GaN/InGaN Microcavities and Applications

GaN/InGaN Microcavities and Applications

A dissertation presented
by

Nan Niu

to

The School of Engineering and Applied Sciences

in partial fulfillment of the requirements
for the degree of
Doctor of Philosophy
in the subject of

Applied Physics

Harvard University
Cambridge, Massachusetts

April 2015

Advisor
Professor Evelyn Hu

Author
Nan Niu

GaN/InGaN Microcavities and Applications

Abstract

Semiconductor micro- and nano-cavities are excellent platforms for experimental studies of optical cavities, lasing dynamics, and cavity Quantum Electrodynamics (QED). Common materials for such experiments are narrow bandgap semiconductor materials with well-developed epitaxial growth technologies, such as GaAs and InP, among others. Gallium nitride (GaN) and its alloys are industrially viable materials with wide direct bandgaps, low surface re-combination velocities, and large exciton binding energies, offering the possibility of room temperature realization of light-matter interaction. Controlling light-matter interaction is at the heart of nanophotonic research which leads to ultra-low threshold lasing, photonic qubits, and optical strong coupling. Technologically, due to its blue emission, GaN photonic cavities with indium gallium nitride (InGaN) active mediums serve as efficient light sources for the fast growing photonic industry, optical computing and communication networks, display technology, as well as quantum information processing.

The main challenges in fabricating high quality GaN cavity are due to its chemical inertness and low material quality as a result of strain-induced defects and threading dislocations. In this dissertation, I examine the designs, novel fabrication processes, and characterizations of high quality factor GaN microdisk and photonic crystal nanobeam cavities with different classes of InGaN active medium, namely quantum dots (QDs), quantum wells (QWs), and fragmented quantum wells (fQWs), for investigating light-matter interaction between cavity and these active media.

This dissertation is carefully organized into four chapters. Chapter 1 outlines the background of the research, the materials and growth, and the necessary technique Photoelectrochemical (PEC) etching which is uniquely used to undercut and suspend GaN cavities.

Chapter 2 outlines the fabrications, optical experiments, and tuning technique developed for GaN/InGaN microdisks. Microdisks are circular resonant cavities that support whispering gallery modes. Through the use of optimized dry etching and PEC, high quality factor microdisks with relatively small modal volume are fabricated with immediate demonstration of low threshold lasing. On the path to achieving light and matter interactions, irreversible tuning of the cavity mode of p-i-n doped GaN/InGaN microdisks is achieved through photo-excitation in a water environment. Such a technique paves the

way for deterministically and spectrally matching the cavity mode to the emitter's principle emission.

Chapter 3 outlines the work done on the high quality GaN photonic crystal nanobeams with InGaN QDs and fQWs. The fragmented nature of the fQW layer has a surprisingly dramatic influence on the lasing threshold. A record low threshold is demonstrated that is an order of magnitude lower in threshold than identical nanobeams with homogeneous QW, and comparable to the best devices in other III-V material systems. As an active medium with greater carrier confinement than quantum wells, and higher carrier capture probability than quantum dots, the fQW active medium, in combination with the nanobeam cavity with ultra-small modal volume and high quality factor, provides an ideal means of probing the limits of light and matter interactions in the nanoscale. Moreover, GaN/InGaN nanopillars are fabricated to isolate a single InGaN QD for understanding its emission properties. Antibunching is observed, demonstrating the quantum nature of the QD emission. Gas tuning is attempted on GaN nanobeams with InGaN QDs to achieve QD-cavity mode coupling and to demonstrate cavity enhanced single photon emission. Last but not least, Chapter 4 concludes the dissertation with summary and future directions.

Table of Contents

Publications

N. Niu*, A. Woolf, D. Wang, T. Zhu, Q. Quan, R.A. Oliver, and E.L. Hu. *Ultra-low threshold Gallium Nitride photonic crystal nanobeam laser*. (Submitted to Appl. Phys. Lett, 2015)

A. Woolf, T. Puchtler, I. Aharonovich, T. Zhu, **N. Niu**, D. Wang, R.A. Oliver, and E.L. Hu. *Distinctive signature of indium gallium nitride quantum dot lasing in microdisk cavities*. Proceedings of the National Academy of Sciences **111**, 14042 (2014)

I. Aharonovich, A. Woolf, K.J. Russell, T. Zhu, **N. Niu**, M.J. Kappers, R.A. Oliver and E.L. Hu. *Low threshold, room-temperature microdisk lasers in the blue spectral range*. Appl. Phys. Lett. **103**, 021112 (2013)

N. Niu*, T.L. Liu, I. Aharonovich, K.J. Russell, A. Woolf, T.C. Sadler, H.A.R. El-Ella, M.J. Kappers, R.A. Oliver and E.L. Hu. *A full free spectral range tuning of p-i-n doped gallium nitride microdisk cavity*. Appl. Phys. Lett. **101**, 161105 (2012) (Cover Letter)

I. Aharonovich, **N. Niu**, F. Rol, K.J. Russell, A. Woolf, H.A.R. El-Ella, M.J. Kappers, R.A. Oliver and E.L. Hu. *Controlled tuning of whispering gallery modes of GaN/InGaN microdisk cavities*. Appl. Phys. Lett. **99**, 111111 (2011)

* Corresponding author

Citations to Previously Published Work

Portions of Chapters 2 have appeared in the following publication:

I. Aharonovich, N. Niu, F. Rol, K.J. Russell, A. Woolf, H.A.R. El-Ella, M.J. Kappers, R.A. Oliver and E.L. Hu. *Controlled tuning of whispering gallery modes of GaN/InGaN microdisk cavities*. Appl. Phys. Lett. 99, 111111 (2011)

Portions of Chapters 1 and 2 have appeared in the following publication:

N. Niu, T.L. Liu, I. Aharonovich, K.J. Russell, A. Woolf, T.C. Sadler, H.A.R. El-Ella, M.J. Kappers, R.A. Oliver and E.L. Hu. *A full free spectral range tuning of p-i-n doped gallium nitride microdisk cavity*. Appl. Phys. Lett. 101, 161105 (2012)

Portions of Chapters 2 have appeared in the following publication:

I. Aharonovich, A. Woolf, K.J. Russell, T. Zhu, N. Niu, M.J. Kappers, R.A. Oliver and E.L. Hu. *Low threshold, room-temperature microdisk lasers in the blue spectral range*. Appl. Phys. Lett. 103, 021112 (2013)

Portions of Chapters 1 and 2 have appeared in the following publication:

A. Woolf, T. Puchtler, I. Aharonovich, T. Zhu, N. Niu, D. Wang, R.A. Oliver, and E.L. Hu. *Distinctive signature of indium gallium nitride quantum dot lasing in microdisk cavities*. Proceedings of the National Academy of Sciences 111, 14042 (2014)

Portions of Chapters 1 and 3 have appeared in the following publication:

N. Niu, A. Woolf, D. Wang, T. Zhu, Q. Quan, R.A. Oliver, and E.L. Hu. *Ultra-low threshold Gallium Nitride photonic crystal nanobeam laser*. (Submitted to Appl. Phys. Lett, 2015)

List of Figures

Acknowledgements

First and foremost, it is necessary for me to express my deepest gratitude to my advisor Professor Evelyn Hu for everything she has done for me since the beginning of my graduate studies. Without her guidance, advise, support, and care, I would never have become the person I am today, I would never have learned those knowledge that makes me capable and confident today, and I would never have obtained any of these research results as I have today. She has given me more patience than any student would ever deserve, and has contributed enormously to my growth. I am very grateful and honored for having the opportunity to pursue 6 years of my Ph.D. studies in Professor Evelyn Hu's research lab and I am sure this experience will be a memory that motivates me every day of my future life. I am also thankful to Professor David Clarke for many interesting discussions and for generously making an initial introduction for me to Professor Evelyn Hu which made all of these happen.

I wish to deliver my gratitude to our former group members, Dr. Tsung-Li Liu, Dr. Kasey Russell, Dr. Fabian Rol, Dr. Jonathan Lee, and Dr. John Joo who

have trained me to master those research techniques for doing my experiments and have consistently and continuously helped me through discussions. Their passion and understanding for science and engineering motivated me and taught me to think differently. I wish to thank our GaN group members Dr. Alex Woolf, Danqing Wang, and our Cambridge University collaborators Dr. Rachel Oliver and Dr. Tongtong Zhu, for the helps and unquestionable trust they have given to me, for the efforts and sweat we contributed together, and for those knowledge and achievements we have gained together. I wish to thank Dr. Shanying Cui for endless supports, fun time, and discussions and for that she and I are the first two students that joined Professor Evelyn Hu's group when the group is relocated to Harvard. I wish to thank Professor Federico Capasso and Professor Marko Loncar for their kind supports and advises and for taking their precious time to be on my qualifying committee and my defense committee. Moreover, I wish to thank all the CNS staff, Dr. Jiangdong Deng, Dr. Ling Xie, Dr. Andrew Magyar, and faculties at SEAS for countless helps they have assisted me with and the time they generously spent with me. I also wish to thank Harvard School of Engineering and Applied Sciences for admitting me as a graduate student twice, once for my Master's Degree application, and once for my Ph.D. Degree application. Harvard SEAS gave me a chance to pursue a life I want and have given me every learning resource I need. I cannot be more grateful to the school.

I want to save this last paragraph in the acknowledgements to thank my parents who have made so much sacrifice for me, who have given me everything, beyond all boundaries of love. This last paragraph being the shortest is because my gratitude to them is at the heart and beyond what language can express.

Dedication

This dissertation is lovingly dedicated to my father, Xulin Niu, and my mother, Huimei Zhang, for their support, encouragement, and endless love that have sustained me throughout my life, and to my grandparents, who left us for a better world, for their love and care for me since the beginning of my memory.

CHAPTER 1: **Introduction and Basics**

1.1 Background

In the recent years, GaN and its alloys have attracted tremendous research and development interest from the science and engineering community due to its unique optical and electrical properties for applications in optoelectronic and electronic devices, such as light emitting diodes (LEDs), lasers, and power electronics. With a wide range of alloy bandgaps (up to 3.4 eV) and high exciton binding energy, the InGaN active medium is highly efficient in light emission across the entire visible spectrum, as shown in Figure 1.1, as well as enhanced room temperature performance compared to other III-V semiconductors [1, 2]. However, one of the main challenges in the growth of nitride semiconductors has been the lack of lattice-matched substrates thereby, inducing a large number of structural defects degrading device performance [3, 4]. Furthermore, conductive p-doped GaN is difficult to achieve, partially due to the high activation energy of Mg dopants and the

slightly n-type nature of intrinsic GaN [4, 5].

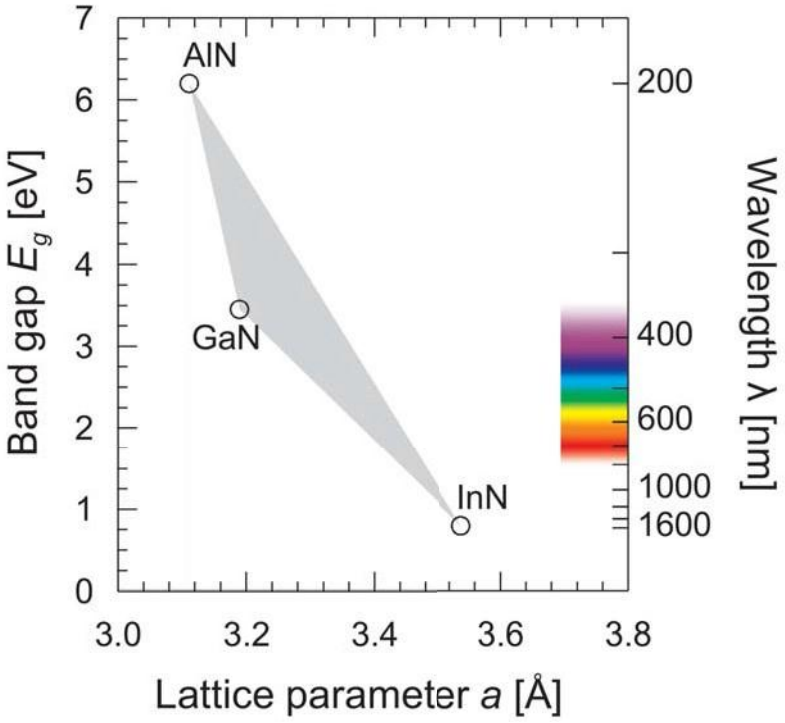

Figure 1.1 Relationship between bandgaps of Wurtzite III-nitrides and lattice parameters. The visible spectrum range is also shown on the wavelength axis [3].

1.2 GaN/InGaN Materials and Defects

GaN, AlN, and InN have wide direct bandgaps of 3.4 eV, 6.2 eV, and 0.7 eV at room temperature, respectively [1, 2]. Figure 1.2 shows a bandstructure of GaN with Wurtzite crystal lattice. Direct electronic transition is allowed

between the Γ valley and the hole bands, giving access to efficient optical emission.

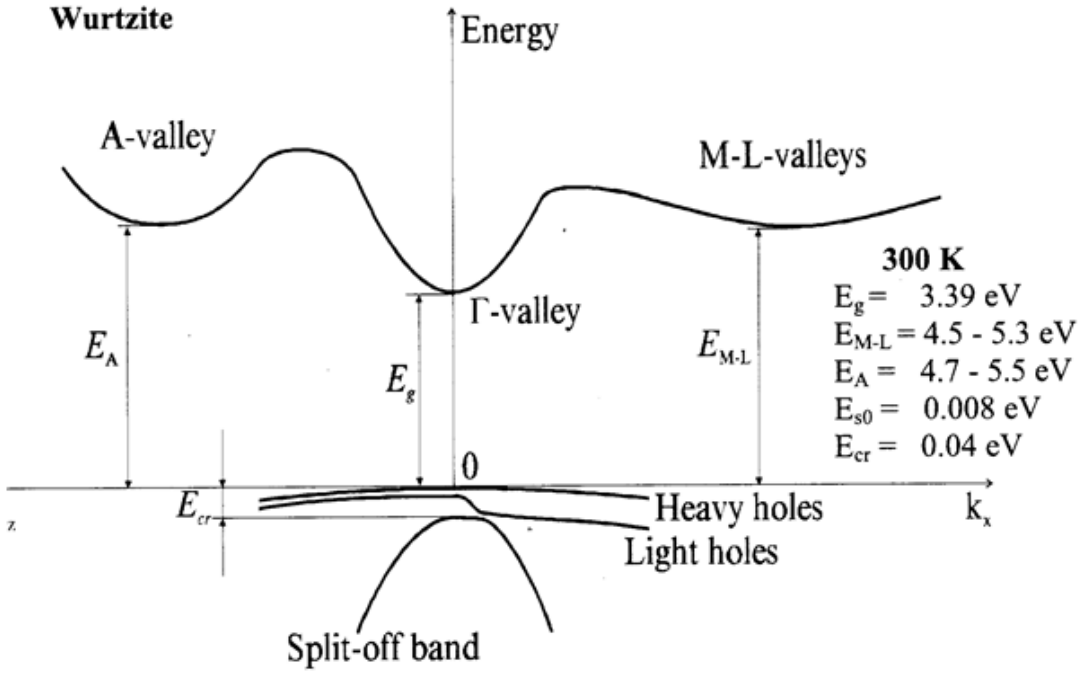

Figure 1.2 Bandstructure of Wurtzite GaN with a direct bandgap [6].

All in all, III-nitride semiconductors can be grown in Zinc-blende and Wurtzite crystal structures [2, 7]. Figure 1.3 shows the schematics of the atomic stacking sequence in a standard Wurtzite and Zinc-blende lattice. However, for GaN, InN, and AlN, only the Wurtzite crystal structure is thermodynamically stable under ambient conditions [2]. A III-nitride Wurtzite unit cell is shown in Figure 1.4 with a table of lattice constants calculated in a stress- and strain-free system.

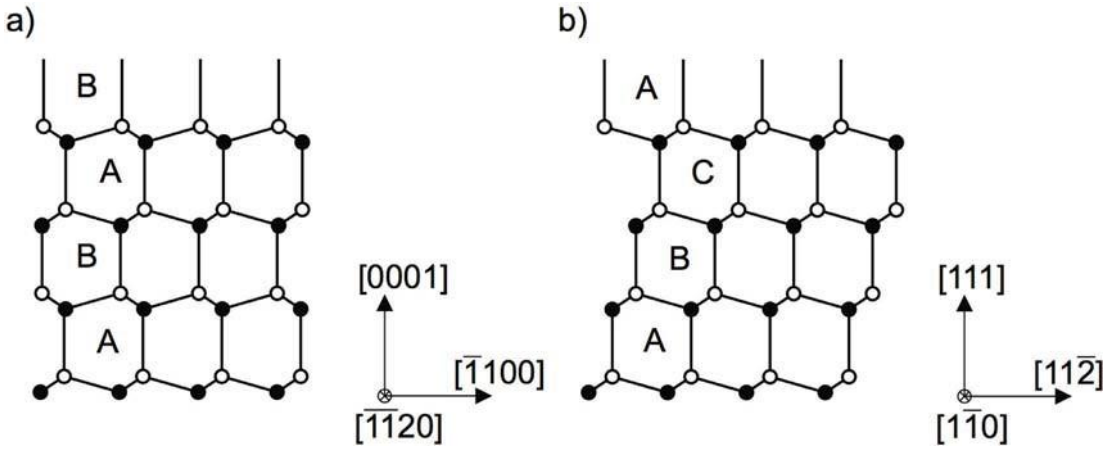

Figure 1.3 Schematic of the atomic stacking sequence in a) Wurtzite and b) Zinc-blende lattice [2].

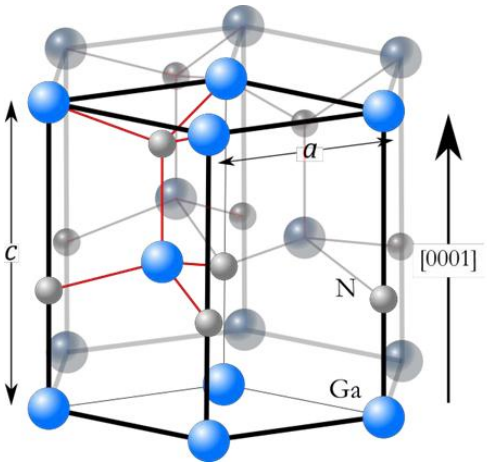

	a (nm)	c (nm)
AlN	0.311	0.498
GaN	0.319	0.518
InN	0.353	0.569

Figure 1.4 Schematic of the III-nitride Wurtzite unit cell with table of lattice constants [8].

In the III-nitrides Wurtzite crystal structure, due to the lack of symmetry in the [0001]/c-direction and the partially ionic nature of the bonding, a spontaneous polarization thereby exists along the c-axis, the polar axis [8, 9]. All materials used for experiments in this dissertation are epitaxially grown along the c-direction and therefore referred to as c-plane material.

Moreover, III-nitride semiconductors exhibit piezoelectric polarization in a strained environment, which naturally occurs due to lattice mismatch and different thermal expansion coefficient among the substrate and growth materials and alloys. Such piezoelectric polarization is large in III-nitrides, an order of magnitude larger than typical III-V and II-IV semiconductors [4, 9].

1.2.1 Polarization and Internal Fields

An internal electric field along the c-axis, a unique property of Wurtzite semiconductor, has dramatic effects on the emitters and device properties. As Figure 1.4 shows, in the crystal matrix of GaN and its alloys, there exists a non-centrosymmetry in the c-direction. Moreover, due to the higher electronegativity of the nitrogen, electrons are attracted and localized closer to the nitrogen atoms. This electronic arrangement in the matrix gives rise to a spontaneous polarization as shown by the arrow in Figure 1.4 [8, 9].

The net result of the polarization is an internal electric field that bends the electronic band along the c-direction. It is calculated that an internal field in the order of MV/cm can exist in GaN and its alloys [9, 10]. Due to the internal field, electrons and holes are delocalized leading to a dramatic reduction of the spontaneous emission (SE) rate and the corresponding oscillator strength. Such effect is even stronger for confined heterostructure systems epitaxially

grown along the c-axis. In a confined system such as a Quantum Well (QW) or Quantum Dot (QD), the internal field pushes the carriers, due to their opposite charges, in opposite directions. The spatial separation, or in quantum mechanical terms a decrease in the overlap between wave functions of conduction electron and valence hole as shown in Figure 1.5, reduces the probability of a recombination event [11]. This observation is known as the quantum-confined Stark effect (QCSE). Moreover, the internal field decreases the energy separation between the lowest confined electronic energy level in the conduction band and valence band, leading to a red shift in emission spectrum [12].

.

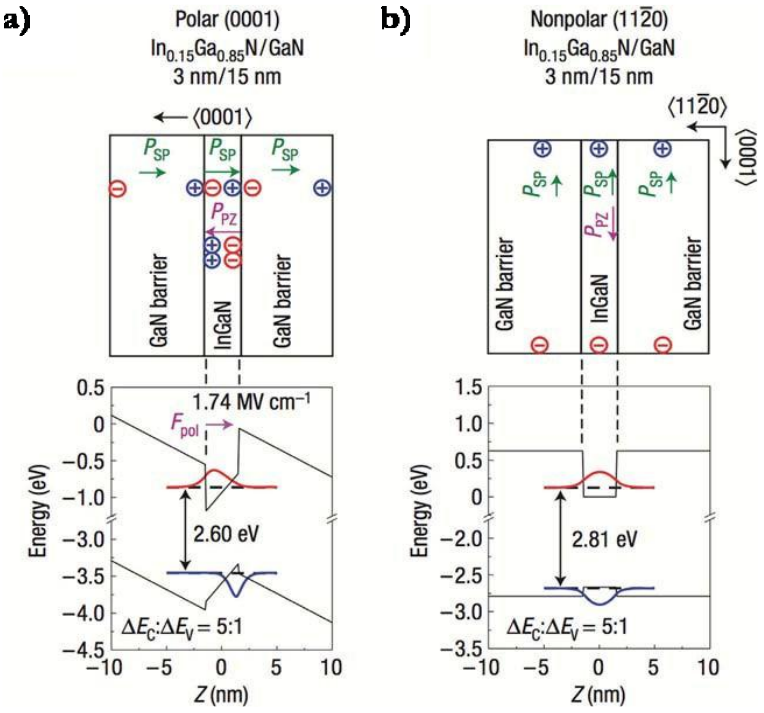

Figure 1.5: Comparative schematics of a) a polar InGaN/GaN QW and b) a non-polar InGaN/GaN QW. Due to polarization, charges accumulate at interfaces of polar-oriented QW [12].

1.2.2 Materials Growth

Heteroepitaxy, the technique for growing materials different from the substrate, is common for the growth of GaN and its alloys due to the lack of large bulk nitride substrates. Among all available substrates for GaN growth, with up to 16% lattice mismatch [13] and with a large difference between thermal coefficients, it is interesting that sapphire has been the most widely used substrate material. It is transparent and stable during high temperature growth. In general, there are three main growth techniques used, metal-organic vapor phase epitaxy (MOVPE), molecular beam epitaxy (MBE), and metalorganic chemical vapor deposition (MOCVD) [13]. MOVPE, as the principal growth technique, and sapphire substrates are the choices for all materials grown for experiments in this dissertation.

During a standard MOVPE growth, gaseous precursors flow with ammonia (NH_3) in a carrier gas of nitrogen or hydrogen to a heated substrate surface. A thin film will be formed through layer by layer growth with an epitaxial relationship to the substrate [4, 7]. For the growth of III- nitrides, the metal-containing group III precursors are trimethylgallium $Ga(CH_3)_3$, trimethylindium $In(CH_3)_3$, or trimethylaluminum $Al(CH_3)_3$.The basic reaction for GaN growth is given as follows:

$$Ga(CH_3)_3(gas) + NH_3(gas) \rightarrow GaN(solid) + 3CH_4(gas)\ [4]$$

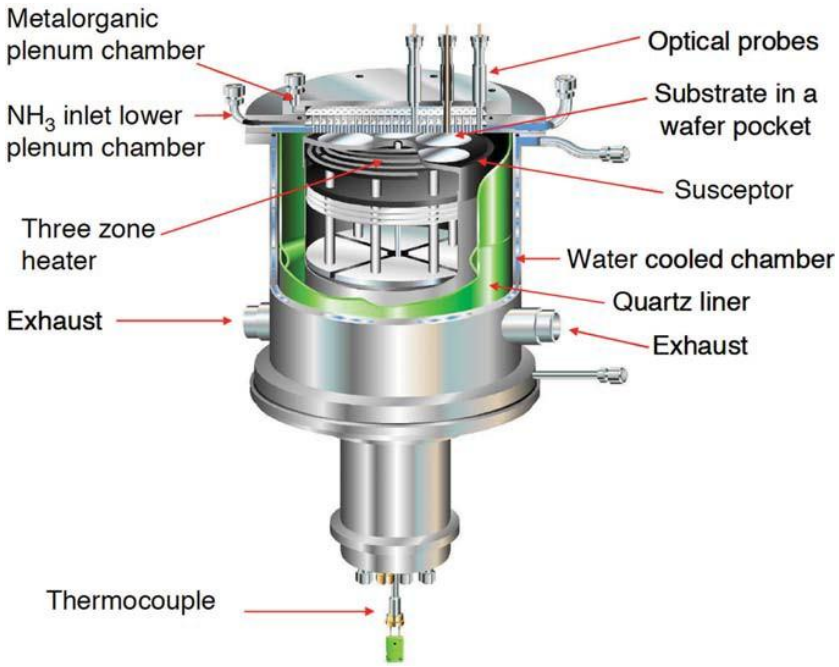

Figure 1.6: Schematic of Thomas Swan close-coupled showerhead MOVPE reactor [14].

It is important to note all materials used in this dissertation were grown by Dr Tongtong Zhu in a 6 x 2 in. Thomas Swan close-coupled showerhead (CCS) reactor as shown in Figure 1.6. Substrate temperature, reactor pressure, and the pressure ratio of III and V group precursors are important controlled parameters for MOVPE growth of high quality III-nitrides. High temperatures, above 1000 °C, are required for GaN for creating high surface mobility critical for improving the surface morphology, and facilitates the breakdown of NH3. Moreover, high V/III ratio is required to prevent desorption of nitrogen during growth process [4, 7].

1.2.3 InGaN Quantum Dots

A quantum dot (QD) is a semiconductor crystal with a typical size within the order of the wavelength of its electron wavefunction or the effective Bohr radius. In a QD, its exciton is confined in all three spatial dimensions with an enhanced oscillator strength thereby allowing a stronger overlap between the electron and hole wavefunctions in the conduction and valence band, respectively. As a result, in general the radiative recombination for a QD embedded in a barrier material is highly efficient compared to embedded quantum wells (QWs) of the same material [15-17]. Moreover, in a 3-dimensionally confined system, energy levels become discrete and transitions between such levels result in sharp spectral lines as shown in Figure 1.7 indicating an optical density of states resembling a delta-like function, which is the optical signature of single QDs [18].

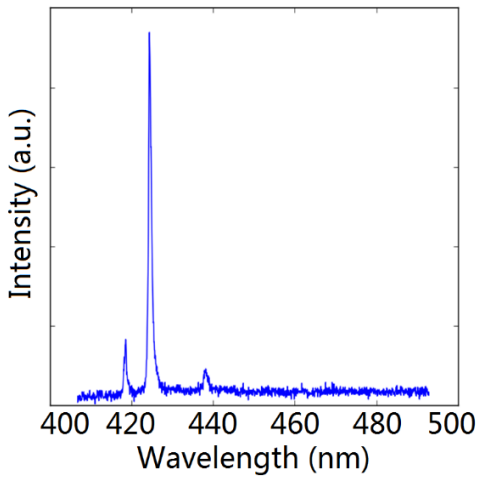

Figure 1.7 Emission spectrum of an unintentionally doped GaN/InGaN quantum dot sample optically excited by a 380nm laser at 4K.

Growth of InGaN QDs is a very challenging and involved process. Aside from the strain accumulated between the GaN and the sapphire substrate, due to lattice mismatch, strain also exists between InGaN and GaN layers. In addition, defects can be incorporated into the material such as residual and unwanted hydrogen in the carrier gas. Such a non-ideal environment prohibits QD formation via the standard Stranski-Krastanov (SK) mechanism, often useful for the growth of arsenide and phosphide QDs [19-21]. Addressing the challenge in forming InGaN QDs, Dr Rachel Oliver et al. (2003) proposed another path for epitaxially growing InGaN QDs in GaN barrier material by utilizing the Modified Droplet Epitaxy (MDE) [22, 23].

A simplified MDE growth process flow is illustrated by Figure 1.8. An $In_xGa_{1-x}N$ epilayer with a set composition is initially grown to approximately 3nm in thickness. In-rich regions are expected to form at step edges, dislocations, and other features throughout the epilayer. It is then annealed under a nitrogen environment at the growth temperature for a pre-set time to encourage the decomposition of In rich regions into N_2 and metal In/Ga. A significant amount of the decomposed metal accumulates in scattered areas to form nano-scale droplets due to surface tension. Figure 1.8 (d, ii) shows an atomic force microscope (AFM) image of an uncapped annealed InGaN layer, where the white dots are the metallic droplets. Hypothetically, it is believed that during the subsequent growth of a GaN cap, the metallic droplets would go

through re-nitridation, resulting in the formation of InGaN QDs within the GaN barrier material. It is found that adjusting the temperature and anneal time alter the areal density and size distribution of the metallic droplet prior to capping. However, the errors associated with such control are high and deterministically positioning the QDs is impossible [7, 22-25].

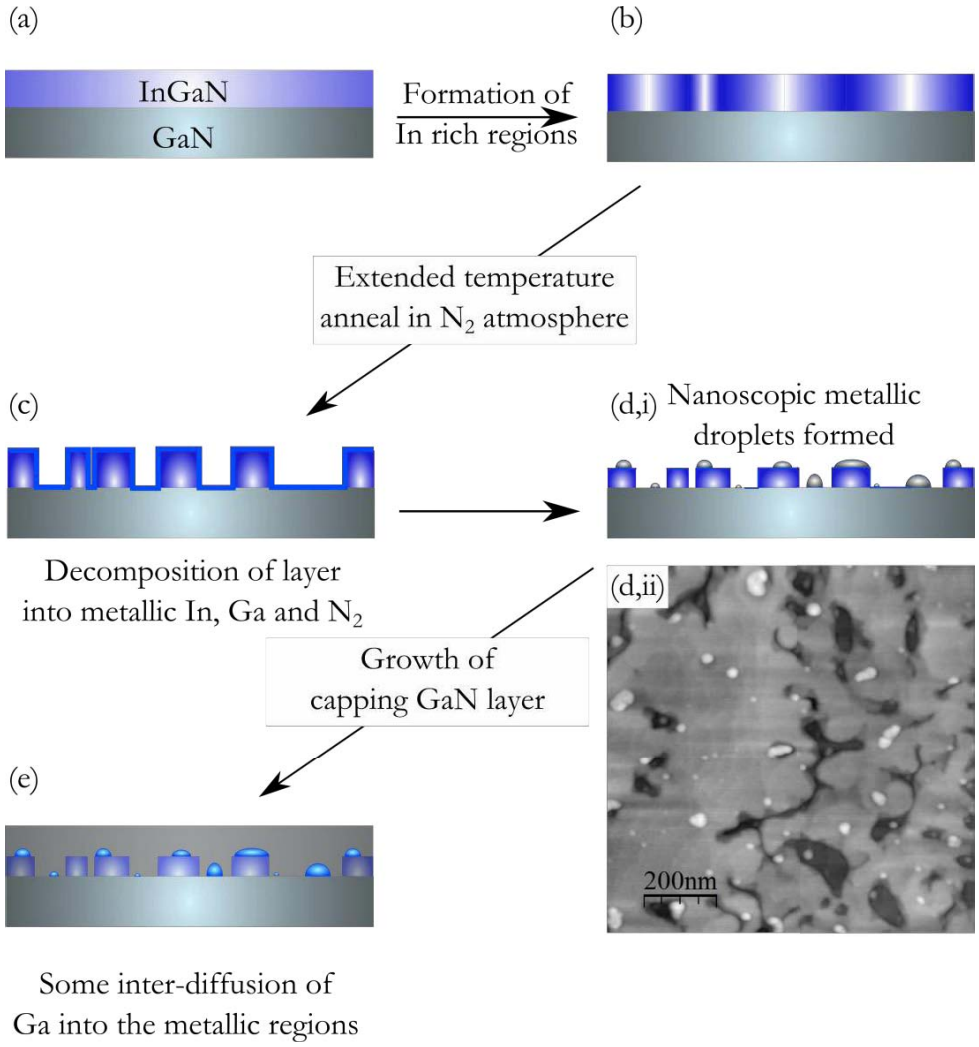

Figure 1.8 A simplified MDE growth process flow for GaN/InGaN QDs materials. Sub-figure (d, ii) shows an AFM image of an uncapped annealed InGaN layer [7].

Due to the lack of precise control of the QD formation process, the QD densities of samples grown under the same condition occasionally differ by as much as an order of magnitude. Moreover, intrinsic to the MDE process, is the presence of the fragmented quantum well (fQW) layer created during the anneal process; thus the emission spectra of GaN/InGaN QDs samples contained emission signatures of both InGaN QDs and fQWs. This creates difficulties for doing analysis and comparisons for GaN/InGaN QDs samples and understanding its effect on cavity phenomenon such as lasing and coupling.

Figure 1.9 shows a photoluminescence spectrum of a bulk unintentionally doped GaN/InGaN QDs wafer excited by a 380nm Ti-Sapphire frequency doubled laser at 4K with the optical measurement set-up described in Appendix A. Due to the discrete density of states of QDs, narrow and isolated emission peaks are clearly observed indicating successful formation of QD structures. Through MDE growth, it is estimated that InGaN QD is composed of 20 - 30 % In. As a result of the difference in compositions, contribution from the fragmented QW layer, and the difference in size of the decomposed metallic droplets which subsequently formed InGaN QDs, a broad emission peak generally spans from 410 nm - 490 nm in wavelengths.

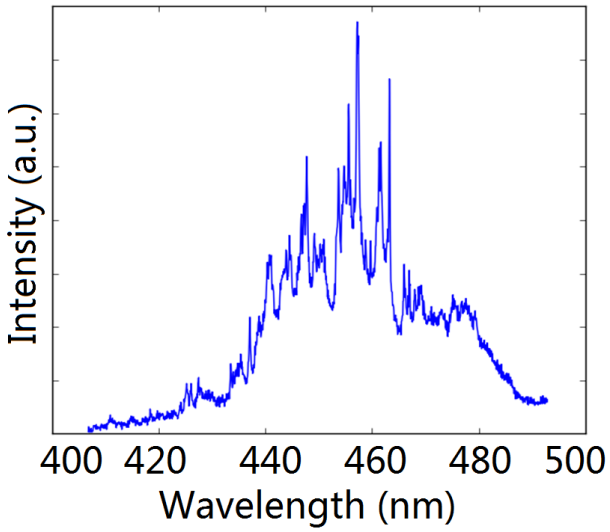

Figure 1.9 Photoluminescence spectrum of a bulk unintentionally doped GaN/InGaN QDs wafer excited by a 380nm Ti-Sapphire frequency doubled laser at 4K.

The difference in internal strain, In compositions, and size of the InGaN QDs, gives rise to differences in the strength of the internal polarization fields among the QDs. Such internal fields alter and weaken the electron-hole wave function overlap and the oscillator strengths, and thus creates differences in the radiative lifetimes of the QD ensemble, between 1 ns and 5 ns, with exceptions up to and exceeding ~ 100 ns [26, 27]. Experiments on studying the InGaN QDs will be discussed in detail in section 3.3.1 of Chapter 3.

1.2.4 InGaN Fragmented Quantum Wells

For the lasing experiments outlined later in this dissertation, a unique active

medium deserves special attention, namely the fragmented quantum wells, formed during the annealing process after the initial $In_xGa_{1-x}N$ epilayer is grown [28]. Compared to zero-dimensional QDs, fQWs are analogous to inhomogeneous quantum wells which exhibit quantum confinement in two directions. Similar to QDs, the fQWs also exhibit significant variation in thickness and In composition, especially in the vicinity of dislocation pits on the surface of the underlying GaN [29]. Figure 1.10 shows an AFM scan of the fQWs before capping. The average width of the InGaN fQW strips is approximately 70 nm. The inset image shows an AFM line profile of a selected region on the as-grown annealed InGaN epilayer indicating a height variation of roughly 3 nm. In the standard fQW materials used for cavity purposes, the fQW was formed by growing a 2.5 nm thick InGaN epilayer at 710^{o} C and annealing at the growth temperature for 240 seconds in an atmosphere of NH_3 and N_2 prior to capping with 7.5 nm of GaN. Following annealing, the InGaN epilayer exhibits a network of interlinking InGaN strips aligned roughly along the [11-20] direction. After the growth of the GaN capping layer, a composition gradient in the InGaN strip is expected to form, making the center of the strip more indium rich than the edges [30]. This creates a graded electronic potential which confines the carriers at the center of the strips. For comparison and in order to better determine the In composition, analogous structures were grown that contained continuous InGaN QW material. Both the QWs and the GaN barriers were grown at a temperature of 740 °C, again

under N_2. X-ray diffraction (XRD) was used to characterize the indium content of continuous QWs to be approximately 18%. It's impossible to obtain reliable XRD quantification of the indium composition of fQW due to its non-uniformity. While the average indium content of the fQW will be lower than that of the QW, previous microscopy studies suggest that at the center of the InGaN strips both the width and composition of the fQW should be similar to that of the QW structure.

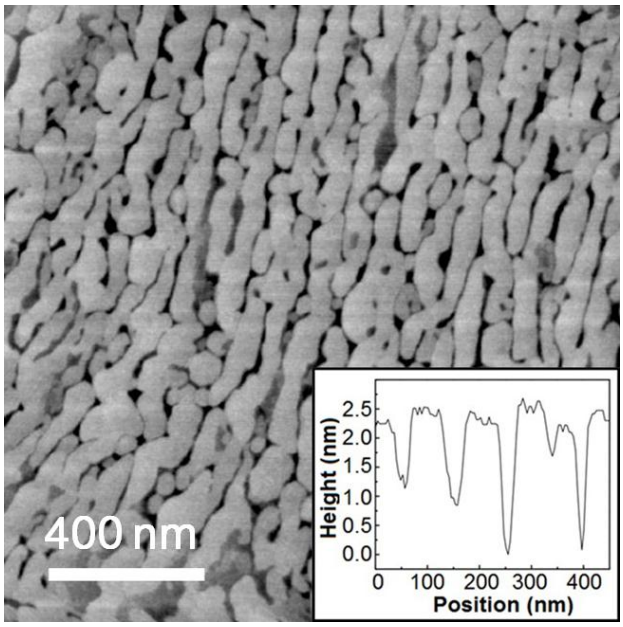

Figure 1.10 AFM scan of the fQWs before capping. The average width of the InGaN fQW strips is approximately 70 nm. The inset image shows an AFM line profile of a selected region on the as-grown annealed InGaN epilayer indicating a height variation of roughly 3 nm.

In the early stages, it was believed that the formation of a large amount of fragmented QW together with QDs was a significant drawback of the MDE when growing QD samples. The inevitable presence of the fQWs with QD

active layers made it difficult to delineate the unique role of the QD in optical emission and ultimately, in lasing. However, given the results of the ultra-low threshold lasing experiments discussed in Chapter 3, the beneficial role of fQWs has been better realized. Figure 1.11 shows a room temperature photoluminescence spectrum of a bulk unintentionally doped GaN/InGaN fQWs wafer excited by a 380nm Ti-Sapphire frequency doubled laser. Principal emissions for InGaN fQWs span from 420nm to 490nm. Due to the larger optical density of states, fQWs materials emit with stronger intensity compared to QD materials.

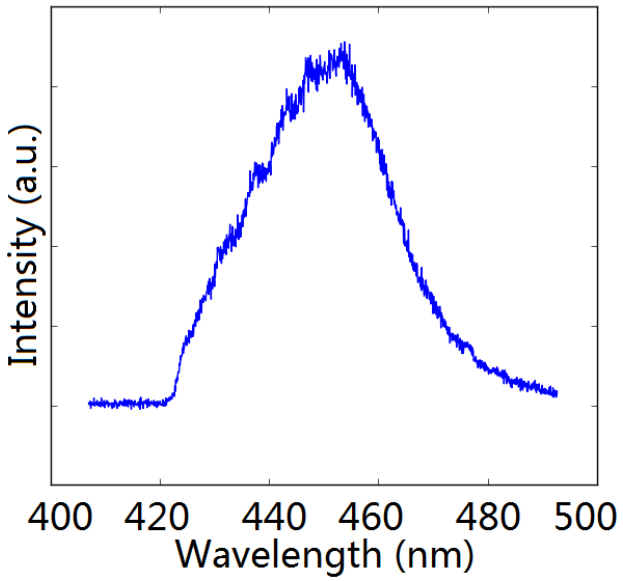

Figure 1.11 Room temperature photoluminescence spectrum of a bulk unintentionally doped GaN/InGaN fQWs wafer excited by a 380 nm Ti-Sapphire frequency doubled laser.

1.2.5 Threading Dislocations

Threading dislocations (TDs) are lines of crystallographic defects created as a result of large lattice and thermal expansion coefficient mismatches among the different growth materials and the substrate [31, 32]. Electronically, TDs induce electron scattering thereby reducing the carrier mobility [32-34], and increasing the leakage current in devices [35]. All in all, TDs can be non-radiative recombination centers thereby reducing the optical efficiencies of the material [36], however, their effects on the optical quality of cavities are more subtle and are described in the succeeding chapters [37]. As a result of largely mismatched sapphire substrates, TDs are widely found in GaN, and their density can reach up to approximately $10^{10}/cm^2$ [38-40]. Such high density of TDs adversely affect the fabrication and performances of the GaN/InGaN optical cavities.

Even though TDs originate within and throughout bulk GaN material, they do propagate through the layer and terminate as pits at the material surface, which are clearly visible using AFM. By selecting the underlying substrate, it's possible to obtain crude control, to a certain extent, over the TDs density (TDD) of a grown wafer. Figure 1.12 shows AFM images of three wafers with different threading dislocation densities. The dark spots are the pits at which threading dislocations terminate. The purpose of growing and working with

material batches such as these is for experimental comparison and analysis of the optical properties of the materials and cavities with correlations to dislocation densities.

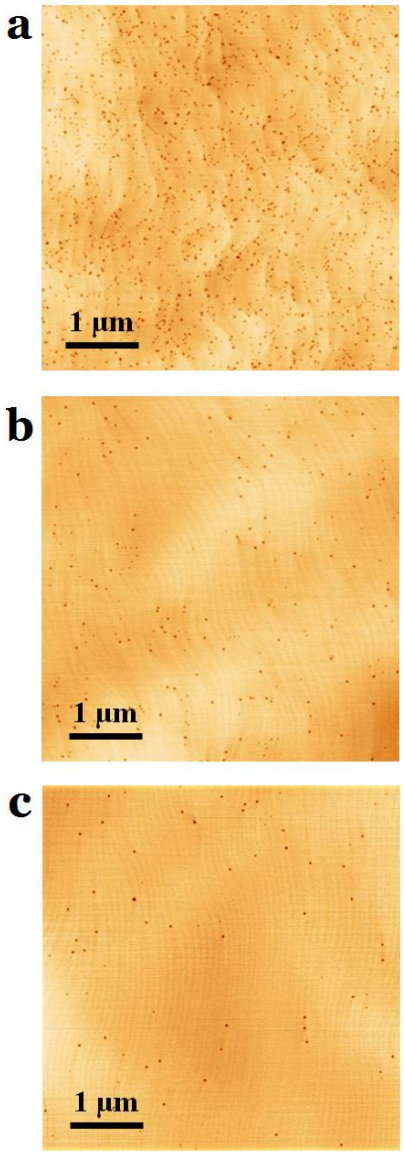

Figure 1.12 AFM images of as-grown GaN before capping. Dark spots are surface pits due to threading dislocations. a) highly-resistive (HR) with TDD~5.64 x 10^9 cm^{-2}, b) medium dislocation density (MDD) with TDD~1.01 x 10^9 cm^{-2}, c) low dislocation density (LDD) with TDD~3.16 x 10^8 cm^{-2} [29].

One of the most important factors that contributes to the success of GaN for industry and light applications is its high optical efficiency despite the intrinsic large TDs density. Such level of TDs density can render conventional III-V compound semiconductors optically inactive. It has been a long on-going debate that InGaN-based LEDs may be insensitive to dislocations [41, 42]. These observations are often attributed to the inevitable fluctuations of the In composition in the active medium thereby creating localization potentials for carriers [43].

Sugahara et al. (1998) used transmission electron microscopy (TEM) in conjunction with cathodoluminescence (CL) imaging and demonstrated that dark spots in the CL image occur at the locations of the TDs as shown in Figure 1.13 [44]. This evidently proves that TDs are non-radiative recombination centers for carriers which can lead to reduced internal quantum efficiency (IQE) [41]. From this analysis, the minority carrier diffusion length is determined to be approximately 50 nm. Consequently, if minority carrier diffusion length is shorter than dislocation spacing, radiative recombination is most likely to dominate over non-radiative recombination events.

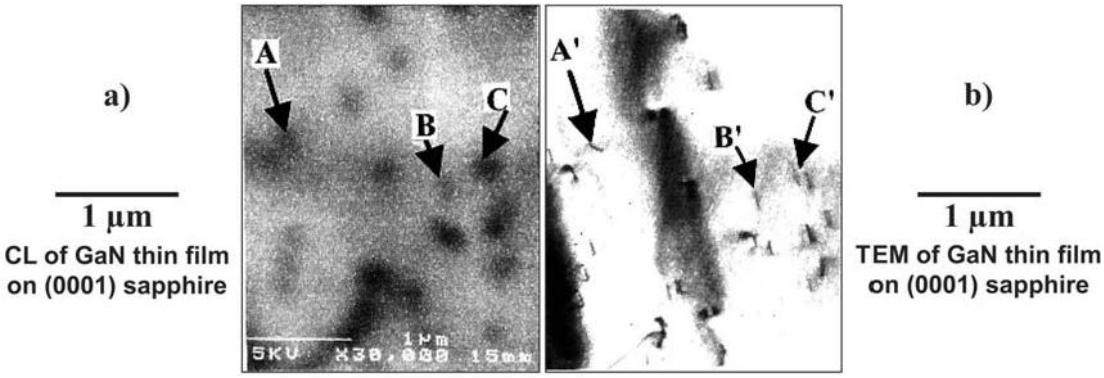

Figure 1.13 a) CL image and b) plan-view TEM image of a zoomed-in region of a GaN film grown on (0001) sapphire substrate, showing correlations between dark spots in CL and the dislocations in TEM [44].

1.3 Photoelectrochemical Etching

Intrinsic chemical inertness can prevent the aging of semiconductor materials and device. However, such advantage can also post significant challenges for fabrication of useful devices. In the past, due to its chemical stability, processing of GaN-based devices relied heavily on dry etching [45]. The majority of photonic devices require selective etching and removal of certain layers while preserving other layers intact and free from damage. For example to optically isolate, or suspend a cavity structure, an ion-damage free, selective wet chemical etching technique would be preferable.

Photoelectrochemical (PEC) etching is an easily accessible technique to etch

GaN and its alloys at room temperature [46, 47], and is the only selective wet etching technique one uses for etching GaN and its alloys in this dissertation.

In short, PEC is a photo-assisted wet etch technique. The PEC apparatus consists of an above-bandgap Xe light source and an electrochemical cell as shown in Figure 1.14. During the PEC process, the semiconductor serves as the anode and a metal in contact with the surface serves as the cathode [45, 47]. For the choice of metal for cathode, one uses 50 nm of Pt or 50 nm of Au with 5 nm of Ti for adhesion purpose directly evaporated onto the material surface. The incident light is partially absorbed by the GaN or its alloys generating electron-hole pairs within the material. Electrons are efficiently extracted through the cathode to create a net hole concentration within the material. Holes, if diffused to the surface of the semiconductor, can react with the electrolyte, forming an oxide. Such oxide is dissolved in the electrolyte, resulting in material etching [48].

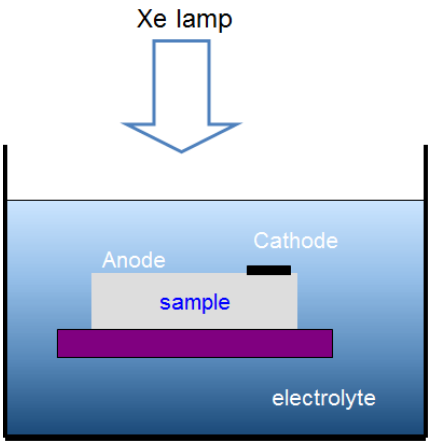

Figure 1.14 A standard PEC apparatus for etching GaN and its alloys.

In choosing the electrolyte, three simple considerations need to be fulfilled: 1) the unilluminated electrolyte does not lead to material etching, and 2) is conductive over the distance between surface to be etched and cathode, and 3) such solution needs to readily dissolve the formed oxide.

For all the fabrications used for making photonic cavities in this dissertation, the electrolyte is 0.004 M of HCL. Figure 1.15 is a selectively etched microdisk using PEC etch in 0004 M of HCL electrolyte. Used in conjunction with reactive ion etching (RIE), PEC allows fabrication of sophisticated device and cavity geometries.

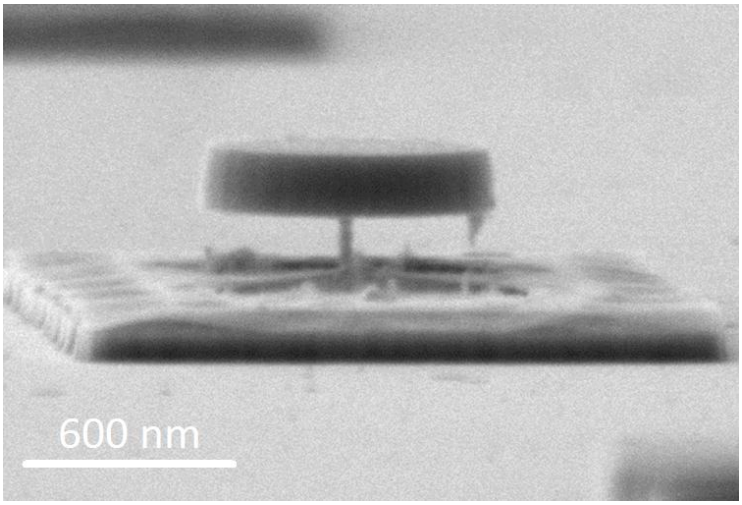

Figure 1.15 A suspended microdisk formed by selectively etching the InGaN layer in a circular mesa in 0.004 M HCL under Xe lamp for 10 minutes. The InGaN layer is sandwiched between two layers of GaN in the mesa.

Above all, due to the dependence on hole concentration, a few limitations, as listed below, exist intrinsically to PEC etching creating difficulties for processing high quality GaN devices:

1. High sensitivity to built-in electrical fields;
2. Selectivity to defects and threading dislocations;
3. General difficulty to etch p-type GaN due to surface bending at the interface with the electrolyte.

In this section, the selectivity and challenges of the PEC process will be addressed in detail. Using PEC along with other standard processing tools available in cleanroom, all the photonic cavities of interest in this dissertation, namely microdisk and photonic crystal nanobeam, have been successfully fabricated.

1.3.1 Selectivity

Selectivity in etching can be leveraged for fabricating advanced and sophisticated device structures. However, selectivity can also complicates the process, and in certain case, to an extent that certain desired geometries become impossible to realize. Due to the need for generating a net hole

concentration at the surface of the material in the electrolyte, PEC etching is often dictated by two important material selectivity parameters, namely the doping and bandgaps [45, 49].

When a semiconductor is in contact with an electrolyte, a depletion region in the material is created near the interface with the electrolyte causing the material's electronic band to bend. In n-type materials, photo-generated holes within the semiconductor are accelerated towards the interface by the curvature of band bending as shown in Figure 1.16 (a). This results in oxidation of the semiconductor surface and subsequent etching. However, in a p-type materials as shown in Figure 1.16 (b), band bending creates a natural barrier for the holes to reach the interface between the semiconductor and electrolyte, thereby preventing the formation of surface oxide. As a result, it's believed that p-type GaN is resistive to PEC etching [45].

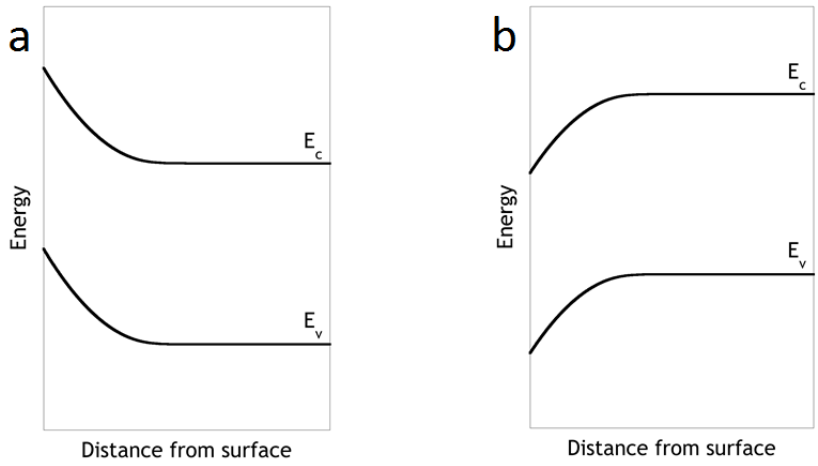

Figure 1.16 Electronic band bending at the semiconductor and HCL interface for (a) a n-type materials and (b) a p-type material [45].

A semiconductor absorbs photon with energies above its bandgap [50]. This selective absorption process allows the possibility of bandgap-selective etching, which along with careful design realizes many practical device geometries. Only the material layer which absorbs the incident photons will be etched. Figure 1.17 (a) shows a scheme for selective etching of a single material layer, one with narrower bandgap, by using photons in between the energy of the two bandgaps of the two materials. For most material structures one works with, InGaN is used as the sacrificial layer which is selectively etched using PEC leading to suspended structures. For such reason, Xe lamp is used as the light source with a GaN wafer immediately below serving as optical filter to remove the spectrum absorbable by GaN, as shown in Figure 1.17 (b).

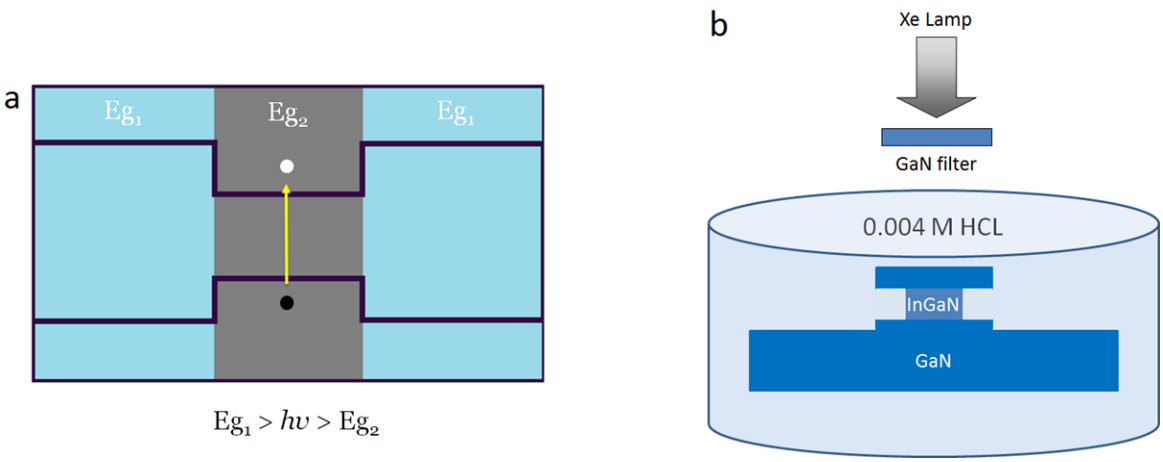

Figure 1.17 a) A material design for selective etching of the material layer positioned in the middle with narrower bandgap using photons in between the energies of the two bandgaps of the two materials. b) PEC set-up for selectively etching InGaN with GaN barrier layers.

1.3.2 Process Challenges

Because of the reliance on excess hole concentration, PEC etching is sensitive to defects. As discussed in the section on TDs, TDs along with many other defects trap free carriers, especially electrons, therefore will inhibit the etch rate and create etch stop surfaces [45, 49]. In the application for GaN/InGaN, this results in the formation of etch resistant whiskers in a selective removal process of InGaN. Since c-plane GaN on sapphire has high density of TDs, the etch-resistant effect is therefore exacerbated creating high density of whiskers attached to the GaN barrier material. In addition, whiskers that are attached to a cavity act as scattering centers, break the ideal symmetry of the cavity, and lower its optical quality. Figure 1.18 (a) shows an undercut 3 micron GaN/InGaN microdisk with 1 layer of InGaN QDs using PEC. It can be easily observed in the red highlighted box, whiskers are created underneath the periphery of the microdisk. Figure 1.18 (b) shows an undercut GaN/InGaN mesa with high density of TDs creating a large density of whiskers using PEC. Until today, there has not been consistent proven results and advancements which can eliminate whiskers using PEC or post-growth fabrication techniques. As a result, it creates heavier reliance on the growth of high quality materials with low density of TDs and defects.

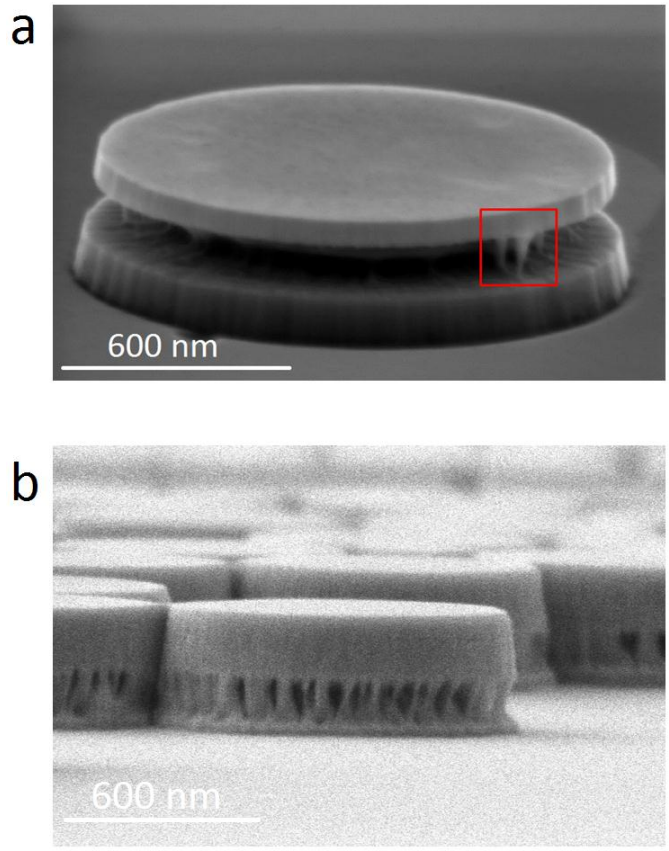

Figure 1.18 (a) A 3 micron GaN/InGaN microdisk with 1 layer of InGaN QDs undercut using PEC. The red box highlights the whiskers underneath the periphery of the microdisk. (b) An undercut GaN/InGaN mesa with high density of TDs using PEC.

1.3.3 Material Designed for Cavity Application

Bandgap-selective PEC etching is widely used for suspending cavities in this dissertation. Figure 1.19 shows a standard epitaxial GaN/InGaN material structure with 3 layers of fQWs. In general, the only difference among material samples for cavity is the choice of the active medium. Compared to

other conventional semiconductor materials for cavities, two unique features deserve special attention, namely the sacrificial superlattice for PEC etching and the etch stop AlGaN layer inside the cavity membrane. Due to the internal fields in GaN and InGaN, carriers especially holes are confined at the interfaces between layers, giving uneven etch profiles for thick InGaN layer. As a result, the superlattice was developed to create more interfaces in a periodic fashion to effectively trap holes leading to uniform etch profile [51]. Moreover, a high resistance AlGaN layer is embedded between the superlattice and the active medium for preventing electrons escaping from the active medium layer, which then creates an excess hole concentration locally and subsequently leads to etching [52].

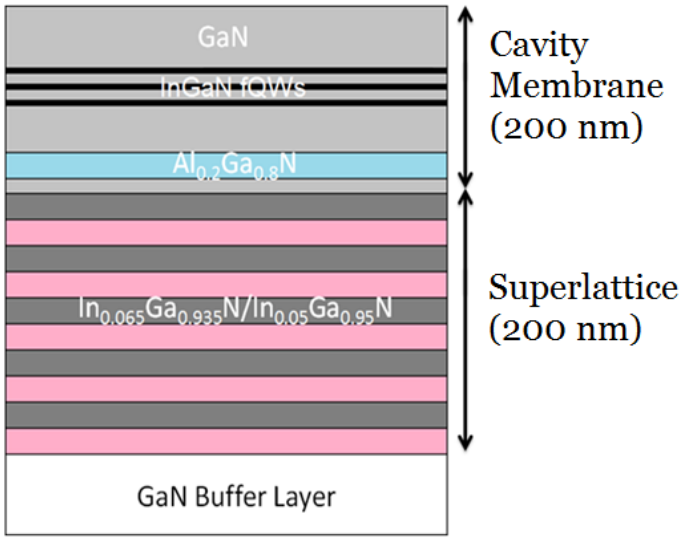

Figure 1.19 A standard GaN/InGaN material structure with 3 layers of fQWs for fabricating GaN/InGaN photonic cavities.

1.4 GaN/InGaN Materials for Cavities

There are a few GaN/InGaN material structures used for fabricating cavities in this dissertation. Their main differences are the thicknesses of the cavity membranes and the choice of active media. Their growth and structures are described in detail below.

(1) 200 nm unintentionally doped (uid-) GaN with 3 layers of InGaN active media (QW, QDs, and fQWs) on InGaN/InGaN sacrificial superlattice (SSL) grown on LDD GaN templates.

The growth starts with a standard Si-doped LDD GaN template [29]. A sacrificial superlattice of un-doped $In_{0.065}Ga_{0.935}N/In_{0.05}Ga_{0.95}N$ (200 nm total depth for PEC selective removal to suspend the cavity membrane or its periphery in air) was then grown and capped by 10 nm of uid-GaN. Then 20 nm of $Al_{0.2}Ga_{0.8}N$ was grown at 1050 °C as an etch-stop layer for the PEC etching, followed by the growth of 60 nm of uid-GaN on top of which 3 layers of InGaN active medium (QW, fQW, or QD) were then grown according to detailed paragraphs below. After the final InGaN active medium layer was grown, a 10 nm GaN capping layer was grown at the same temperature as the InGaN in N_2, followed by a further 80 nm of uid-GaN grown at 1000 °C using

H_2 as the carrier gas. The final structures are shown in Figure 1.20.

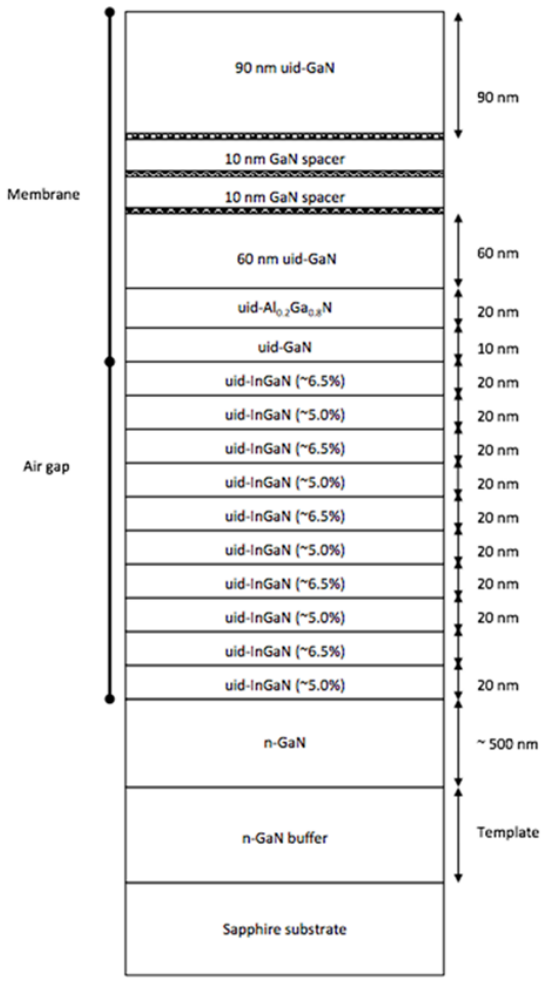

Figure 1.20 Material structure for a 200 nm thick uid-GaN membrane with 3 layers of InGaN active layer material (QW, QDs, fQWs) on InGaN/InGaN sacrificial superlattice grown on LDD GaN templates.

Growth of InGaN QWs (shown in Figure 1.21 (a))

To minimize the indium loss from the QW during barrier growth, GaN barriers were grown, at the same temperature as the InGaN QWs, at 740 °C. The nominal thickness for the QWs is 2.5 nm. This method resulted in

continuous QWs with no visible well width fluctuation measured using transmission electron microscopy [53].

Growth of InGaN fQWs (shown in Figure 1.21 (b))

The 2.5-nm-thick InGaN epilayers were grown at 710 °C and annealed at the growth temperature for 240 s in an NH_3/N_2 atmosphere. The use of NH_3/N_2 gas mixture was to ensure that the annealed InGaN epilayer exhibits a network of interlinking InGaN strips aligned along the [11–20] direction without the formation of any metallic droplets during the annealing process. GaN barrier layers were then grown at 710 °C [53, 54].

Growth of InGaN QDs (shown in Figure 1.21 (c))

As described in Chapter 1, MDE was used for the growth of InGaN QDs. A 2.5-nm InGaN epilayer was initially grown at 710 °C and a post-growth N_2 anneal was performed for 30 s, causing the layer to be broken into regions of "surface pits" and regions of "fragmented QW" with metallic indium/gallium droplets created across both of these regions. During the growth of the GaN capping layer, these droplets re-react with ammonia leading to the formation of InGaN QDs. GaN barrier layers were then grown at 710 °C [23].

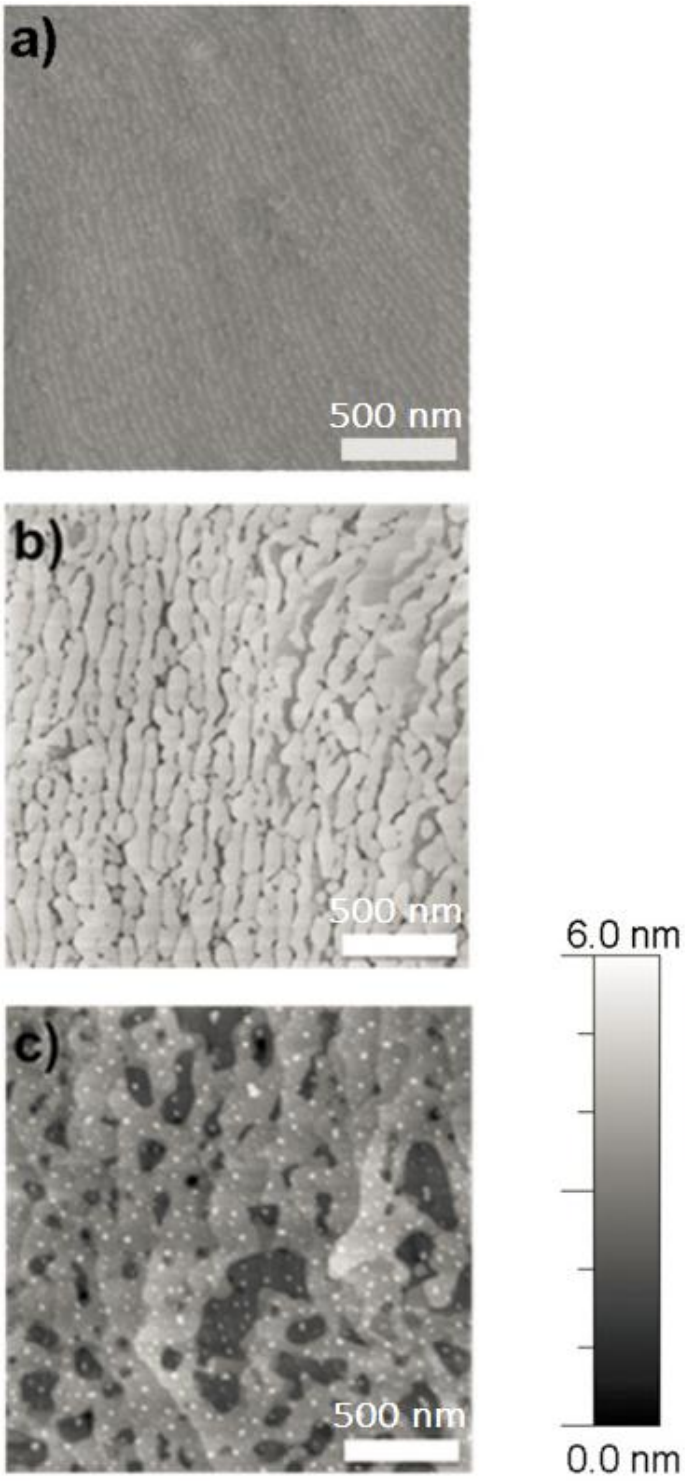

Figure 1.21 AFM images of uncapped active layers for growing (a) homogenous InGaN QW, (b) InGaN fQWs, (c) InGaN QDs [55].

(2) 120 nm GaN with 1 layer of InGaN QDs on InGaN-InGaN SSL grown on c-GaN LDD template.

The material structure was grown by metalorganic vapor phase epitaxy on a c-plane GaN/Al_2O_3 pseudo-substrate [28, 29]. A sacrificial superlattice of n-doped $In_{0.065}Ga_{0.935}N/In_{0.05}Ga_{0.95}N$ (200 nm total depth) was then grown and capped by, 30 nm of n-GaN for a p-i-n junction, or 30 nm of uid-GaN for a uid-GaN membrane. Then 20 nm of $Al_{0.2}Ga_{0.8}N$ was grown at 1050 °C as an etch-stop layer for the PEC etching, followed by the growth of 10 nm of uid-GaN. On top of the uid-GaN, the InGaN quantum dots were grown at 710 °C by modified droplet epitaxy method [22, 23]. After the QD growth, a 10 nm GaN capping layer was then grown at the same temperature as the InGaN QDs in N_2, followed by a further, 20 nm of uid GaN for a p-i-n junction, or 60 nm of uid GaN for an uid-GaN membrane, grown at 1000 °C using H_2 as the carrier gas. For growing a p-i-n junction, the final growth of 30 nm of p-GaN at 950 °C completed the material structure. The anneal process for the p-GaN was carried out at 785 °C in N_2 for 20 minutes. The growth and anneal conditions for the p-GaN have been previously demonstrated not to damage the QDs [56] and have also been shown to have no measureable effect on the sacrificial superlattice for the compositions used here. The final material structure is shown in Figure 1.22.

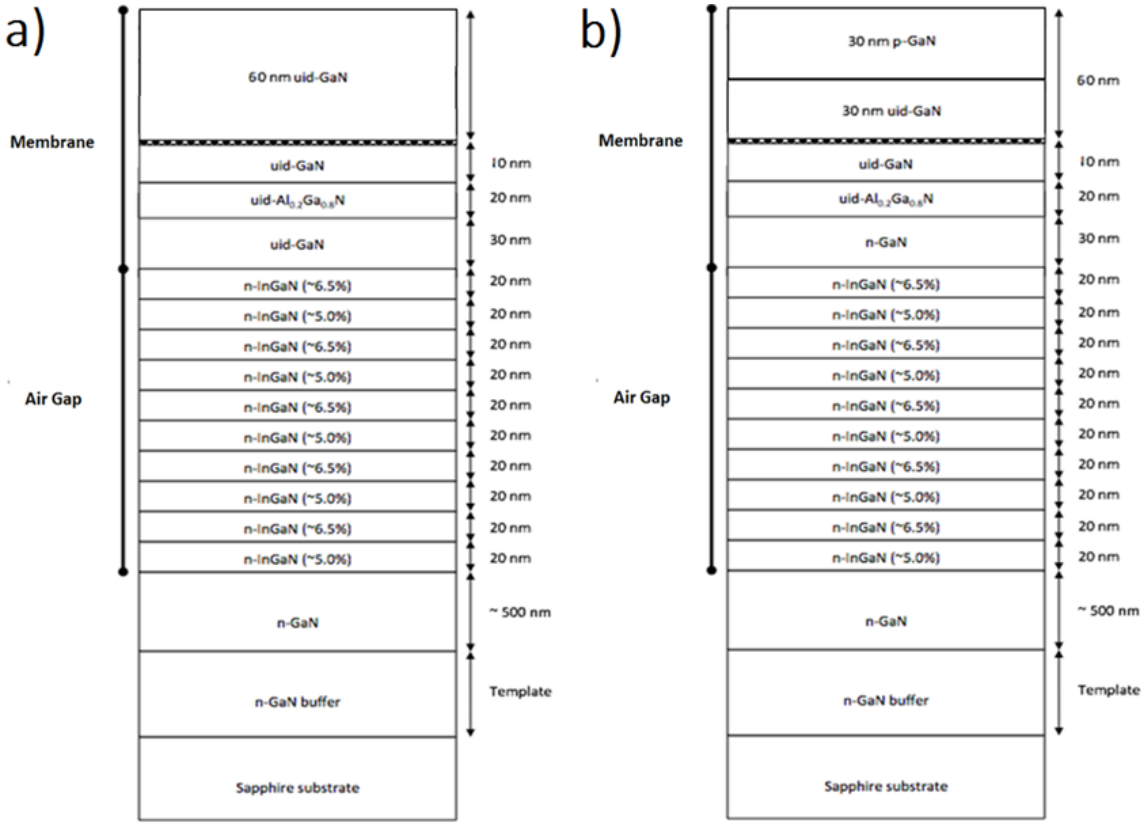

Figure 1.22 (a) Material structure for a 120nm uid-GaN with 1 layer of InGaN QDs on InGaN-InGaN SSL grown on c-GaN LDD template. (b) Material structure for a 120nm p-i-n GaN with 1 layer of InGaN QDs on InGaN-InGaN SSL grown on c-GaN LDD template.

(3) 200 nm p-i-n GaN with 3 layer of InGaN active media (QW and QDs) and on InGaN-InGaN SSL grown on Si-doped LDD c-GaN template.

This growth of this p-i-n sample started with a standard Si-doped LDD GaN template [29]. An n-doped (1×10^{18} cm^{-3}) $In_{0.065}Ga_{0.935}N/In_{0.05}Ga_{0.95}N$ (20 nm - 20nm period, 200 nm total depth) sacrificial superlattice structure was then grown and capped by 50 nm of n-GaN (5×10^{18} cm^{-3}). Then 20 nm of $Al_{0.2}Ga_{0.8}N$ was grown at 1050 °C as an etch-stop layer for the PEC etching,

followed by the growth of 20 nm of uid GaN on top of which three layers of InGaN active medium (QW or QD) were grown at their respective temperature (740 °C for QW or 710 °C for QD using modified droplets epitaxy method) [22, 23, 53] and capped by 10 nm GaN at the same temperature in N_2. The last 10 nm thick GaN cap layer is followed by a 10 nm of uid GaN grown at 1000 °C using H_2 as the carrier gas. A 60 nm thick p-GaN was grown at 950 °C which was followed by another 10 nm p^+ GaN contact layer. The anneal process for the p-GaN activation was carried out at 785 °C in N_2 for 20 minutes [56]. The final material structure is shown in Figure 1.23.

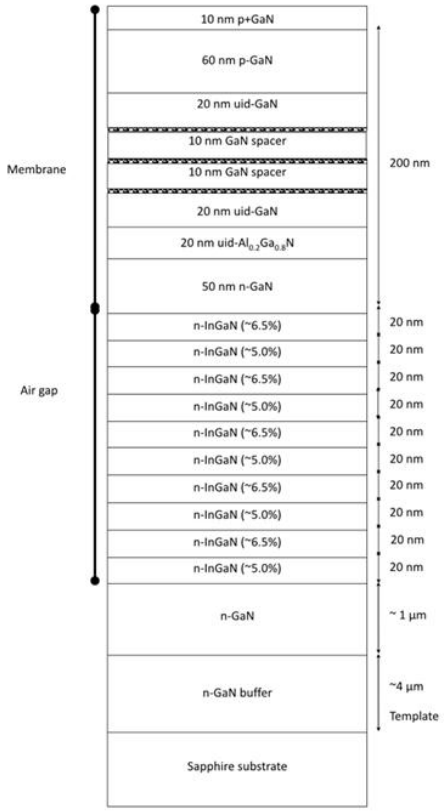

Figure 1.23 Material structure for a 200 nm p-i-n GaN with 3 layer of InGaN QWs on InGaN-InGaN SSL grown on Si-doped LDD c-GaN template.

1.5 Conclusion

Chapter 1 outlines the basic and background information on materials, materials growth, and PEC etching technique that are useful for understanding and fabricating GaN/InGaN optical cavities. GaN and InGaN are young materials compared to conventional semiconductors. As a result, the current quality of material is not defect-free. Moreover, due to limitations set by GaN's chemical inertness, PEC etching is used to selectively remove unwanted layers, however at the same time, residual etch resistant whiskers may be formed, due to TDs. All in all, the tunability of PEC etching allows one to fabricate suspended optical cavities desirably. In the chapters to come, optical micro- and nano-cavities and their applications and the underlying principles will be described in detail.

CHAPTER 2: **GaN/InGaN Microdisk and Applications**

2.1 Microdisk Cavity

2.1.1 Background

A microdisk is a simple cavity structure which confines light propagating around its periphery by total internal reflection [57, 58]. The highest quality standing waves, or eigenmodes, of a microdisk are called the whispering gallery modes (WGMs) which often exist in circular resonant systems [59]. WGMs in a microdisk have a two-fold degeneracy corresponding to clockwise and counterclockwise propagation directions. Due to its high quality factor and small modal volume, a microdisk is a great test bed for the sensitive assessment materials quality and for realization of light-matter interactions. Moreover, they are easier to grow and fabricate compared to many other cavity structures, such as micropost cavities and photonic crystal cavity [60].

Finite difference time domain (FDTD) simulations are often performed to study the theoretical limitations and emission patterns of the WGMs of microdisks. A computed 1st order WGM mode profile along with the SEM image of a fabricated microdisk are shown in Figure 2.1. In a microdisk, the principal emission direction is radially in-plane. To avoid mode leakage into the substrate through evanescent wave coupling, the air gap between the microdisk and substrate should be at least half of a wavelength in air. The number of modes and free spectral range are determined by the size of the microdisk. An increase in microdisk size, in radius or in thickness, will lead to an increase in the number of WGMs and a decrease in free spectral range [61]. The wavelength of light in GaN is λ/n, where n, the refractive index, is approximately 2.5 for wavelengths within the general emission region of the InGaN active medium, from 410nm to 490nm.

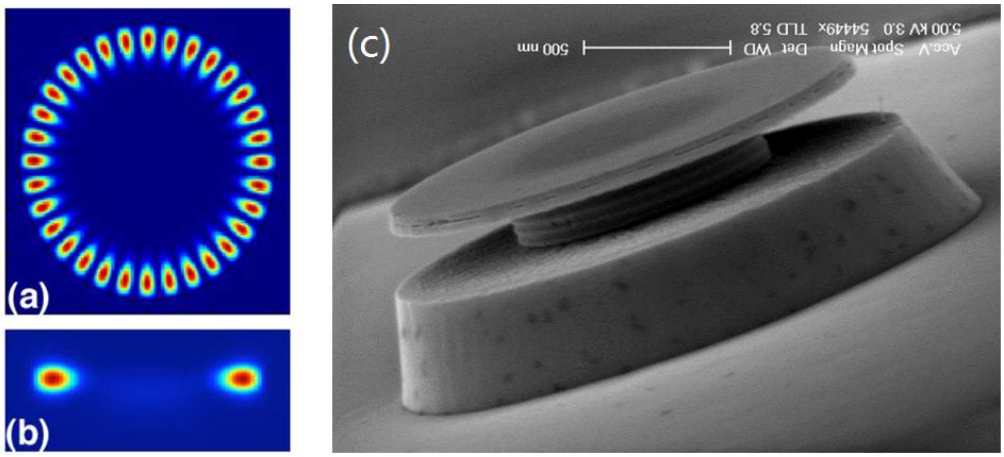

Figure 2.1 (a) Top down view of 1st order WGM of a 2 μm microdisk. (b) Side view of 1st order WGM of a 2μm microdisk. (c) A fabricated unintentionally doped 2 μm GaN/InGaN microdisk.

As with every cavity system, perfect symmetry is critical for obtaining the best Q factor [60, 61]. Microdisks that include imperfections such as surface roughness, defects, and whiskers are susceptible to absorption and scattering which leads to a lower Q factor. Moreover, imperfections and non-circularity can also break the degeneracy of the clockwise and counterclockwise WGMs causing a visible mode-splitting between the principal mode peaks [62]. As a result, it's important to fabricate suspended damage- and defect-free circular microdisks for the best device performance. In a microdisk, due to the slight variation in localization, WGMs can have different quality factors and different susceptibility to defects and imperfections. Higher order WGMs are spatially localized further inside the microdisk. As a result, these modes have a stronger tendency to couple to the post of the microdisk and require greater undercut to become spectrally visible.

Mathematically, computing the resonant modes of a microdisk with radius R and height H requires solving Maxwell's Equations for a cylindrical coordinate system with finite thickness. The derivations can be easily found in available textbooks and journal papers [60, 61]. For the experimental observations on tuning, it is important to point out that spacing between WGMs of the same order, or the free spectral range, is determined by $\Delta\lambda = \lambda^2/2\pi R n_{eff}$, where λ is the mode wavelength, R is the radius of the microdisk cavity, and n_{eff} is the effective refractive index of the mode. Figure 2.2 shows the PL spectrum of a

typical 2 μm unintentionally doped GaN/InGaN microdisk at room temperature. The free spectral range, approximately 17 nm, is clearly shown in the figure.

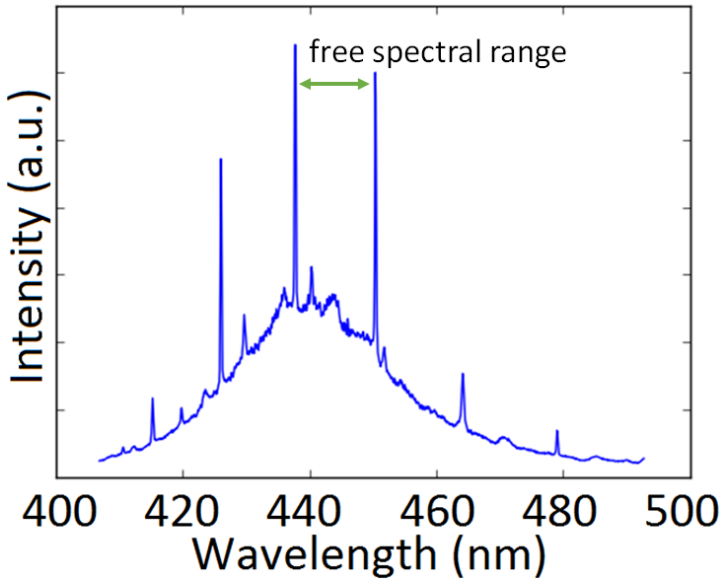

Figure 2.2 PL spectrum of a 2 μm unintentionally doped GaN/InGaN microdisk taken at room temperature. The free spectral range is the separation between 2 adjacent modes of the same order as shown by the arrow indication.

2.1.2 Fundamentals of Lasing

Laser is an acronym for Light Amplification by Stimulated Emission of Radiation. Lasing is a process involving optical amplification of light through stimulated emission [63]. Compared to other light sources, a key characteristic of the laser is spatial and temporal optical coherence in its

emission. Spatial coherence allows a laser beam to remain collimated over a large distance. Temporal coherence allows a laser to emit over a very narrow wavelength range [64, 65].

A two-level system is often useful for quantitative and qualitative description of stimulated emission behavior [66]. An electron can occupy either of the two states E_1 or E_2 separated by an energy gap $\Delta E = E_2 - E_1$ as shown in Figure 2.3. For an electron at the higher energy level E_2, there is only a finite lifetime for which it will remain at E_2 even in the absence of an external field or stimuli. Physically, an electron at E_2 will couple to the vacuum fluctuation field, leading to a spontaneous emission event to relax to the lower level. Moreover, in the case of an external field, for example a photon with frequency equal to the bandgap ΔE, the probability of the electron making a transition to the other energy state is dramatically increased. The electron's transition from state E_1 to state E_2 can be accomplished by the absorption of the photon with energy equal to ΔE. Vice versa, a photon with energy equal to the bandgap ΔE can also stimulate an electron to make a transition from state E_2 to state E_1, emitting an additional photon with the same frequency and polarization, leading to the process of stimulated emission. The transition probability for both absorption and stimulated emission is the same [66]. For such a reason, to generate lasing behavior, it's necessary to prepare the system with more electrons in the higher energy level to produce a net gain for stimulated

emission events. This preparation process is known as population inversion, beyond which a spontaneous emission event will trigger stimulated emissions leading to lasing behavior [63].

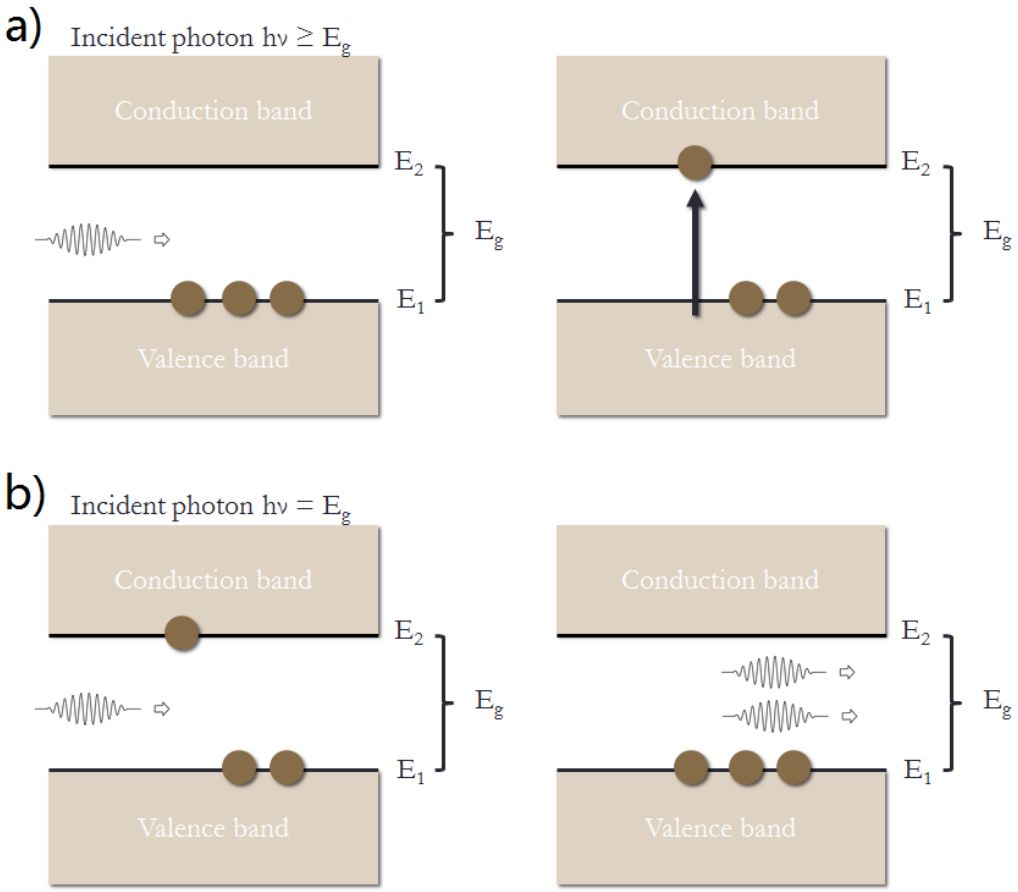

Figure 2.3 Schematic of two level systems with electrons occupying states E_2 and E_1 under the influence of an incoming photon. (a) A two level system with one electron at E_1 absorbs the incoming photon with energy above the bandgap E_g transitioning to state E_2. (b) A two level system with one electron occupying the higher energy state E_2 under the influence of an incoming photon with energy equal to the bandgap E_g produces another identical photon through stimulated emission.

In the ideal two-level system model, only radiative transitions are considered. However, non-radiative recombination also exists in which excited electrons relax to the lower energy state without emitting a photon. Examples can be recombination events occurring at defect sites or with surface states. The time in which a non-radiative recombination event occurs is the non-radiative recombination lifetime. For optically active materials, it is important that the non-radiative recombination lifetime is significantly longer than the radiative recombination lifetime [50]. For practical considerations, it is therefore important to grow high quality and low defect materials for the best laser performance.

In a semiconductor laser, the gain medium is often an epitaxially grown material with lower bandgap which traps and confines the electrons and holes in conduction and valence band respectively. The gain medium is excited by an external source with above-bandgap energy, such as with a pump laser, to reach population inversion to trigger lasing. The minimum excitation power necessary to reach lasing action is the lasing threshold [63]. For the GaN/InGaN laser cavities in this dissertation, the gain medium is InGaN QWs, fQWs or QDs. Lasing relies fundamentally on light-matter interaction. Consequently, an optical cavity is useful to increase the intensity of the mode overlapping with the gain medium. In general, cavities with moderately high quality factor and small modal volume are important to making low-threshold

semiconductor lasers [60].

To characterize lasing action, a photon density plot is a necessary tool to determine the onset of lasing and to clearly reveal the three regimes of lasing operation. Figure 2.4 shows two typical lasing curves, a linear photon density vs. excitation power plot in (a), and a log-log photon density vs. excitation power plot in (b). The first regime of lasing operation is dominated by spontaneous emission, in which the gain medium is excited well below the lasing threshold. In the log-log plot, such regime has a constant slope due to linear increase of output intensity with excitation power. As the population of carriers in the excited state increases with increasing excitation power, the rate of stimulated emission becomes comparable to spontaneous emission, which marks the transition to the second regime of operation, amplified spontaneous emission. In both plots, the amplified spontaneous emission region is clearly indicated by an exponential increase in photon population. However, due to large spontaneous emission events involved, the overall photons emitted are incoherent, with random phases and a significant spread in wavelengths. As the excitation power is further increased, the rate of stimulated emission dominates over the spontaneous emission. At this point, the lasing threshold is reached, in which a clear suppression of spontaneous emission is observed in the laser PL spectrum. Using the linear photon density plot, the lasing threshold is determined as the intersection of the horizontal

axis and a linear fit to the higher-power region of the data. Photons emitted from the dominant stimulated emission events are coherent in phase and wavelength. In both of the photon density plots, the lasing intensity vs. excitation power is once again in a linear relationship [63].

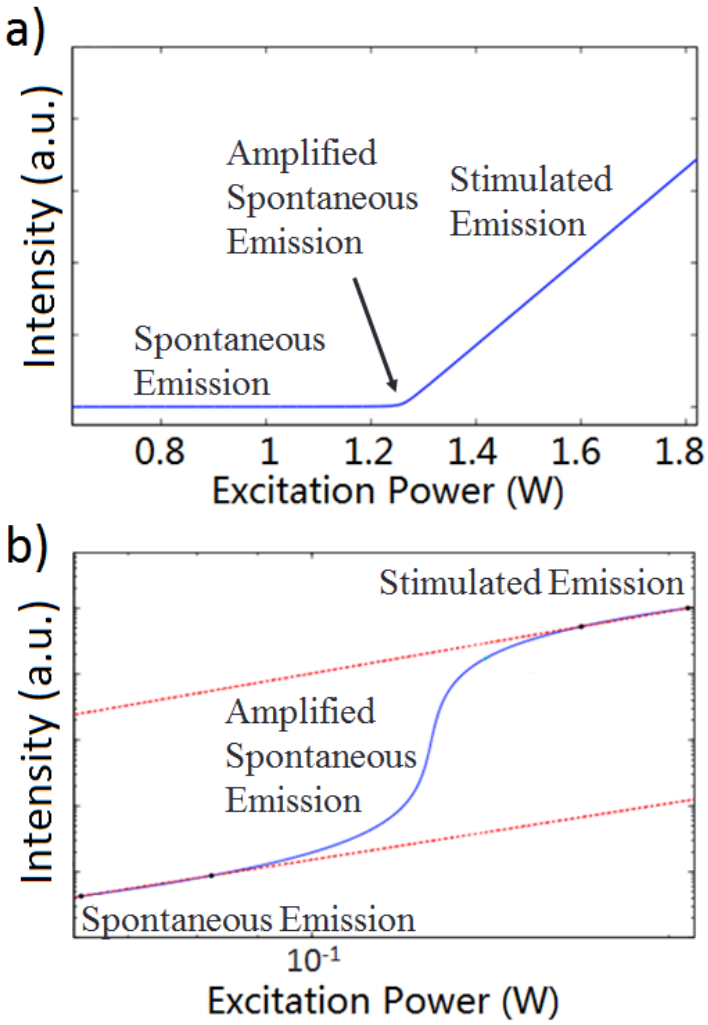

Figure 2.4 (a) A typical linear lasing curve plotting output photon density against external excitation power. (b) A typical log-log lasing curve plotting output photon density against external excitation power. In both plots, three regimes of lasing operation are clearly identified, spontaneous emission, amplified spontaneous emission, and stimulated emission.

2.2 Experimental Results

A substantial amount of work on microdisk fabrication and lasing was carried out among a number of student and postdoctoral researchers. This section summarizes some of the essential lessons learned from that work with respect to the choices of the active layer materials (quantum dots, fragmented quantum wells and quantum wells) described in Chapter 1, and differences in the lasing behavior of microdisk cavities with the different active materials. A typical material structure for these microdisk studies is shown in Figure 1.20 in section 1.4.

Earlier experiments comparing microdisks with either 120 nm or 200 nm thick membranes, showed much higher Q factors for the 200 nm membranes. This experimental observation was confirmed by simulations. Therefore, all cavities for lasing and cavity-QED experiments later employed a 200 nm thick cavity structure. For such 200 nm thick membranes, a record high Q factor of ~ 9100 was demonstrated for 3 μm-diameter microdisks with 3 QD layers in the active region, and single QD layer in the same microdisk structure yielded Q factors as high as 7500. Despite the high Q factors, neither of these microdisks achieved lasing under accessible excitation powers. Forming microdisks of 1 μm diameter, using the same material structure, resulted in immediate observation of room-temperature lasing at 0.28 mJ/cm^2 threshold

power for the 3QD-layers. No lasing for microdisks with a single InGaN QD layer is observed. As a result, the trinity of a small modal volume, a decent Q factor, and a multi-layered active medium is required for achieving lasing action in a microcavity structure.

2.2.1 Fabrication

Cleaning and preparations were necessary before beginning the fabrication process for making GaN/InGaN microdisks. Initially, the wafer (5 mm × 5 mm) was sonicated in Acetone and IPA for 3 minutes each, followed by a 30 minutes cleaning in piranha and then a 3 minutes buffer oxide etch to remove the surface oxides. Immediately after cleaning, SiO_2 beads of a selected size suspended in IPA were dispensed onto the wafer surface. The beads served as masks for the subsequent inductively coupled plasma (ICP) etch of the material in 25 sccm of Cl_2 and Ar gas for an approximate depth of 520 nm. The SiO_2 beads were subsequently removed in BOE and Acetone/IPA sonication. PEC etching in 0.004 M HCl was then performed to selectively etch the $In_{0.065}Ga_{0.935}N/In_{0.05}Ga_{0.95}N$ superlattice, forming the final microdisk structures. Figure 2.5 is a schematic showing the fabrication flow. Figure 2.6 shows the SEM image of a resulting microdisk with 200 nm thick cavity membrane. The active medium is 3 layers of InGaN QDs which are located in

the middle of the disk membrane sandwiched by the GaN barrier layers.

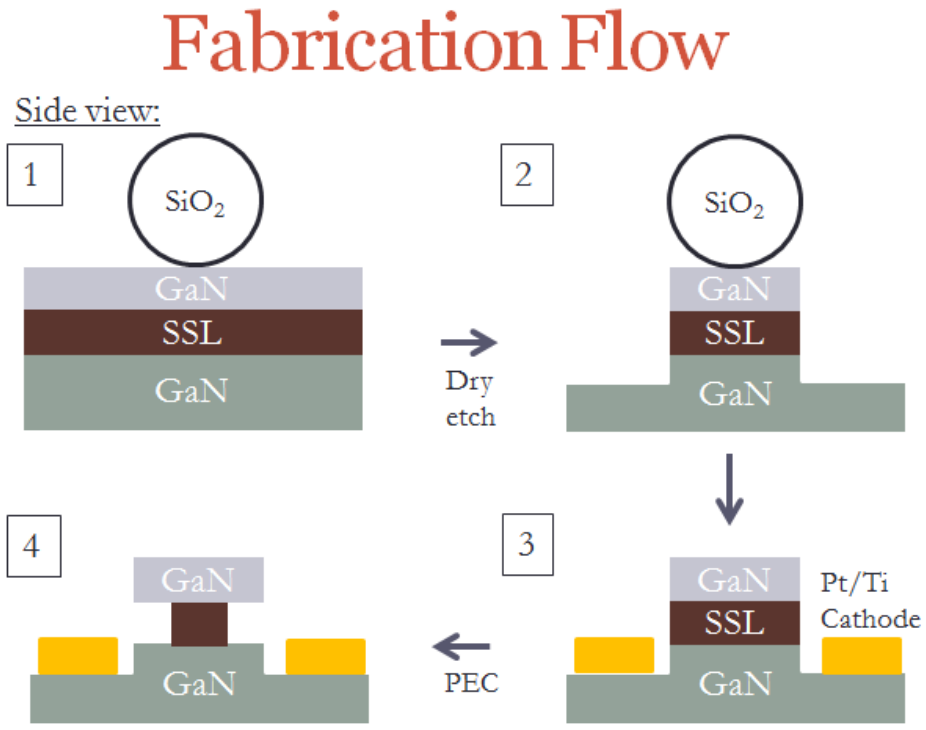

Figure 2.5 Fabrication flow for making GaN/InGaN microdisks.

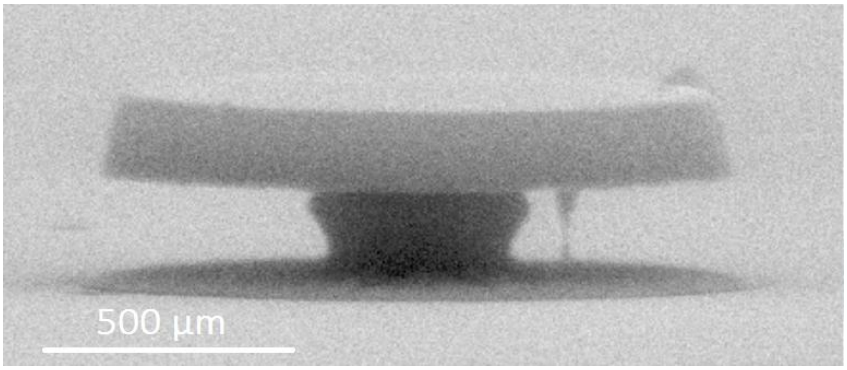

Figure 2.6 SEM image of a 1 µm diameter GaN/InGaN microdisk with 200 nm thick cavity membrane, fabricated using the process flow outlined in Figure 2.5. The active medium is 3 layers of InGaN QDs, located in the middle of the disk membrane sandwiched by the GaN barrier layers.

2.2.2 Photoluminescence Characterization

Optical characterization of microdisks was performed using a frequency-doubled titanium sapphire laser emitting at 380 nm, an energy below the bandgap of GaN but above the bandgap of the InGaN QDs, through a long working distance objective (×100, numerical aperture (NA) = 0.5). The beam radius is approximately 290 nm. The emission from the microdisks was collected through the same objective and directed into a spectrometer for analysis. The full schematic of the PL set-up is illustrated by Figure A.1 in Appendix A.

Figure 2.7 (a) shows the PL spectrum taken at room temperature from a 1 μm diameter microdisk with 3 layers of QDs. Figure 2.7 (b) shows a high resolution spectrum of the transverse electric (TE) mode at 475.8 nm. This mode exhibits a splitting between the two degenerate WGMs, most likely due to imperfections and lack of complete rotational symmetry. These two modes are fitted with Lorentzian functions, as indicated with the red and green lines, through which a Q factor of ~ 6600 is extrapolated.

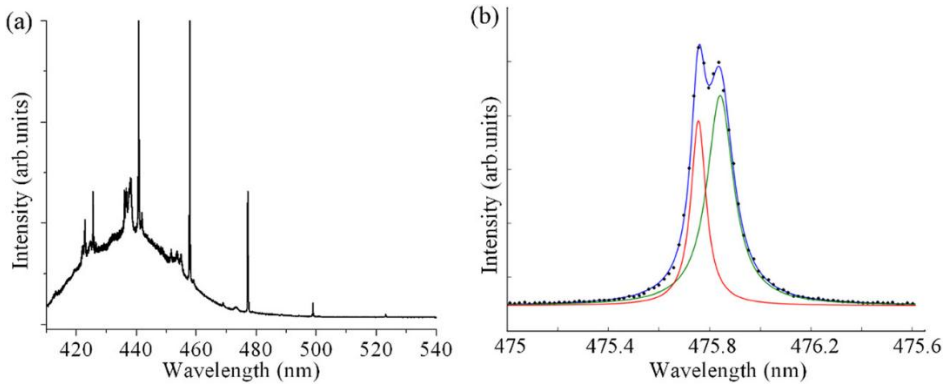

Figure 2.7 (a) Room temperature PL spectrum of a 1 μm diameter microdisk with 3 layers of QDs. (b) High resolution spectrum of the transverse electric (TE) mode at 475.8 nm with splitting between the two degenerate WGMs. Q factor of ~ 6600 is extrapolated by using Lorentzian function fitting [49].

2.2.3 Microdisk Lasing

Extensive characterization was undertaken of the 1 μm diameter microdisks, to compare the differences in lasing behaviors, for the QD, fQW and QW active layer materials. The signature of room temperature lasing was clearly observed from all three samples, as shown in Figure 2.8. Multiple WGMs are visible under low power excitation. As the excitation power was increased through the lasing threshold, the intensity of a single mode increased dramatically and dominated over all other modes and spontaneous emission. Pronounced narrowing of the lasing mode was observed, signifying the increased temporal coherence of emission in the lasing regime [49, 55]. The

log-log photon intensity vs. excitation power plots are shown in the insets indicating clear achievements of lasing actions with all three regimes of operation, spontaneous emission, amplified spontaneous emission, and stimulated emission, as described in section 2.12. Moreover, no clear dependence between the lasing thresholds and the Q factors was observed.

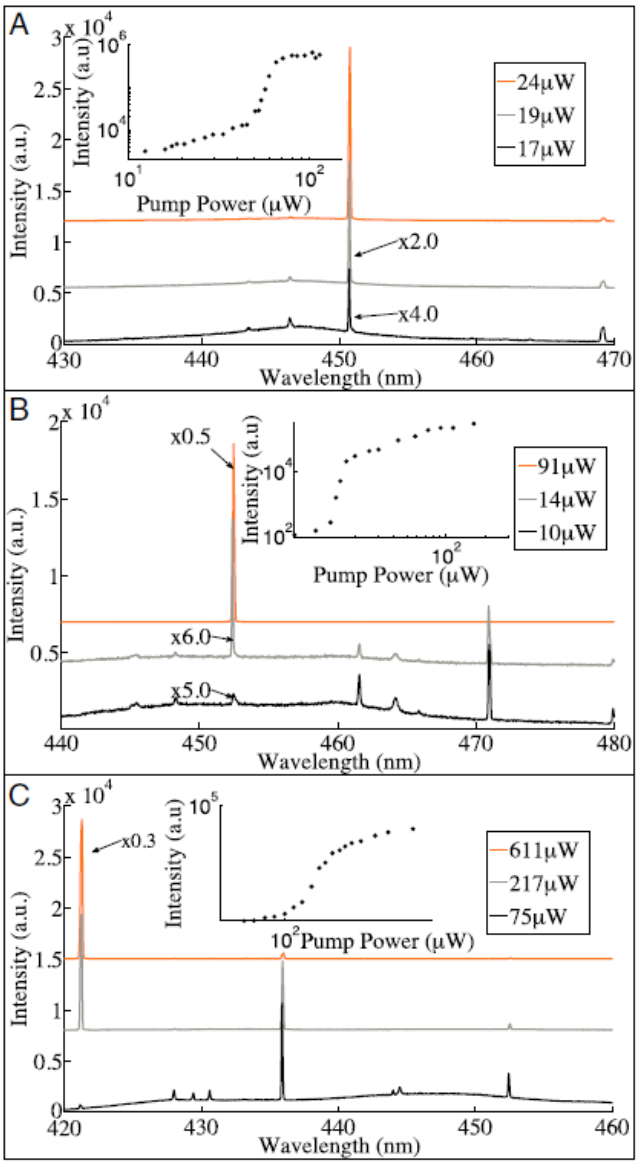

Figure 2.8 Lasing spectra from 200 nm thick GaN/InGaN microdisks with 3 layers of (a) QWs (b) fQWs (c) QDs. Insets show the log-log lasing curves demonstrating the three regimes of laser operation [49, 55].

For the QW microdisk, the lasing mode appeared near the peak of background luminescence at low excitation power and remained its spectral position through lasing. For the fQW microdisk, the dominant mode rested at the long-wavelength side of the background luminescence (~471 nm) under low power excitation. By increasing excitation power through threshold, an initially less visible mode close to the background emission center (~452 nm) became dominant and reached lasing. For the QD microdisk, a dominant mode initially appeared near the center of the background luminescence (~436 nm) under low power excitation. Increasing the excitation power caused a distinctive transition to occur in which the WGM with the shortest wavelength (~421 nm) abruptly became dominant and, with further increased excitation power, achieved lasing action. Alex Woolf et al. (2015) demonstrated that the observation of the blue shifts in the lasing modes for microdisk cavities with fQW and QD gain materials is due to an interplay between and relative importance of the carrier capture cross-section versus the radiative emission efficiency of the fQW regions and QDs of varying size [49, 55].

The table in Figure 2.9 summarizes the averaged data for the center of the gain emission, the lasing wavelength, and the lasing threshold for three samples. Microdisks with 3 layers of QWs offered the best performance in terms of lasing thresholds, possibly due to the larger density of electronic states and better coupling between the emitters and cavity modes. These QW

microdisks also had more consistent lasing thresholds due to homogeneity of the gain medium and better uniformity of the overall material quality. In comparison, microdisks with 3 layers of fQWs lased with a wide range of thresholds. This observation can be attributed to the variation in the areal distribution and composition of the annealed fQWs which caused inconsistencies among microdisks in their material properties. Microdisks with 3 layers of QDs exhibited more consistent lasing thresholds with a significantly lower average compared to the fQW microdisks. As pointed out in earlier discussion, the number of QDs in spatial and spectral resonance with the WGMs was likely limited, however, moderate lasing thresholds were achieved. This could be attributed to the lower threshold carrier density required for QDs compared to conventional QWs [67]. Nevertheless, QW gain material produced lasers with best consistency and lowest average threshold. Consequently, InGaN QW is comparatively the most promising choice of compatible gain material for a GaN microdisk laser.

Sample	Average center λ of background (nm)	Average λ of lasing mode (nm)	Average lasing threshold (μW)	Threshold range (μW)
QW	446 ± 2.3	448 ± 6.7	184	88-375
fQW	457 ± 3.5	451 ± 6.7	753	83-3600
QD	441 ± 4.8	428 ± 3.8	303	118-815

Figure 2.9 Lasing statistics by averaging over the 20 microdisk lasers measured for each of the QW, fQW, and QD samples [55].

2.3 Tuning Application

2.3.1 Introduction and Observation

For cavity-QED and light-matter interaction experiments, it is necessary to realize both spatial and frequency resonance of emitter to cavity modes. One challenge is in the ability to tune the cavity mode to spectrally match the emission of the emitter of interest. A variety of methods has been employed to tune cavity modes in other semiconductor materials (e.g. GaAs) and are mostly based on the modification of the local refractive index of the cavity. Temperature tuning of photonic crystal cavities (PCCs) using gas condensation has been previously demonstrated [68]. In a different approach, deposition of thin photosensitive layer on top of the cavity (such as chalcogenide [69] or spiropyran [70]) is performed. Upon laser irradiation, the refractive index of the layers is modified, resulting in a tuning of the cavity modes. Alternatively, chemical digital etching which slightly modifies the cavity dimensions was also demonstrated [71]. Since there is a different temperature dependence of the QD emission energies and that of the optical modes, change of temperature has been used to effect tuning [72]. Better controlled local tuning has been achieved by employing heating pads positioned in a close proximity with the PCC [73].

An *in situ* method of tuning InGaN/GaN microdisk cavities is described in this

section. The technique arose from an observation made during a PL measurement for a set of uid GaN/InGaN microdisks with 1 layer of QDs (material structure shown in Figure 1.22 (a) in section 1.4): an unexpected non-reversible blue-shift of the WGMs. It was initially believed to be an oxidation effect due to exposure of the cavity to moisture in air. As a result, PL measurement and tuning was tested by immersing the microdisks in de-ionized water (DI-water) and irradiating the microdisk with a UV laser (360 or 380 nm) excitation. The diameter of the laser beam was approximately 500 nm. The SEM image of the microdisk is shown in Figure 2.10 (a). Modes with quality factor (Q) as high as 3500 were measured as shown in the PL spectrum in Figure 2.10 (b). Tuning of the WGMs was achieved and continued as long as the laser was focused on the disk. Only the probed microdisks underwent the tuning while other cavities on the sample remained unaffected. By measuring cavity PL spectrum during tuning, one was able to continuously monitor the evolution of the WGMs and dynamically control them.

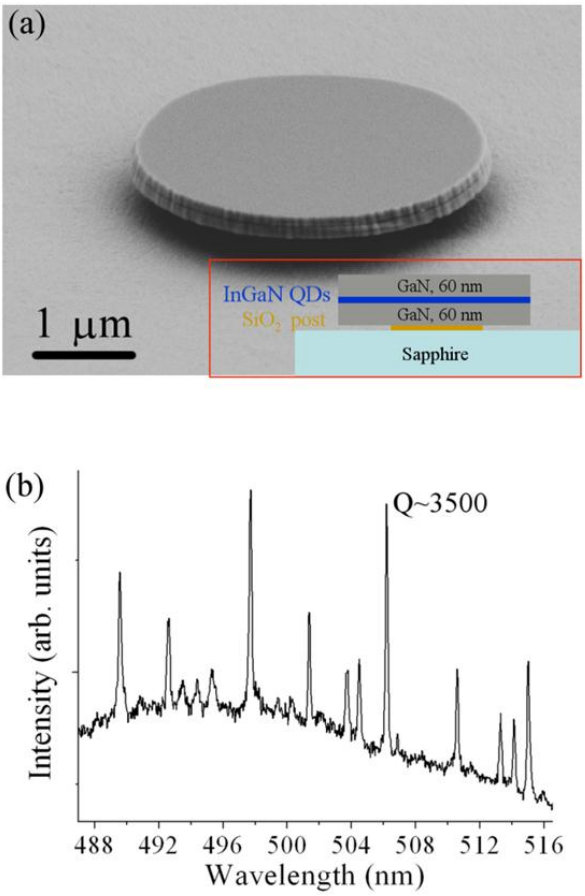

Figure 2.10 (a) SEM image of an InGaN/GaN microdisk with inset showing the cavity's material structure. (b) Room temperature PL spectrum of the microdisk [74].

To further understand the observed effect, the same microdisks were immersed in DI-water within a small cell, composed of a hollow rubber ring (1 mm height) in between two cover glass slides. The sample was excited and imaged through the top cover slide. Figures 2.11 (a) – (c) show the tuning of the WGMs, achieved by continuous irradiation of the disk with two different excitation powers of 0.2 mW (a) and 0.9 mW (c) using the 360 nm wavelength excitation laser. A faster rate of blue-shift in WGMs was observed under higher power excitation. It was

noted that the rate of tuning was directly related to the applied excitation power. To further understand the mechanism underlying the tuning, the microdisks were immersed in a non-polar solvent, toluene. The samples were subjected to 20 minutes of continuous irradiation at 80 μW power with 360 nm excitation laser. No tuning was observed, providing more evidence that the observed process was indeed related to oxidation in the aqueous environment.

The same tuning operation was repeated using a 380 nm excitation wavelength, which corresponded to an energy below the bandgap of the GaN but above the bandgap of the InGaN QDs. Figures 2.11 (b) and (d) show the results of the mode tuning employing 0.3 mW and 1 mW of excitation power. Comparing the two excitation schemes, it was clear that tuning rate using the 380 nm laser excitation was considerably slower than that observed for the 360 nm excitation. With excitation power of ~ 1 mW, a 1.9 nm mode shift was observed under 380 nm laser excitation, while a shift of up to 3.5 nm was observed under 360 nm excitation. The tuning was even slower employing low excitation powers as shown in Figure 2.11 (b) and was halted when the power decreased to ~ 50 μW. Finally, the WGM shift was permanent and non-reversible. By and large, these data collectively suggest the possibility of developing this observed effect into a deterministically and precisely controlled permanent tuning technique for WGMs in a GaN/InGaN microdisk.

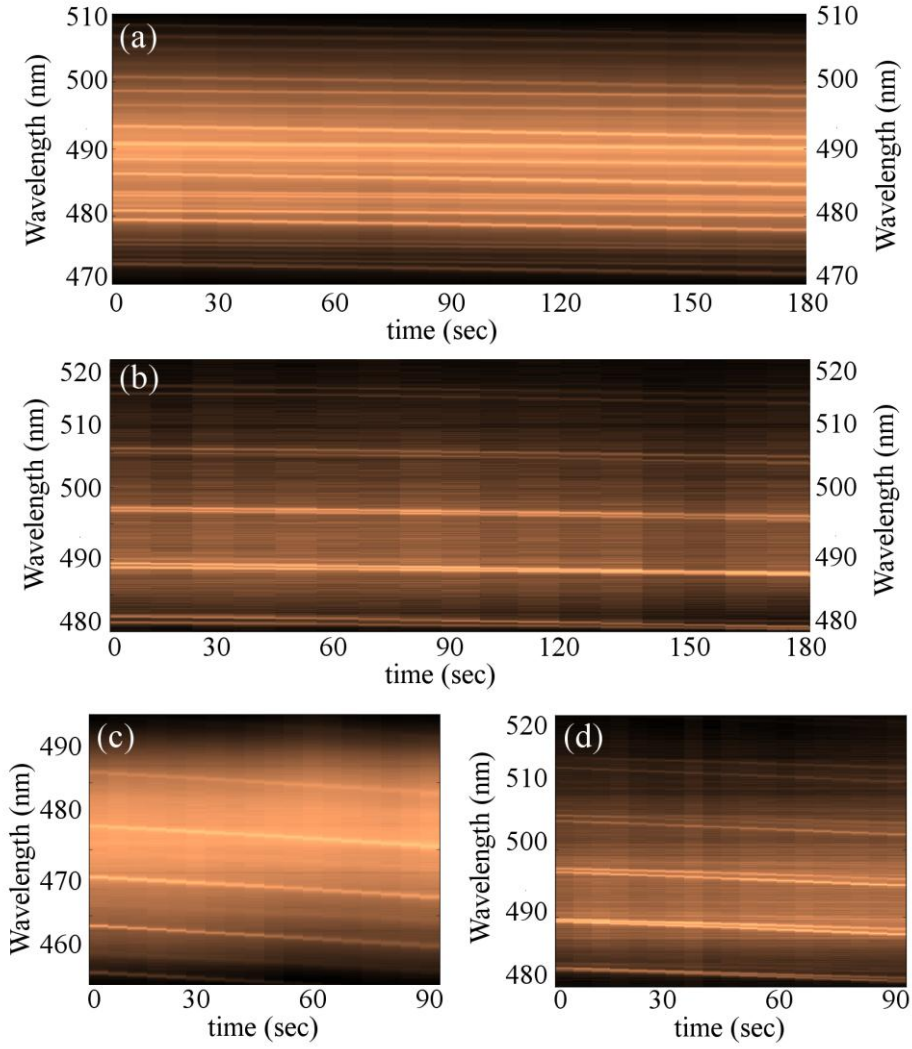

Figure 2.11 Tuning of the WGMs of InGaN/GaN microdisks immersed in DI-water with (a) 360 nm excitation wavelength with 0.2 mW and (c) 0.9 mW excitation power. (b) 380 nm excitation wavelength with 0.3 mW and (d) 1 mW excitation power. The bright lines present peaks of the WGMs [74].

Figures 2.12 (a) and (b) show two PL spectra recorded dynamically during the tuning after 5 sec (black curves) and 100 sec (red curves) using 360 nm and 380 nm laser excitation, respectively. A degradation of Q factor for the 360 nm tuning process was clearly observed. However, only a minor change in Q factor

occurred for the 380 nm tuning, even for a comparable shift in wavelength.

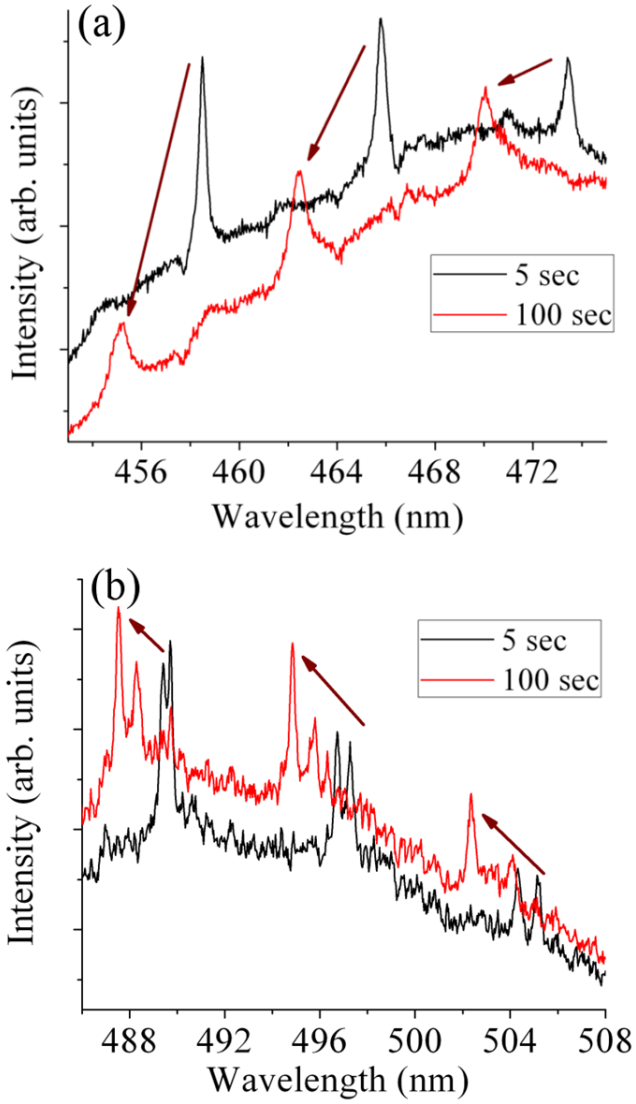

Figure 2.12 PL spectrum recorded in-situ after 5 s and 100 s of tuning of the WGMs with (a) 360 nm and (b) 380 nm laser excitation. The dark red arrows indicate the direction of the mode shift [74].

The mechanism of tuning was believed to be a process similar to PEC etching of GaN, in which photo-generated holes enhanced oxidation of the GaN, and where the oxide was subsequently dissolved in the DI-water. The consistent

blue shift of the modes with increased tuning power and time suggested a reduction in the size of the microdisks. In addition, there has been a previous report of PEC oxidation of n-GaN in water, under an applied bias > 2 V [74]. In this case, photo-oxidation likely took place resulted in a thin layer of oxide which was subsequently dissolved in DI-water, resulting in a precise etch removal of the microdisk material thereby causing a blue-shift in the cavity modes.

The mechanism of the *in-situ* tuning also accorded well with the wavelength-dependence of the tuning. Excitation at 360 nm would generate electron-hole pairs throughout the volume of the microdisk membrane. Generated carriers would readily diffuse to all the microdisk surfaces, resulting in a faster and fairly isotropic photo-oxidation and etching of the periphery of the disk, as well as the surfaces. For excitation at 380 nm, below the bandgap of the GaN, electron hole pairs would only be generated within the InGaN QDs layer creating a smaller carrier concentration compared to the case for 360 nm laser excitation. At low incident powers, the photo-generated carriers would likely be confined in the InGaN region, and thus no hole-enhanced surface oxidation was observed. At high powers, band-filling occurred in which the electrons and holes could escape the confinement of the InGaN region and would drift and diffuse to the microdisk surfaces leading to oxidation and etching. Given the direction of the internal fields of GaN, photo-oxidation/etching would take place

predominantly on the top (Ga-face) surface.

COMSOL software was used to simulate the shift in wavelength of the modes with respect to change in dimensions of the microdisk. A change of 10 nm in the radius of the microdisk produced only a 1 nm shift in the mode wavelength, while a 10 nm change in the thickness of the microdisk, resulted in approximately 7 nm wavelength shift of the WGMs. Thus an isotropic etch of the disk, with a reduction in both the thickness and diameter of the disk would exhibit a mode shift very nearly equal to an etch that affected only the thickness of microdisk. The WGMs can be sensitive to the quality of the etched sidewalls. Thus, for a similar observed mode shift, the isotropic etch process associated with the 360 nm excitation has a greater impact on the symmetry and quality of the microdisk sidewalls. As demonstrated experimentally, a larger degradation of Q was observed for the 360 nm tuning process. For such reason, excitation at 380 nm was employed for further experiments on tuning and its calibrations.

To experimentally validate the occurrence of local GaN etching during photo-irradiation of the material surface by 360 nm or 380 nm laser in DI-water, a well-controlled experiment was carried out. A grid pattern, as shown in Figure 2.13 (a), was dry-etch transferred onto another sample of the same material by inductively coupled plasma (ICP) etching in 25 sccm of Cl_2 and Ar gas for an

approximate depth of 200 nm. The squares were the etched area and the grid bars were protected by a mask, which was subsequently removed. Following the grid fabrication, PMMA C6 was spun onto the sample, and Raith 150 Electron Beam Lithography was subsequently used to expose 1 μm circles aligned to the middle of the grid intersections, visible as the bright spots in Figure 2.13 (a). After chemical development, the circles became holes thereby exposing the underlying GaN surface. The sample was then immersed in DI-water and the areas exposed by the hole were irradiated with 360 nm laser with ~ 50 μW power for 1 minute. After the irradiation, the PMMA was removed in Acetone.

AFM was used to map the surface profile of the etched area, as shown in the inset of Figure 2.13 (b). A trench had been formed in the illuminated regions, and roughly 13 nm of GaN material had been removed. This experiment unambiguously demonstrated the successful etching of GaN by irradiating the material in DI-water, validating the observation for the tuning of the microdisk WGMs.

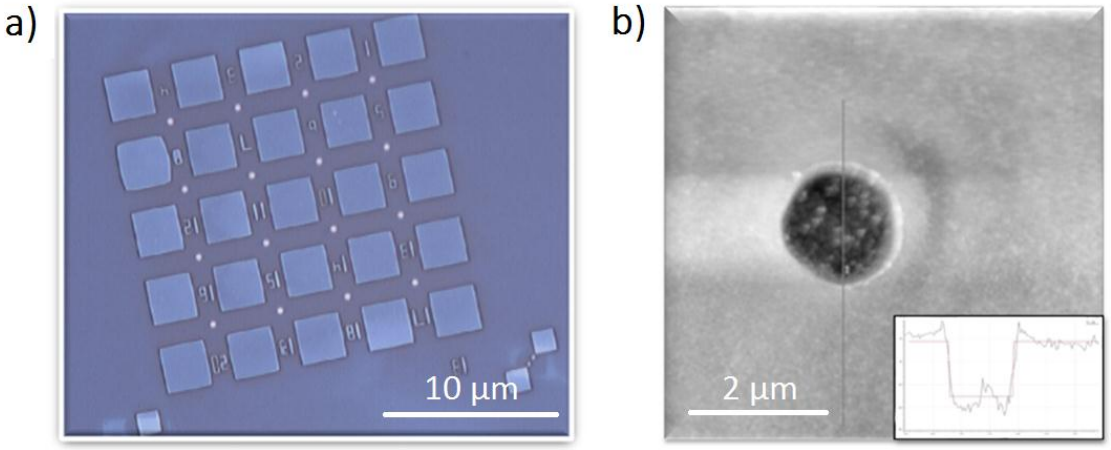

Figure 2.13 (a) Dry-etch transferred grid pattern of GaN covered in PMMA C6. The bright spots are 1 µm diameter holes defined using Raith 150 Electron Beam Lithography. (b) AFM scan of an etched area. Inset shows a line measurement for depth profile of the etched area.

2.3.2 Tuning on P-I-N Microdisks

Through experiments with different material structures, it was found the tuning technique was most effective when applied to p-i-n microdisks. A free spectral range tuning of the WGMs was achieved without any degradation of the Q factors. Moreover, despite the lower powers used in these experiments, the tuning rates achieved (in wavelength shift/incident power/time) were substantially higher than previously achieved. The precise experimental procedures and observations are discussed below.

120 nm-thick, 2 µm diameter p-i-n GaN/InGaN microdisks with 1 layer of QD

(material structure shown in Figure 1.22 (b) in section 1.4) were fabricated. Figure 2.14 (a) shows a SEM image of the microdisk. The InGaN QD active layer is located in the middle of the disk membrane sandwiched by the p- and n-doped GaN layers as shown in Figure 2.14 (b). Figure 2.14 (c) shows a room temperature PL spectrum from the microdisk. Distinct modes could be seen decorating the broad background emission of quantum dots. The Q factor of the first order WGMs were ~ 1500.

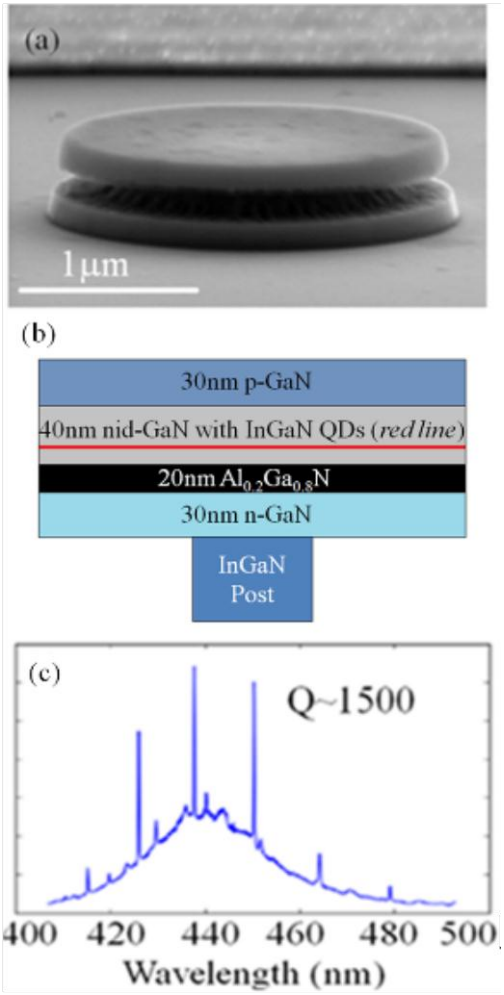

Figure 2.14 (a) SEM image of the InGaN/GaN microdisk. (b) The material structure of microdisk. (c) PL spectrum recorded from the disk showing the first order WGMs with Q approximately 1500 [75].

The microdisks were immersed in water within the same cell set-up used for the first tuning experiment and subjected to illumination with 380 nm laser beam directly incident onto the p-GaN of the disk structure. After illumination in water for a given incident power and time, the microdisks were removed from the cell and dried. A spectrum of the microdisk was then taken in air to more precisely determine the shift in the mode. Moreover, it was ascertained that direct illumination of microdisks in air does not induce a mode shift. Figure 2.15 (a) details the shift of a given mode for 60 seconds illumination at incident powers of 150 nW, 450 nW, and 960 nW, respectively, all measured directly underneath the focusing objective. Figure 2.15 (b) shows the shift in a mode as a function of time, measured at a constant laser power of 450 nW. In both cases, the linear shift in mode wavelength with time, at constant power, or with power at a constant time, provides the possibility of deterministic tuning of one WGM into resonance with a quantum dot transition. Figure 2.15 (c) is a histogram of 'normalized' tuning rate in nanometers (of wavelength shift)/incident power/time of each of 15 different tested microdisks. The standard deviation of the rates falls within 13% of the rate value. This result shows homogeneity in the tuning process and implies that the material properties among different locations of the sample were relatively uniform.

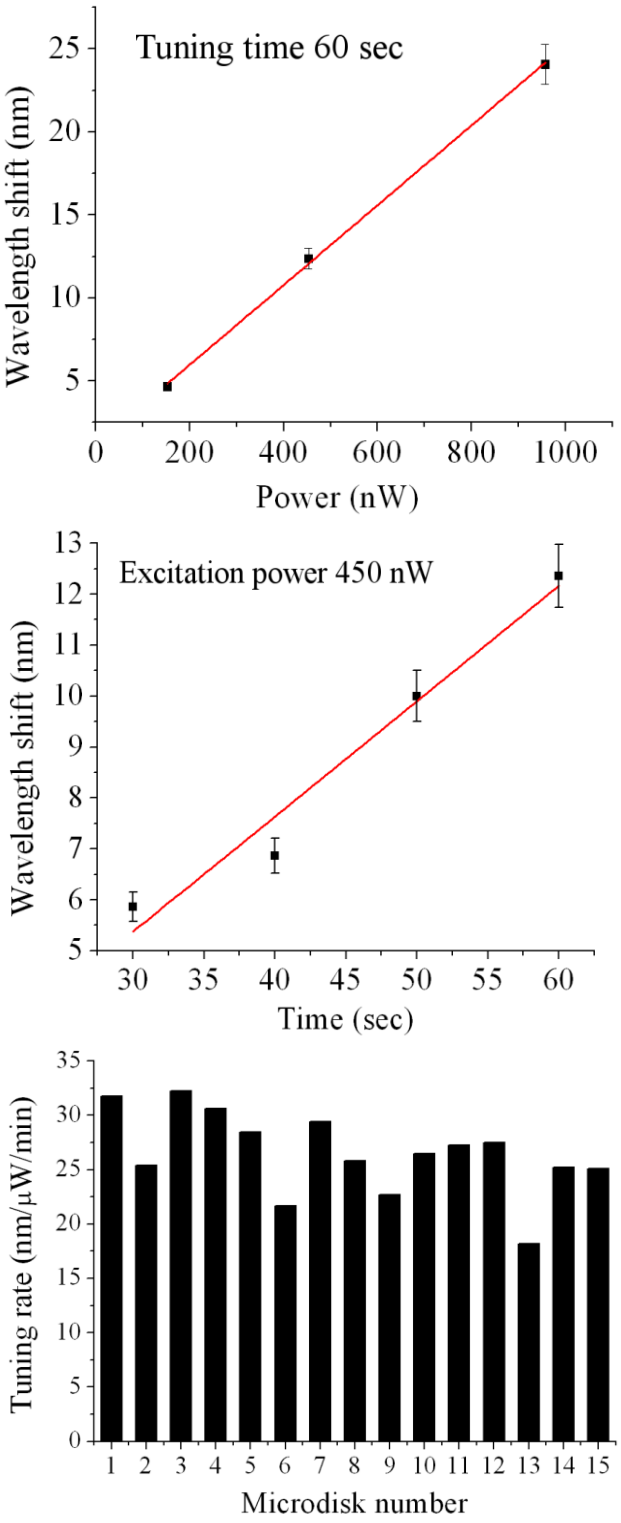

Figure 2.15 (a) A plot showing tuning range vs. different excitation powers with constant tuning time of 60 seconds. (b) Plot showing tuning range vs. time with constant power of 450 nW. (c) A histogram of normalized tuning rates (nm/μW/min) of 15 microdisks [75].

To further demonstrate the precise control of WGM shifts possible with this technique, full spectral range tuning on several microdisks was attempted. A chosen microdisk was tuned in 5 consecutive 10-second intervals. After each tuning cycle, the sample was taken out of DI-water, dried and a spectrum was taken in air. The results are displayed in Figure 2.16. The spectra are offset in the y-direction, for clarity, and the bottom spectrum is the PL signature of the disk before tuning was commenced. The subsequent spectra represent the changes after successive additional 10 seconds of tuning. The shadowed box highlights the evolution of a selected WGM. As the arrow indicates, this mode was tuned from its original wavelength to the emission line of the initial adjacent mode. No Q degradation is observed.

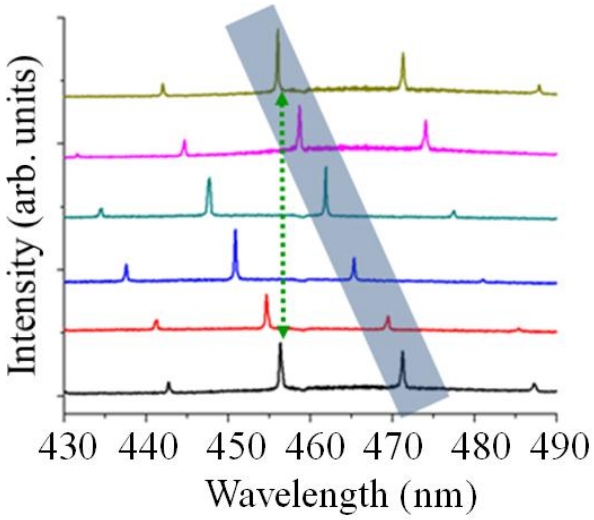

Figure 2.16 PL spectrums of microdisk cavity over 50 seconds of tuning under power ~450 nW with 380 nm laser. The bottom spectrum was taken before tuning. The arrow indicates tuning one WGM over one free spectral range. The shadow box indicates the evolution of the WGM. The times interval before each spectrum is 10 s from bottom to top [75].

To directly validate the occurrence of microdisk surface etching, a measurement experiment was carried out by masking a portion of the microdisk to mark changes in its geometry during the water-based tuning process. A masking structure 80 nm in diameter was formed by electron beam lithography using Fox-16™ resist. The mask was designed to prevent photo-induced changes in the underlying material, and is placed at the center of the microdisk to avoid overlapping with the WGMs, as shown in Figure 2.17 (a). The microdisk was then placed in the water cell and subjected to 450 nW illumination for 60 seconds. After the laser irradiation, the sample was removed from the cell and immersed in buffered oxide etch (BOE, 7:1 NH_4F:HF) for 1 minute to completely remove the mask. Atomic Force Microscopy (AFM) was then done on the microdisk to characterize the surface roughness. Figure 2.17 (b) shows the AFM trace in the vicinity of the original mask. The masked region was ~8 nm higher than the surrounding surface, indicating that the top surface of the microdisk was etched during the tuning process.

PL of the microdisk after the tuning showed a 14.2 nm blue shift in one selected WGM. COMSOL simulations modeled the mode shift expected for the microdisk having an 8 nm reduction in vertical dimension for the microdisk membrane. The result of the simulation indicated a blue shift of ~13.9 nm in the selected WGM. The close correspondence between the simulation and experimental results suggest that only the top, p-type GaN was etched during

this process.

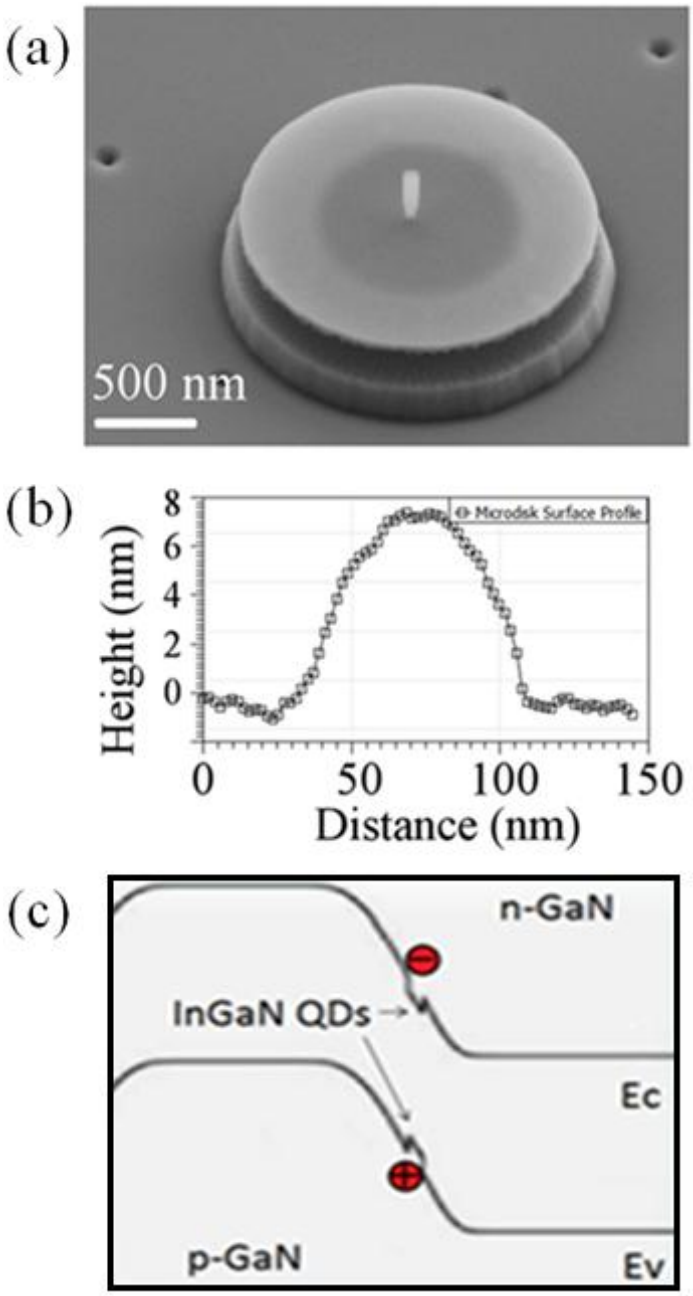

Figure 2.17 (a) SEM image of the InGaN/GaN microdisk with FOx™ resist mask. (b) AFM scan of microdisk top surface profile in the vicinity of the removed resist mask. (c) A simplified bandstructure of a p-i-n junction of disk membrane. The QWs in middle represent the QD layer. The red dots with plus and minus sign represent hole and electron excited by laser, respectively [75].

As stated in Section 2.3.1, it is believed that the tuning process is similar to PEC etching of GaN; it is notable that in the experiments, the light was incident on the p-GaN material of the microdisk, and that generally p-type semiconductors are not etched in PEC processes. However, our 380 nm laser excitation generated electron-hole pairs only in the lower bandgap quantum dot layer, not in the surrounding GaN. Under these conditions, as Tamboli et al. have shown [76], PEC etching can be used effectively to etch the p-GaN. Figure 2.17 (c) shows a simplified bandstructure of a p-i-n junction representing the disk membrane. Electron-holes pairs were generated in the quantum dot layer. The natural band-bending of the structure and the rather shallow confinements of the electrons and holes enabled the holes to drift and diffuse to the p-GaN surface, enhancing oxidation and subsequent etching. The photo-generated electrons were similarly swept to the n-GaN side of the material. One believes that the mechanism described above underlies the rapid tunability, with substantial mode shifts and yet with no degradation of quality factor. By contrast, under illumination of 360 nm radiation at only 120 nW power for only 10 s, the mode shift observed was about 6 nm, but the Q is degraded from 1200 to 450. In this case, electron-hole pairs were generated throughout the volume of the microdisk. However, a preferential etching of the underlying n-GaN and the disk periphery was observed. Even though a change in the radial dimension of the microdisk produces a far smaller mode shift than a commensurate change in the thickness, the effect of a change in the radial symmetry on the cavity Q-

factor can be significant. A SEM image of a heavily irradiated (at 380 nm) p-i-n microdisk is shown in Figure 2.18. Prolonged laser tuning thinned the disk membrane and created moderate surface roughness, which led to the eventual degradation of the cavity Q factor.

In comparing the tuning of these p-i-n structures with the uid structures characterized earlier, tuning of the modes was achieved at substantially lower powers: 200 nW to 1 μW, for either 360 nm or 380 nm incident wavelength, compared to the few hundred μW to ~ 1 mW incident powers used for the uid microdisks. Illumination of the uid structures at 50 μW power and 380 nm produced no tuning at all. While the histogram of Figure 2.15 (c) shows average tuning rates of ~ 20 nm/μW/min for the p-i-n microdisks, the tuning rates for the uid microdisks were 3 to 4 orders of magnitude less. Thus the bandstructure of the cavity material, relative to the excitation wavelength played an important role in determining the predictability and control of the tuning process.

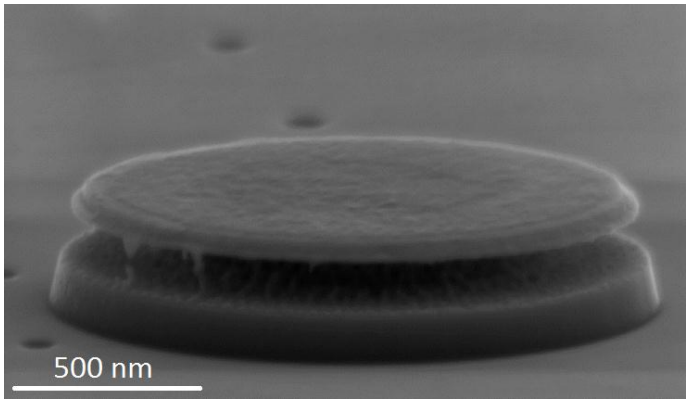

Figure 2.18 SEM of a p-i-n GaN/InGaN microdisk irradiated by 380 nm laser with 20 μW power for 3 minutes.

Applying this tuning technique on p-i-n GaN/InGaN microdisks resulted in a greater than one free spectral range blue-shift tuning of the WGMs without degradation of their Q factor. With the linear dependence on the applied excitation power and the fine controllability, this technique constitutes an important step in achieving spectral resonances of WGMs with embedded emitters, crucial for studying cavity QED and realizing optoelectronic devices.

2.4 Conclusion and Future Work

In this chapter, background information of microdisk cavity is introduced in detail. With the growth and fabrication ability, high Q factor GaN/InGaN microdisks with QW, fQW, and QD active media were successfully fabricated which led to observation of lasing. Ideally in the near future, GaN/InGaN materials with reduced defect density can be grown to further improve the device performance and cavity Q factor. Through numerous characterization and lasing experiments with the GaN/InGaN microdisks, an optimized material structure was found: 200nm thick cavity membrane with 3 layers of gain materials. This structure was used as a baseline for extensive studies on GaN/InGaN microdisk lasers. Due to the low threshold lasing observed in these microdisks, one believes electrically driven operation can be an

interesting avenue of exploration, making these devices more suitable for further applications. Moreover, for the tuning technique and experiment, a natural extension would be to apply such controlled technique to create permanently coupled microdisks in a deterministic manner. Both of these two future directions are described in detail in the following sections.

2.4.1 Electrically Injected Microdisk

In this chapter, all microdisks lasers have been optically excited. Optical injection is a critical step for demonstrating lasing and a useful method for studying cavity and material properties. However, electrical injection is essential for practical applications [77]. Building the apparatus for electrical injected microdisk represents a challenge due to the requirement for metal contacts which, if in direct contact with the cavity, represent a major source of optical absorption and loss. As a result, careful design and sophisticated fabrications are required.

Figure 2.19 shows the schematic of a proposed electrically injected p-i-n GaN/InGaN microdisk with 3 layers of QWs structure. The structure of the material is shown in Figure 1.23 of section 1.4. 1 μm microdisk was fabricated from this p-i-n material and achieved lasing with an unadjusted threshold of ~

150 uW of excitation power, which is approximately two times higher than the lowest threshold observed in the uid GaN/InGaN microdisks with 3 layers of QWs.

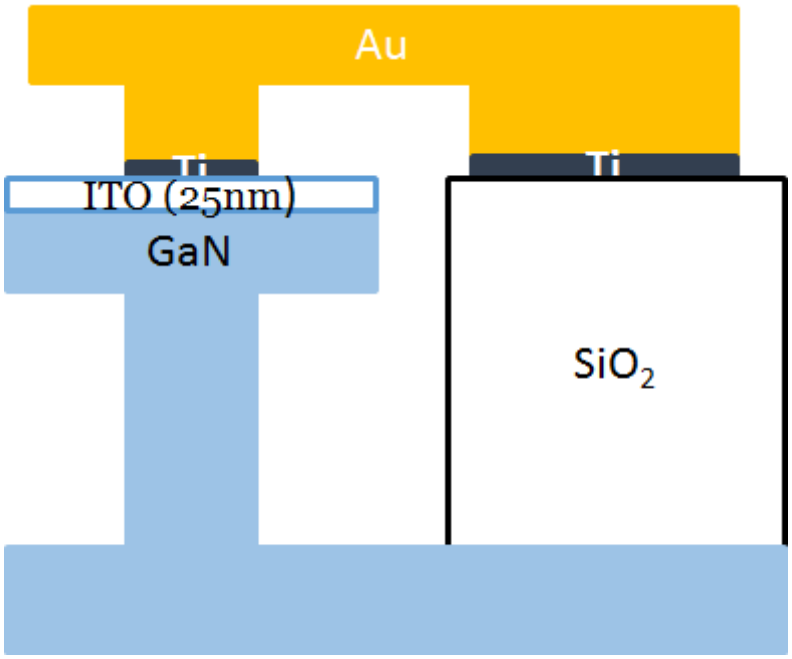

Figure 2.19 Schematic of an electrically injected p-i-n GaN/InGaN microdisk with 3 layers of QWs.

Fabrication of the proposed structure in Figure 2.19 involves numerous steps with high precision alignment. As a result, a well-defined alignment marker for electron beam lithography is necessary. First, 25 nm of indium tin oxide (ITO) is sputtered onto the cleaned GaN wafer and annealed at 500 °C for 1 minute to render the ITO transparent with regard to the emission range of the InGaN QWs. PMMA C6 is then spun onto the sample and baked at 180 °C to form a spacer layer for resist lift-off. FOx™ 16 resist is subsequently spun onto

the PMMA-covered sample and baked at 90 °C. Elionix 125 Electron Beam Lithography (Elionix) is used to define 2 μm diameter disks, which are subsequently developed. Unaxis ICP RIE is used to etch the sample in 25 sccm of N_2 and Cl_2 for an approximate depth of 520 nm. The sample is then sonicated in acetone to remove the spacer layer lifting off the FOx™ 16 resist mask. A cathode, patterned by photolithography, of Pt (50 nm)/Ti (5 nm) is evaporated onto the sample surface using Denton EE-4 Metal Evaporator (EE-4). PMMA is spun onto the sample again, and using the Elionix, large square openings aligned to the microdisk (2 μm from the edge of the microdisk) are exposed and developed for sputtering and lifting off the SiO_2 stands as shown in the schematic of Figure 2.19. The height of the SiO_2 is level with the top of the ITO. The sample is ready to be etched in 0.004 M HCL using PEC to undercut the microdisks. Figure 2.20 shows a SEM image of a 1 um diameter GaN/InGaN microdisk with 25 nm of ITO on top. Q-factor of ~ 2300 is measured on first order WGMs.

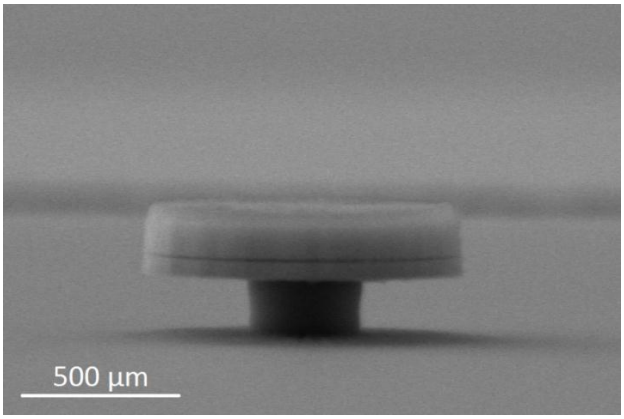

Figure 2.20 SEM image of a 1 um diameter GaN/InGaN microdisk with 25 nm of ITO on top.

The last step of the fabrication process is to form the metal arm structure on top of the microdisk as the p-contact of the electrical injection apparatus. The metal arm is suspended therefore will not adversely affect the Q factor of the microdisk. Nevertheless, this step requires high precision alignment. A simple process flow is shown in Figure 2.21. First, PMMA C6 is spun onto the sample. Using Elionix, a circle with 500 nm diameter and an opening with smaller areal dimension compared to the SiO_2 stand are aligned to the middle of the microdisk and SiO_2 stand, respectively, exposed and developed as shown in Step 1 of Figure 2.21. It is important to note the 500 nm circle will serve as the mold for the metal post of the metal arm, facilitating the injection of carriers into the microdisk. Therefore it is necessary to position the circle in the middle of the microdisk to avoid coupling of the WGMs to the metal post. Following this step, LOR-3A is spun onto the sample and baked at 90 °C for 30 minutes. LOR-3A serves as a blocking layer for PMMA chemical development following the next E-beam exposure. PMMA C6 is spun onto the sample again and baked at 90 °C for 30 minutes. A 1.5 μm circle and another opening with smaller areal dimension compared to the first exposed opening are aligned to the middle of the microdisk and SiO_2 stand, respectively, and exposed. Following this initial exposure, a bar structure bridging the 1.5 μm circle and the opening are exposed as shown in Step 2 of Figure 2.21. The sample is developed, first in MIBK:IPA (1:3), then in CD-26 Shipley Photoresist developer to partially remove the LOR-3A to connect the two

developed PMMA patterns for metal evaporation to form the final metal arm structure. Thermal Evaporator is used to evaporate 25 nm of Ti as a sticking layer followed by 250 nm of Au. Subsequent lift-off in remover PG at 80 °C is needed to complete the proposed structure shown in Figure 2.19. A wire bonder will be used to connect the Au on top of SiO_2 stands as the p-contact and the floor level of the microdisk as the n-contact. This experiment will be an interesting high-impact future direction for the p-i-n GaN/InGaN microdisks.

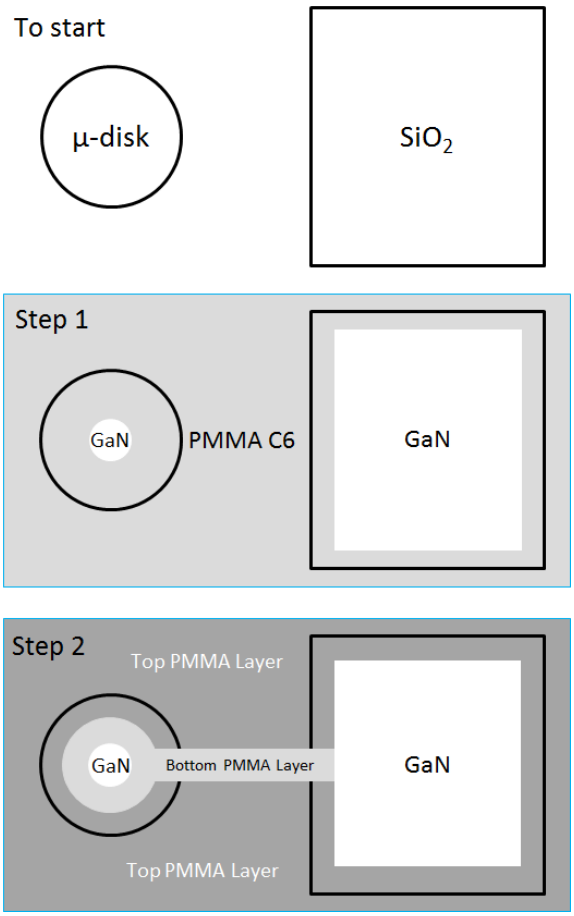

Figure 2.21 A simple process flow for creating the resist mold to evaporate and lift-off the metal arm structure for electrical injection of the GaN/InGaN microdisk.

2.4.2 Coupled Microdisks

Coupled microcavities can form “photonic molecules” (PM) with analogous properties compared to confined electronic states [78 - 81]. The size and arrangement flexibility of coupled microdisks (CMs) offers advantages to create arbitrary PMs exhibiting unique optical properties [78]. Moreover, lasing, coupled mode-mode splitting, and optical bistability have previously been demonstrated in GaInAsP CMs [78, 82]. GaN/InGaN is an excellent material system for creating CMs operating in the blue spectrum. A fabrication process is developed to create twin GaN/InGaN microdisks with minimal distances (~ 50 nm). Using the water tuning technique, it is possible to spectrally match selected resonances of the twin cavities to form permanently coupled GaN/InGaN microdisks.

FDTD simulation is performed on coupled 2 μm-diameter GaN microdisks with different separations. The microdisks that are coupled are modeled to be identical. Figure 2.22 (a) shows the simulation of a CM with 30 nm spacing. As the inset shows, a mode-mode splitting of 0.2 nm is observed. Figure 2.22 (b) and (c) show the antisymmetrically and symmetrically coupled (first order) mode-mode profiles, signature of a strong interaction between the twin cavities. Comparable to electronic systems, the antisymmetric mode has slightly larger energy therefore is represented by the peak with the shorter

wavelength after splitting occurs. It is found that WGMs with longer wavelengths have stronger coupling strength due to the larger leakage of evanescent fields. Moreover, increasing separation between the CMs dramatically decrease the mode-mode splitting and significantly lowering the coupling strength. Figure 2.22 (d) shows a diagram for simulated mode-mode splitting strengths of the first order WGMs of CMs with different separation distances. Longer wavelength modes exhibit stronger coupling therefore larger mode-mode splitting due to slightly larger evanescent fields. CMs with separation larger than 100 nm have minimally discernable coupling (< 0.1 nm).

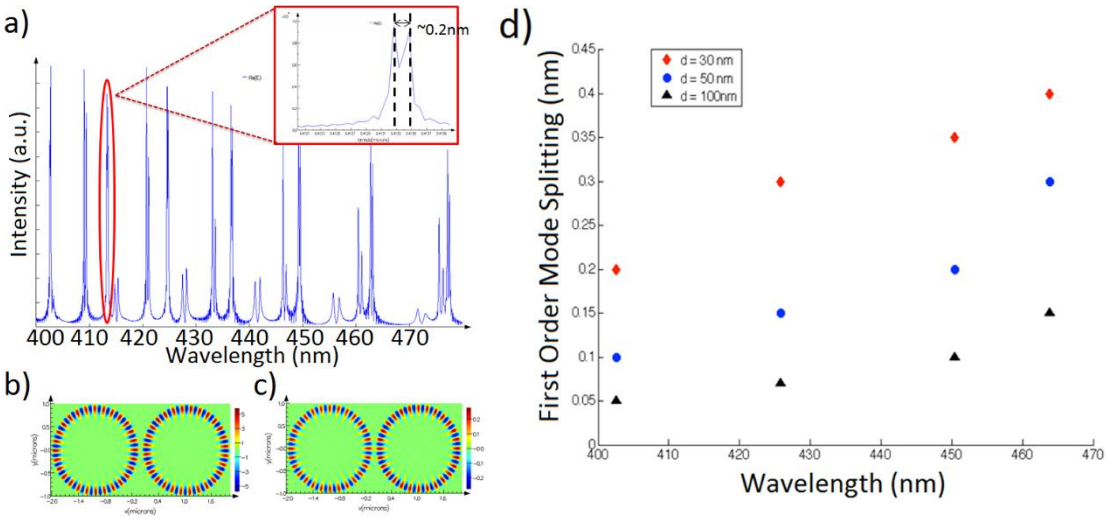

Figure 2.22 FDTD simulation of 2 μm coupled identical GaN microdisks with 30 nm of separation. (b) Antisymmetrically coupled mode-mode profile. (c) Symmetrically coupled mode-mode profile. (d) Diagram for simulated mode-mode splitting strengths for CMs of different separations.

The fabrication flow for 2 μm-diameter GaN/InGaN CMs with 3 layers of QDs

is identical compared to fabricating a single microdisk except for the choice of mask which requires an extra preparation and lithographic step. The mask for coupled microdisks is FOx™ 16 resist which is exposed using Elionix. Due to charging and proximity effect it is difficult to achieve a separation spacing smaller than 200 nm without distorting the circularities of the CMs. However, as illustrated by Figure 2.22 (d), in order to observe coupled mode-mode splitting, it is necessary and critical to minimize the distance between the twin GaN/InGaN microdisks to around 50 nm to enhance evanescent coupling. As a result, a conductive scheme for E-beam lithography is adopted which consists the deposition of a 5 nm SiO_2 diffusion prevention layer followed by the E-beam evaporation of a 10 nm Ti conductive layer onto the surface of the GaN wafer before applying the FOx™ 16 resist. With this new fabrication recipe, 2 μm-diameter circular coupled microdisks with the shortest interdisk separation of ~ 50 nm are successfully fabricated. Figure 2.23 (a) shows a SEM image of 200 nm thick, 2 μm-diameter GaN/InGaN coupled microdisks with 3 layers of QDs.

Room temperature PL measurement are performed on the GaN/InGaN CMs. Figure 2.23 (b) and (c) show the PL spectra of the microdisk on the left and right, respectively. Due to fabrication flaws, surface roughness, and other material imperfections, a 2 nm offset is measured between the positions of the corresponding WGMs in each disk. Such offset value is an order of magnitude

larger than the linewidths of the WGMs, therefore preventing any overlapping spectral interactions between the cavities. Experimentally demonstrating coupling between the CMs requires controllably tuning a selected WGM of one microdisk into resonance with the targeted WGM of the twin microdisk. Using the well-developed tuning technique outlined in the previous section 2.3.2, it is possible to achieve permanent strong coupling between these CMs without any degradation of the cavities' Q factors. Fine tuning will be required to accurately match the WGMs of interest. Low power laser excitation in DI-water will offer a uniform slow tuning rate for the microdisk, and through which, tuning with sub-nanometer precision can be achieved. This experiment will be an interesting future direction which involves low risk and minimal uncertainties. Only a limited number of steps are needed beyond those already accomplished.

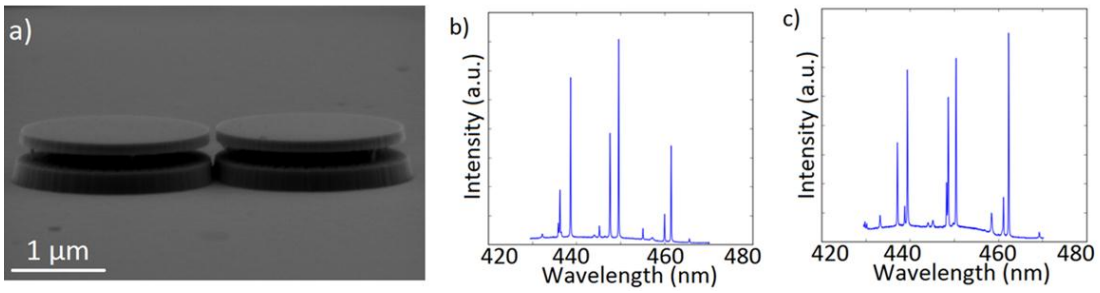

Figure 2.23 SEM image of 200 nm thick, 2 µm-diameter GaN/InGaN coupled microdisks with 3 layers of QDs. Separation between the microdisks is determined to be ~ 50 nm. (b) PL spectrum of the microdisk on the left (c) PL spectrum of the microdisk on the right.

CHAPTER 3: GaN/InGaN Photonic Crystal Nanobeam and Applications

3.1 Background

In the recent years, photonic crystal (PC) cavities [83, 84] have attracted great interests from the engineering and scientific communities because of their small wavelength-scale modal volumes and ultra-high Q factors, achievable and adjustable through careful designs [85 – 87]. These advantages provide an ideal platform for experimentally realizing light-matter interactions [88] and applications such as lasing [89, 90], quantum information processing [91], nonlinear optics [92], and others [93 – 95]. PC nanobeam can be an ideal cavity structure for certain material systems due to its 1-D geometry and smaller footprints [96], which can greatly simplify the fabrication process. Qimin Quan et al. (2010) proposed a deterministic method for designing PC nanobeams with ultra-high Q factors, which ideally resulted with (i) zero extended cavity length between the middle mirrors, (ii) constant periodicity ('periodicity = a'), and (iii)

a Gaussian-like field attenuation profile [97]. The coupling loss to the feeding waveguide is reduced by using more than 15 periods of mirrors on each side of the nanobeam symmetrically. The optical energy is concentrated in the dielectric region in the middle of the cavity [96].

Figure 3.1 (a) and (b) respectively show the schematic of nanobeam used in FDTD simulation and the table summarizing the design parameters for two nanobeam designs used in this dissertation. The refractive index for GaN is ~ 2.5 for wavelengths in InGaN emission range. The particular cavity design comprises a ridge waveguide perforated with gratings of cylindrical holes designed using the deterministic high-*Q* method [96, 97]. The nanobeam cavity from each of the two designs has a unique resonant mode frequency, Q-factor, and modal volume (V), and is selected to spectrally match to the principal emissions of the gain media for the intended application. For instance, as observed in microdisk cavity system, lasers with QDs as gain material achieved lasing at a shorter wavelength of ~ 428 nm on average, yet in comparison, QW and fQW microdisks lased within a longer wavelength range, approximately from 445 to 455 nm. Nanobeam of design 1 has a resonant mode at 437 nm with a Q factor of ~ 118,000 and a modal volume of ~ 1.5 $(\lambda/n)^3$. Nanobeam of design 2 has a resonant mode at 420 nm with a Q factor of 101,000 and a modal volume of 1.7 $(\lambda/n)^3$. Both designs use the same beam length of 5.2 μm with the same periodicity and membrane thickness of

130 nm and 200 nm, respectively. Moreover, design 1 uses a beam width of 130 nm whereas design 2 uses a 125 nm width. FDTD simulation of the intensity profile of the resonant mode at 420 nm for design 2 is shown in Figure 3.1 (c). The mode is concentrated and confined within the small volumes of the semiconductor material, between the inner etched holes.

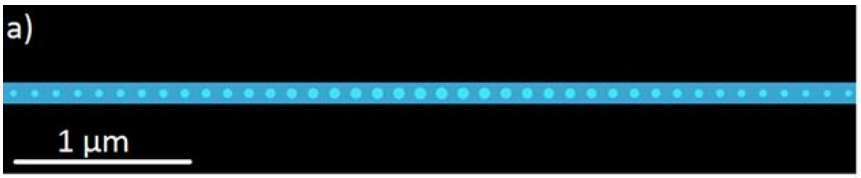

b)

Hole Radius (nm)	Design I *Mode at 437 nm*	Design II *Mode at 420 nm*
Inner hole	36.0	41.0
hole 2	35.2	40.2
hole 3	34.3	39.3
hole 4	33.5	38.5
hole 5	32.6	37.6
hole 6	31.8	36.8
hole 7	30.9	35.9
hole 8	30.1	35.1
hole 9	29.3	34.3
hole 10	28.4	33.4
hole 11	27.6	32.6
hole 12	26.7	31.7
hole 13	25.9	30.9
hole 14	25.1	30.1
hole 15	24.2	29.2
hole 16	23.4	28.4
hole 17	22.5	27.5
hole 18	21.7	26.7
hole 19	20.8	25.8
Outer hole	20.0	25.0

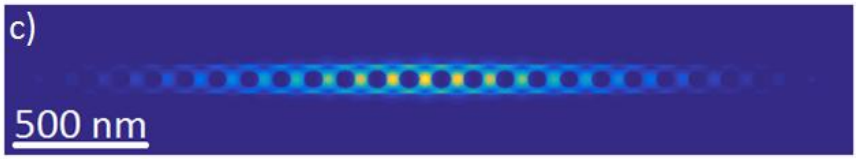

Figure 3.1 (a) Schematic of the nanobeam in FDTD simulation. (b) Table summarizing the design parameters for two nanobeam designs with modes at 437 nm and 420 nm. The refractive index for GaN is ~ 2.5. (c) FDTD simulated resonant mode intensity profile for nanobeam mode at 420 nm (design 2).

3.2 Experimental Results

3.2.1 Fabrication

Figure 3.2 shows a schematic of the fabrication flow. As described in Chapter 2, it is necessary to clean and prepare the GaN/InGaN sample before beginning the fabrication process. Initially, the wafer (5 mm × 5 mm) is sonicated in Acetone and IPA for 3 minutes each, followed by a 30 minutes cleaning in piranha and then a 3 minutes buffer oxide etch to remove the surface oxides. A conductive scheme for E-beam lithography is used again which begins with the deposition of a 5 nm SiO_2 diffusion prevention layer followed by the E-beam evaporation of a 10 nm Ti conductive layer onto the surface of the wafer before applying the XR-1541 (XR) E-beam resist. Elionix F-125 electron beam lithography (Elionix) is then used to define the nanobeam and circular pad which serve as masks for the subsequent inductively coupled plasma (ICP) etch in 25 sccm of N_2 and Cl_2 gas for an approximate depth of 300 nm. Subsequently, FOx-16 resist is spin-coated and the Elionix is again used to define a large rectangular pad aligned to the dry-etched nanobeam and circular pad. This pattern is subsequently dry-etched to a depth of approximately 200 nm, using the same conditions as described above. Figure 3.3 (a) shows a SEM image of the dry-etched transferred mesa. This allows access to the InGaN/InGaN superlattice, which is then selectively

removed by the PEC etch in a solution of 0.004 M HCl. Critical point drying is used to avoid adhesion of the nanobeams to the substrate during the drying process. This produces the final suspended photonic crystal nanobeam structure shown in Figure 3.3 (b) and (c): the top-down and side-view SEM images of a 200 nm thick PC nanobeam cavity. No significant imperfections and whiskers near the cavity region are observed.

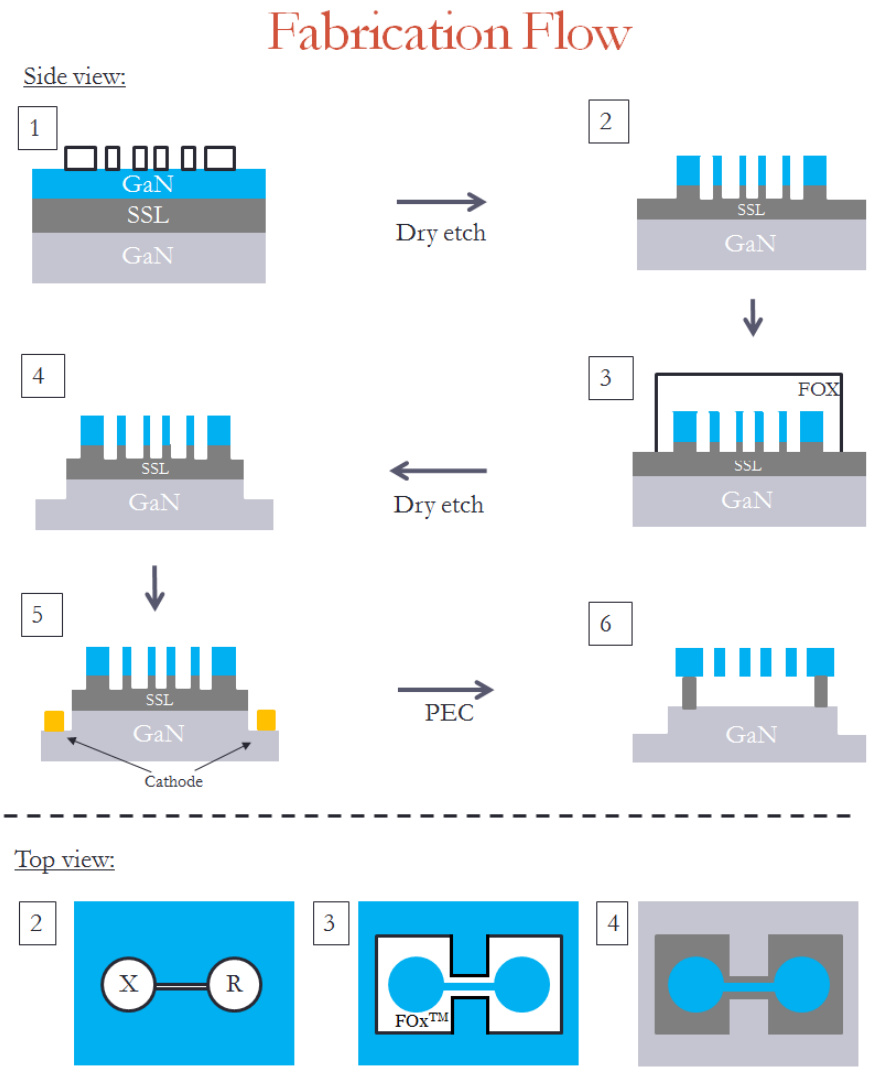

Figure 3.2 Fabrication process flow for the GaN/InGaN photonic crystal nanobeam cavity.

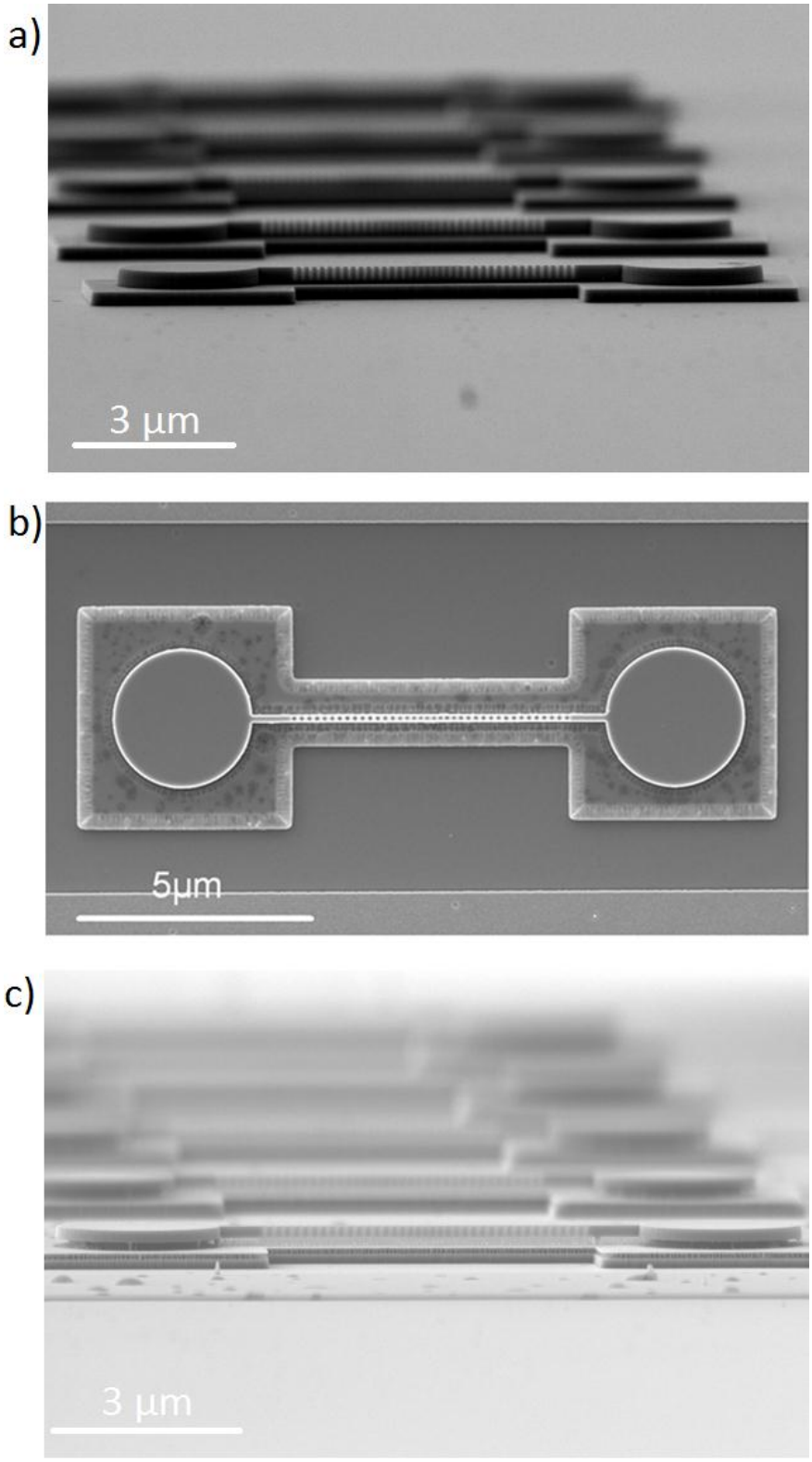

Figure 3.3 (a) SEM of the GaN/InGaN photonic crystal nanobeam before PEC undercut showing the complete dry-etch transferred mesa. (b) SEM top-view image of the photonic crystal nanobeam. (c) SEM side-view image of the photonic crystal nanobeam.

3.2.2 Photoluminescence Characterization

Optical characterization of the PC nanobeams is performed using a frequency-doubled pulsed titanium-sapphire laser at 380 nm wavelength focused onto the sample through a long working distance objective (×40, NA=0.5). The schematic of the optical set-up is shown in Appendix A. The laser spot is a uniform Gaussian shaped beam with 290 nm radius.

Samples with 200 nm thick cavity membrane and 3 layers of active media, as shown in Figure 1.20, are used to fabricate the PC nanobeams discussed in this chapter. A longer wavelength resonance is necessary for QD-embedded nanobeams which are tuned in water and gas chamber for deterministically achieving QD-cavity mode coupling. As a result, design 1 in section 3.1.1 is adopted for QD nanobeams. All nanobeams with fQW and QW gain media are fabricated according to design 2 outlined in section 3.1.1 primarily for lasing experiments. The Q factors of the QD devices are as high as ~ 4200 due to improved fabrication with adjusted parameters obtained by examining the processed devices in SEM, whereas initially fabricated devices with fQWs and QWs have Q factors ranging from 1300 to 2500. Further improvement on the Q factors for fQW and QWs devices can be achieved by optimizing the fabrication parameters similarly as done for the QD devices. The principal modes of the fQW and QW nanobeams are measured between 452 nm - 458

nm, a deviation of over 30 nm from the designed resonance at 420 nm. Nanobeams with QDs are designed with a 437 nm resonance, however, principal modes are measured between 468 nm - 475 nm. This observation is due to the reduced sizes of the etched holes of the fabricated devices compared to their designed values, resulting in an enlargement of the cavity region and therefore a red-shift in mode positions. PC nanobeams exhibit much stronger signal-to-noise ratio in their emission spectra compared to microdisks from the same materials. Figure 3.4 shows the room temperature PL spectra of the fQW, QW, and QD nanobeams.

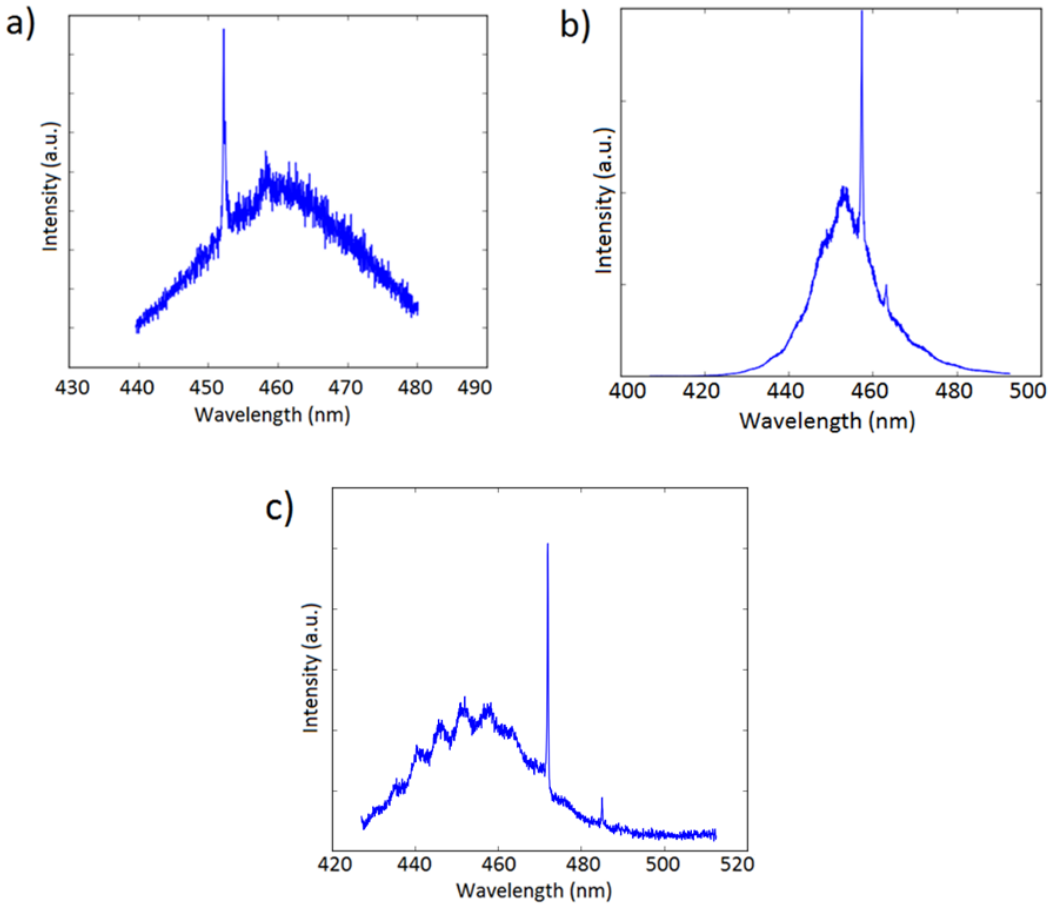

Figure 3.4 Room temperature PL spectra of 200 nm thick PC nanobeams with (a) fQW, (b) QW, and (c) QD active media.

Immediate lasing was observed from GaN nanobeams with 3 layers of InGaN QWs and fQWs. The next section 3.2.3 thoroughly examines lasing from nanobeams with these gain materials. It is important to note that no lasing was observed from nanobeams with QDs, likely due to the reduced capture cross-section of the QDs and the cavity principal modes being close to the center of the background luminescence. As observed from the GaN/InGaN microdisk system, fQW and QW microdisk cavities lased within the spectral vicinity of the peak of the background luminescence. However, microdisks with InGaN QDs achieved lasing only with the WGMs of the shortest wavelengths, on average at ~ 428 nm. As a result, blue-shifting the principal mode may be necessary to achieve QD lasing in these GaN/InGaN nanobeams.

3.2.3 Nanobeam Lasing

The first application of the GaN/InGaN PC nanobeams is ultra-low threshold lasing. Lasing with a spontaneous emission factor, β, as high as 0.94, and a threshold as low as low as 50.1 μW of incident power or 9.1 $\mu J/cm^2$ of absorbed power, is successfully demonstrated. The active medium of these ultra-low threshold structures consists of three fQW layers: InGaN layers consisting of strips 50 nm to 100 nm wide, isolated by narrower troughs, filled

with GaN. For comparison, GaN nanobeams with uniform InGaN QWs are fabricated which demonstrate an average adjusted threshold of ~ 203.6 $\mu J/cm^2$, more than an order of magnitude higher than the average threshold of the fQW nanobeam lasers. Such observation is interestingly contradictory to the measured lasing properties of microdisk lasers with these gain materials. Because of the high surface area to volume ratio of the nanobeam cavities, the additional carrier confinement in the InGaN fQW active medium is essential in reducing non-radiative recombination with the sidewalls and surfaces of the nanobeam cavity, resulting in a dramatically improved lasing threshold. As an active medium with greater carrier confinement than quantum wells, and higher carrier capture probability than quantum dots, InGaN fQW has the potential to be the ideal gain material for a GaN nano-cavity laser. Further analysis on this point is addressed later in this dissertation.

Lasing behavior in the nanobeam devices is clearly demonstrated through linewidth narrowing due to increased temporal coherence (0.32 nm under low excitation power to 0.1 nm at the onset of lasing) [49, 65], and the dramatic increase of the PL emission intensity as a function of incident pump power. The inset image of Figure 3.5 (a) compares the discernible narrowing in linewidth of the principal mode when excited below and above threshold. Moreover, with increased excitation power, there is a slight blue-shift of the

spectral position of the principal mode, which may be related to screening of the built-in electric field. Three different spectra are shown in Figure 3.5 (a), taken below threshold, at threshold, and above threshold. The broad background at low pump power is the signature emission of the fQW active medium, coupled to the leaky modes of the cavity. Figure 3.5 (b) provides a log-log plot of the output intensity versus input power for the device with the lowest threshold, demonstrating all three regimes of operation: spontaneous emission, amplified spontaneous emission, and stimulated emission with laser oscillation. Fits of these data to the laser rate equations suggest a spontaneous emission factor, β, as high as, 0.94. The high β results from the small modal volume, the high quality factor of the mode and the overlap of that single mode with the gain medium. The result is an efficient channeling of the emitted light into essentially a single mode. In comparison, a GaN/InGaN microdisk laser has multiple distinct WGMs overlapping with the principal emission of the active medium. As a result, the competition between these modes significantly reduces the β factor of a microdisk cavity laser compared to a nanobeam laser fabricated from the same material.

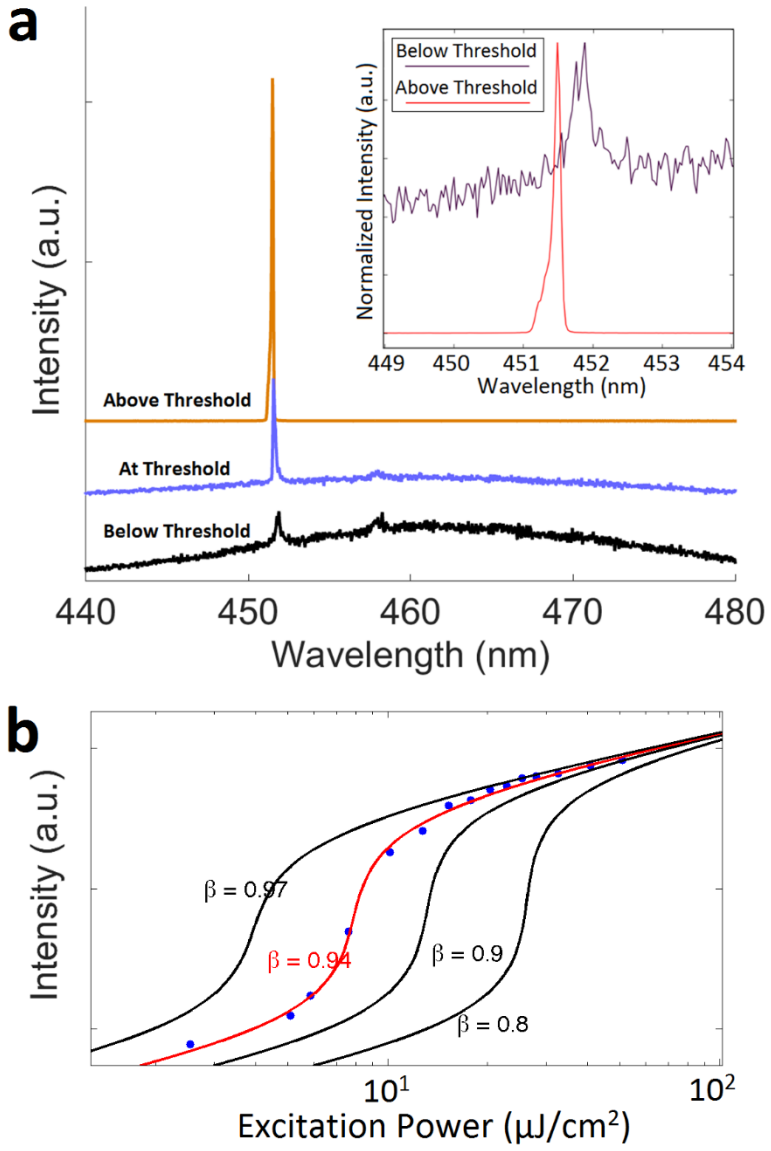

Figure 3.5 (a) Spectra of the nanobeam at three pump regimes: below threshold, at threshold, and above threshold. The inset graph shows a discernible narrowing in the linewidth of the principal mode when excited below and above threshold. (b) Log-log plot of the emission intensity vs. pump power clearly indicating three regions of lasing operation.

Since the excitation laser spot used to couple energy into the nanobeam is far larger in area than the cavities, and since the cavities are fully suspended, the

actual power absorbed by the nanobeams is far less than the incident power applied onto the nanobeams. Therefore an estimate of the actual power absorbed is carried out in the following way: the amount of excitation laser power absorbed by the cavity can be approximated by $P_{abs} = \eta P_{in} \cdot A_{\text{int}}$, whereas P_{in} is input power measured directly above the sample, P_{abs} is absorbed power by the cavity, η is an effective material absorption factor, and A_{int} is the portion of the laser beam intercepted by the cavity. Nearly at the diffraction limit, the excitation laser beam spot with wavelength of 380 nm is approximately 290 nm in radius. It is realistically assumed that the nanobeam is positioned in the center of the uniform laser beam and intercepts approximately 24.5% of the area of the laser beam. In addition, a portion of the incident beam is reflected at each interface between the nanobeam and air. Using a simple approximation, η can be computed by $\frac{(1-R)\cdot(1-e^{-\alpha d})}{(1-\mathrm{R}e^{-\alpha d})}$, whereas, R = 0.18, is the reflection coefficient at each air-beam interface, due to the difference in effective index between air and GaN, α is an effective absorption coefficient for the 380 nm light in traversing a distance *d*, within the beam. The incident beam should be selectively absorbed by the InGaN component of the material, for which a value of $\alpha = 5 \times 10^4\ \text{cm}^{-1}$ is used according to Reference 58. The thickness of the 3 InGaN fQW layers is assumed to be 7.5 nm as deliberately grown. Because of uncertainties in the actual thickness of the InGaN QWs and fQWs upon growing the capping GaN layer, and because there may be absorption levels in the GaN itself, it is also

possible to extend a conservative estimate of d to be 20 nm, or 10% of the physical thickness of the nanobeam. Following this conservative estimate, η is then computed to be approximately 9.3%, and therefore the absorbed power, P_{abs}, is estimated to be about 2.3% of the measured input power, P_{in}. Thus, the lowest lasing threshold of P_{in}=50.1 μW corresponds to an absorbed power P_{abs} of approximately 1.15 μW, over an illuminated area of 125 nm × 580 nm deducted by the area of the two middle holes with radius approximately 35 nm. Given the duty cycle of the pump beam, this corresponds to

$$\frac{1.15\mu W}{76\,MHz}\cdot\frac{1}{(125\times10^{-7})\times(580\times10^{-7})-2\times\pi\times(35\times10^{-7})^2}=23.4\mu J/cm^2$$

The greatest uncertainty lies in the absorption depth, assuming d is as-grown 7.5 nm and 20 nm as conservatively estimated, P_{abs} could vary from approximately 0.9% to 2.3 % of P_{in}, which corresponds to a threshold energy density of 9.1 μJ/cm² to 23.4 μJ/cm², respectively, for the cavity with best optical performance. For all adjusted thresholds presented in this section, absorption depth d of 7.5 nm and a 0.9% absorption coefficient is used for computation.

Figure 3.6 shows a table summarizing the lasing wavelength, Q-factor, and the adjusted lasing threshold of the five measured nanobeam cavities. The adjusted lasing thresholds range from 9.1 μJ/cm^2 to 27.2 μJ/cm^2 with

relatively consistent lasing wavelengths around 454 nm. During the experiment the power is measured in Watts. No clear connections between the lasing thresholds and below-threshold Q factors are observed.

PCC #	Lasing wavelength (nm)	Q-factor (below threshold)	Adjusted threshold (μJ/cm²)
1	456	1333	27.2
2	453	1905	9.3
3	454	1354	12.6
4	452	1451	9.1
5	452	1605	19.8

Figure 3.6 Table summarizing the lasing wavelength, Q-factor, and the adjusted lasing threshold of the five measured nanobeam cavities.

Nanobeam structures identical to those previously described, but which incorporated three layers of uniform quantum well material of approximately the same composition showed a far poorer percentage of lasing devices. While all of the 11 fQW nanobeam lasers probed demonstrated lasing, only 3 out of 10 of the uniform QW nanobeam devices, with minimum measured Q of ~ 1000, showed clear lasing behavior using excitation power allowed by our optical set-up, likely due to variations in the material and gain medium qualities across the sample wafer. For 5 fQW nanobeams that were analyzed in detail, the average lasing threshold is calculated to be 15.6 μJ/cm², and the lasing wavelengths are relatively consistent at around 454 nm. Comparatively,

the average adjusted threshold for the QW nanobeam lasers is 203.6 μJ/cm², more than an order of magnitude higher than the average threshold of the fQW nanobeam lasers. Figure 3.7 shows the linear output intensity vs. pump power plots for a fQW and a QW nanobeam laser, demonstrating clear lasing behaviors with a dramatic difference in thresholds. These results are particularly interesting since our earlier comparison of lasing thresholds in microdisk cavities discussed in the last chapter yielded the opposite outcome: the average lasing threshold for cavities with fQW active layers was approximately four times greater than for cavities with QW active layers. In addition, the range of threshold powers was about an order of magnitude larger for the fQW microdisk lasers.

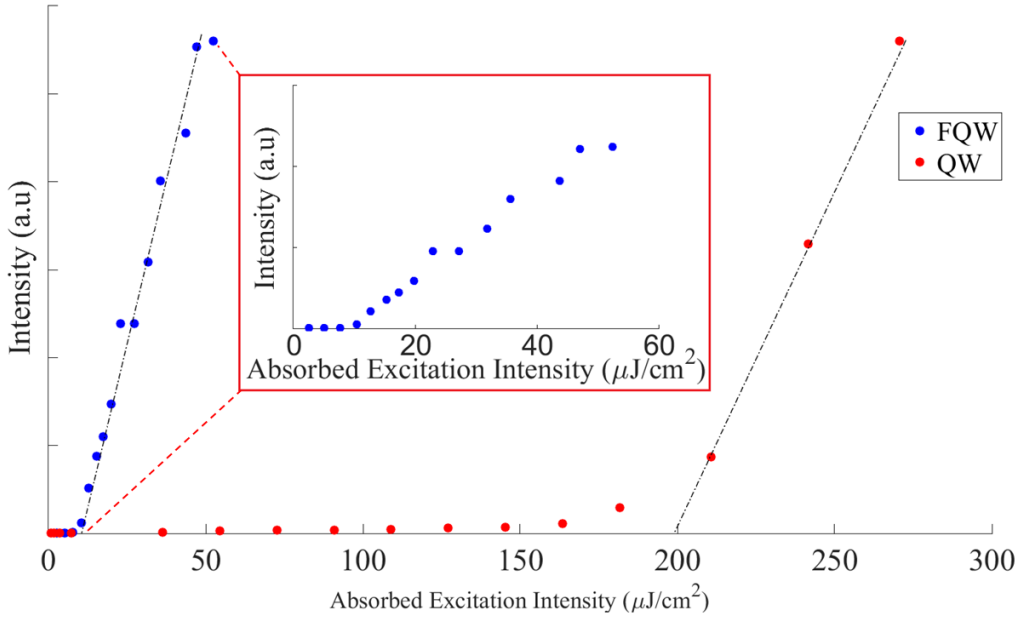

Figure 3.7 Linear output intensity vs. pump power plots comparing the thresholds of the fQW and QW lasers. The inset shows a zoomed-in version of the plot for the fQW laser with 9.1 μJ/cm² threshold. The QW laser has an adjusted threshold of 198.6 μJ/cm².

It is believed that the difference results from the changes in the relative loss mechanisms for carriers and photons as the cavity-active medium system is altered. The nanobeam cavities provide smaller modal volumes than do the microdisks, allowing a stronger mode-emitter coupling. Figure 3.8 shows a AFM of the fQW layer before capping and the inset shows a portion of the nanobeam cavity dimensions overlaid on the as-grown annealed InGaN epilayer, illustrating the interplay of the scales of the two structures.

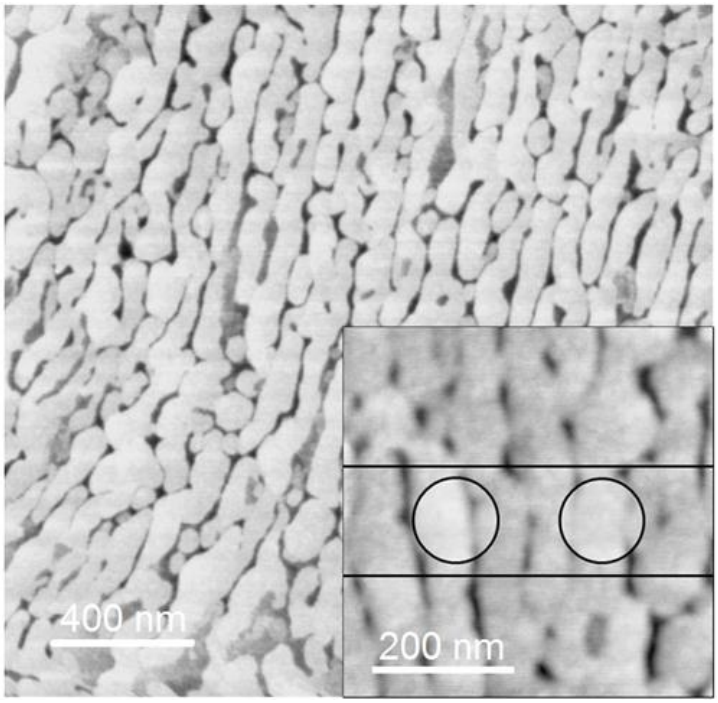

Figure 3.8 AFM scan of the annealed InGaN epilayer showing the fQWs before capping. The inset image presents a possible overlay of the nanobeam and the fQW structures at the same size scale, showing the interplay of the two.

The schematic shown in Figure 3.9 (a) suggests how electron-hole pairs created within a uniform QW active layer of the nanobeam cavity may diffuse

to the edges of the etched holes and recombine non-radiatively with surface states. The region enclosed by the dashed line delineates the approximate boundaries of the center cavity mode. If the average distance of photo-created carrier to etched surface is less than a carrier diffusion length (LD), then a substantial loss to non-radiative recombination is expected. Although no measurement on the diffusion lengths and radiative lifetimes of these particular samples is performed, there are readily available guidance and information from the literature in order to make an order-of-magnitude estimate of $LD = [Dt]^{1/2}$, where D is the diffusion constant, and t is the carrier lifetime for the InGaN active material. Danhof et al (2011) carried out time-of-flight measurements of carrier diffusion in InGaN/GaN quantum wells [98]. They deduced an ambipolar diffusion constant at room temperature of 1.2 cm^2/s for InGaN quantum wells emitting at 470 nm. Values of t will also vary, depending on the nature and quality of the active layer material, but an order of magnitude estimate of $t \sim 10$ ns can be used [99]. The resulting estimate for LD is ~ 1.1 μm, while the typical distance between holes in the nanobeam is ~ 130 nm. Thus, a substantial proportion of the photo-generated carriers will diffuse to the edges or surfaces of the nanobeam and undergo non-radiative recombination with surface states. The large reduction in carrier-generated photons leads to significantly increased lasing thresholds for nanobeams with uniform QW active layers. By contrast, the modulated potential barriers of the fQW active layers enhance the localization of the carriers and limit diffusion to

the surfaces as illustrated by Figure 3.9 (b).

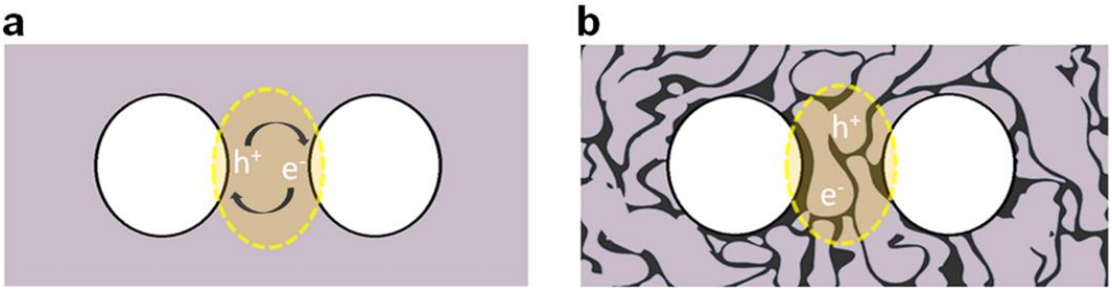

Figure 3.9 (a) Schematic of a nanobeam cavity with uniform InGaN QW active medium. Photo-generated electron-hole pairs can diffuse to the edges of the etched holes and recombine non-radiatively with surface states as indicated by the arrows. (b) Schematic of a nanobeam cavity with InGaN fQW active medium. Photo-generated electron-hole pairs are localized within the boundaries of the isolated islands of the fQW. The regions enclosed by the dashed line in (a) and (b) represent the boundary of the center cavity mode.

In contrast, the best coupling between microdisk cavity and active layer for the multiple maxima distributed along the periphery of the microdisk is achieved for a gain medium that is as uniform as possible. Carriers generated through the entire interior of the disk may diffuse to the periphery, recombine radiatively and interact with the whispering gallery modes. The larger lateral dimensions of the microdisk cavity (with radius > LD) allows the collection of photons from a larger fraction of the photo-generated carriers [100]. The spatial variability of the fQW material disrupts that uniformity, leading to a larger variability and often larger value of the lasing threshold. Thus, the uniform QW active layers produce lower threshold lasing than fQW active

layers for microdisk cavities. By and large, these observation and analysis suggest that matching nanocavity geometry to the right nanostructured gain medium is critically important for fabricating GaN/InGaN lasers with excellent performance.

3.3 GaN/InGaN Nanobeam with QDs

3.3.1 Purcell Effect and Strong Coupling

In cavity QED, one of the most intriguing fundamental effects is the modification of the spontaneous emission (SE) rate of a quantum emitter [101]. SE rate was believed to be an intrinsic property of the emitter. Edward Purcell (1946) presented a theoretical finding suggesting an optical environment with an enhanced local optical density of states, for example a cavity, can control the rate of radiative recombination of an embedded emitter [102]. Such an effect is useful for many applications such as nano-optical spectroscopy [103–106], microlasers [107], and single-photon devices [108, 109]. Figure 3.10 shows the comparison between the optical density of states in a cavity and in free space. In a spontaneous emission event in free space, the emitter is coupled to the vacuum fluctuation energy which triggers the radiative transition [66]. However, in a cavity the optical density of states is

spectrally and spatially enhanced by the resonant mode and dramatically suppressed elsewhere [101, 102]. As a result, an emitter spatially and spectrally matched to a cavity resonant mode will experience an accelerated SE rate whereas an emitter with detuned resonance from the cavity resonance will experience a radiative quenching in its SE efficiency.

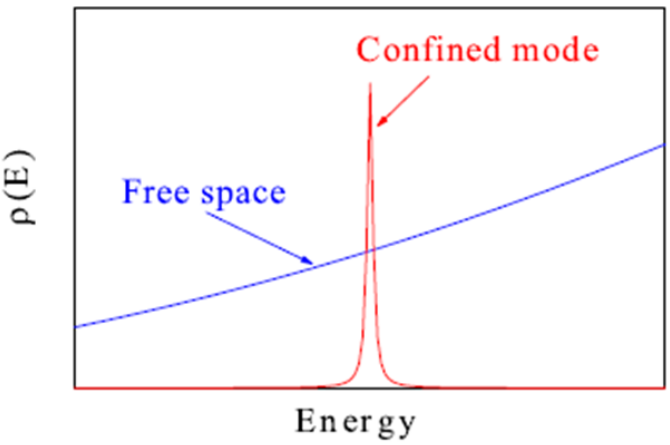

Figure 3.10 Comparison of local optical densities of states in a cavity and in free space.

The maximum SE rate enhancement, namely the Purcell factor F, is defined as [102],

$$F = \frac{3}{4\pi^2}\left(\frac{\lambda}{n}\right)^3 \frac{Q}{V}$$

λ/n is the resonant mode wavelength in the material in which the emitter is located. The Purcell factor F given by this equation is derived by assuming a perfect spectral, spatial and polarization matching between the emitter and

the cavity mode. In reality, deviation from these assumptions will lead to a reduction in the observed SE enhancement and Purcell factor. [101]

Moreover, a strongly coupled cavity-emitter system is created when the spontaneous emission rate of the emitter is increased beyond any underlying dissipative rates, such as the cavity loss and emitter dephasing rates, and the cavity field-emitter interaction time [110-112]. Under the conditions of strong coupling, the original cavity resonance is split into two spectral peaks, which are new eigenfunctions representing entangled states of the emitter and cavity field. Such a system can be critically important for creating practical optical qubits and polariton lasers [112, 113].

3.3.2 InGaN QDs in Nanopillar

A unique advantage of the QD is its ability to emit single photons. As a result, cavities with QDs are often used for studying light-matter interaction at the single photon level. InGaN QDs offers many great advantages compared to QDs from other material systems, such as having a large exciton binding energy which can significantly increase the operational temperature for certain experiments. Before proceeding with cavity QED experiments, GaN nanopillars are fabricated to spatially isolate single InGaN QDs to gain

insights about their optical properties.

Through numerous low temperature PL measurements of different samples of InGaN QDs, it is found that QDs embedded in p-i-n doped GaN matrix give consistently distinct exciton transitions with moderate background. Figure 3.11 shows the material system for fabricating the GaN/InGaN nanopillars. The InGaN QD layer is located 200 nm below the top surface of the GaN. Fabricating this material into nanopillar structures provides better collimation and directionality for the emitted photon, and thereby delivers a stronger signal to the detector.

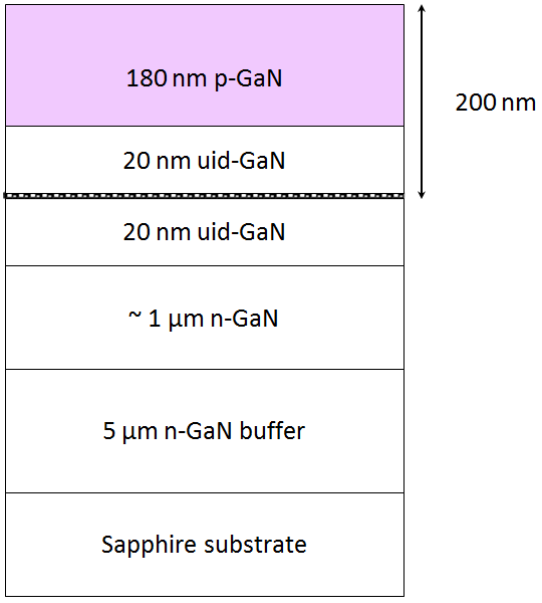

Figure 3.11 Material structure for the GaN/InGaN nanopillars with QDs.

The nanopillars are masked with FOx-16 resist and patterned using Elionix E-beam lithography. The sample is subsequently dry-etched in Unaxis ICP RIE

to a depth of ~ 900 nm. Figure 3.12 shows SEM images of the nanopillar with 100 nm diameter measured on the top surface. The tapered shape naturally results from dry-etching using Cl_2 and Ar gases and radiates a stronger signal for optical detection because a gradual narrowing of the nanopillar tip decreases its effective refractive index therefore reducing light reflection at the top interface with air. The QD density is ~ $10^{10}/cm^2$. As a result, on average there are ~ 2 QDs embedded in a single nanopillar. Moreover, it is known that surface effects can adversely affect emission efficiency of QDs in GaAs and other III-V semiconductors [114, 115]. However, InGaN QDs are smaller and offer stronger confinement for the carriers due to larger effective masses [116]. Therefore, their emission property is more robust and less prone to degradation by surfaces and defects.

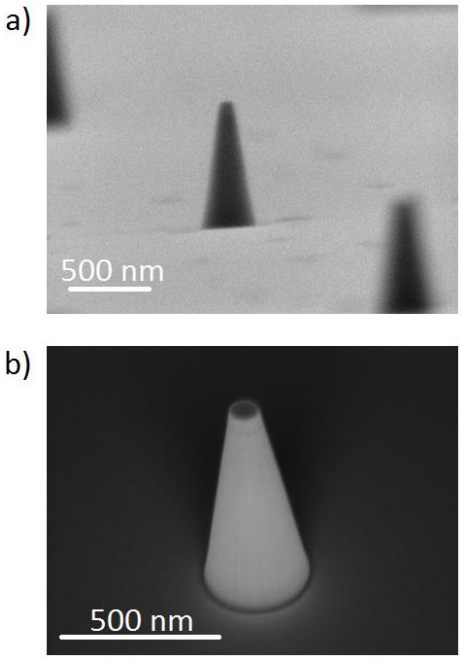

Figure 3.12 (a) Side-view SEM image of the nanopillar. (b) Slanted top-view SEM image of the nanopillar.

Figure 3.13 shows a FDTD simulation for the radiation pattern of the fabricated nanopillar. The QD is vertically located close to the upper mode maximum illustrated in Figure 3.13 (a). This enables the QD to efficiently couple to the waveguide mode of the nanopillar to radiate favorably upward in a collimated manner. Figure 3.13 (b) shows a top view of the radiation pattern demonstrating the directionality of the emission profile.

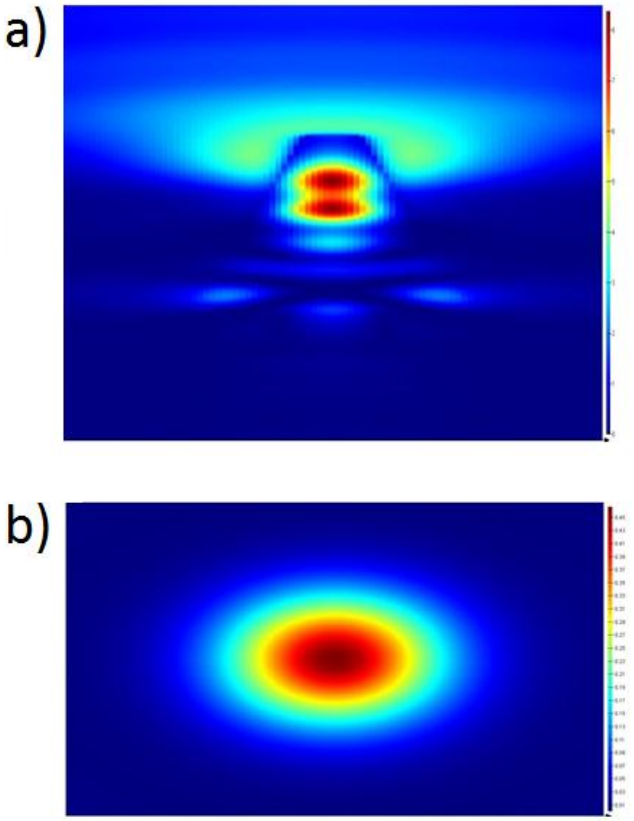

Figure 3.13 (a) Side-view FDTD simulation of nanopillar radiation profile. (b) Top-view FDTD simulation of nanopillar radiation profile.

Optical characterization of the PC nanobeams is performed using a frequency-doubled pulsed titanium-sapphire laser at 380 nm wavelength focused through a long working distance objective (×40, NA=0.5). The schematic of

the optical set-up is shown in Appendix A. The laser spot is a uniform Gaussian shaped beam with 290 nm radius. The sample is center-positioned in a cryostat compatible with liquid Helium cooling. Figure 3.14 (a) and (b) respectively show the PL spectra of the bulk material and a nanopillar measured at ~ 4K.

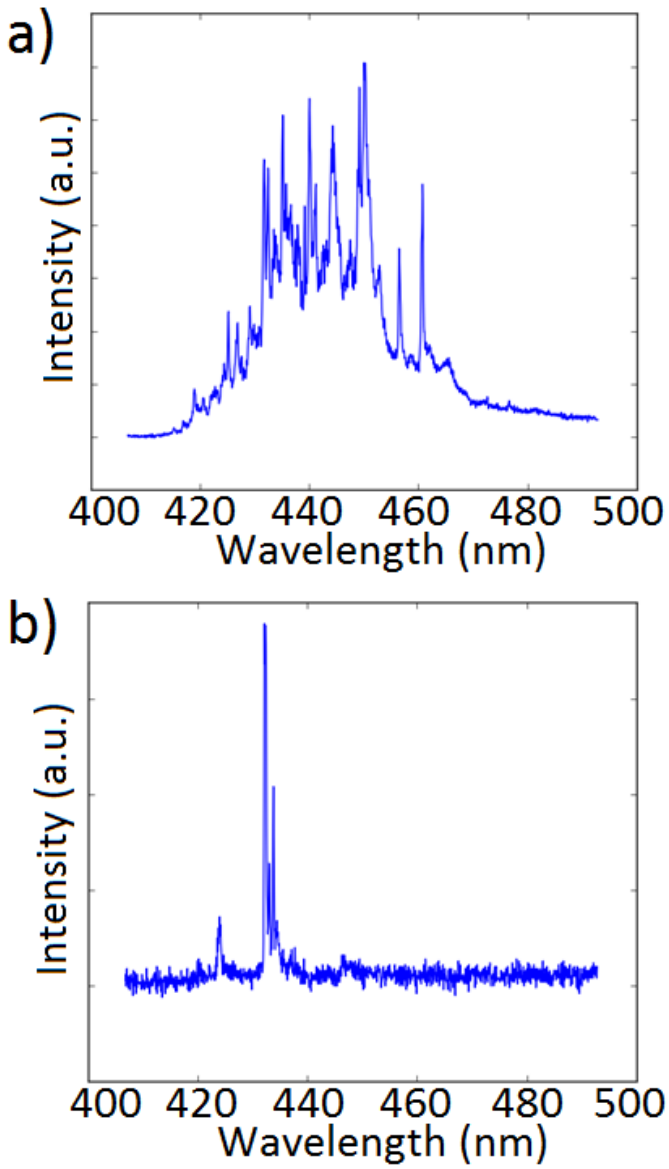

Figure 3.14 (a) PL spectrum of the bulk material. (b) PL spectrum of a nanopillar. Both spectra are measured at ~ 4K.

It is important to note due to the modified droplet epitaxy technique, fQWs formed during the annealing process are inevitably grown in the vicinity of the QDs [22, 23]. The active media collectively generate a luminescence ranging from 420 nm to 500 nm. As Figure 3.14 (b) shows, distinct peaks with minimal background emission are observed likely pertaining to individual exciton and bi-exciton transitions. Comparing spectra in Figure 3.14 (a) and (b), it is clear that the nanopillar structure is effective in isolating individual QDs without deteriorating their optical signatures. For the majority of nanopillars, relatively broad luminescence, often positioned between ~ 460 nm and ~ 500 nm, is commonly observed and believed to originate from the fQWs. The InGaN QDs are physically smaller, which results in blue-shifts of their emissions to a shorter wavelength range. A spread of lifetimes for the QDs are measured ranging from ~ 1 ns to ~ 10 ns. The variation of exciton lifetimes is due to the combination of quantum confined Stark effect and inhomogeneity in the sizes of the QDs [117, 118].

In a QD, a pair of biexcitons is created by tightly confining two excitons in a single energy level. Figure 3.15 (a) and (b) show two simplified quantum well diagrams illustrating energy levels occupied by an exciton and a biexciton pair, respectively. Due to the need for absorbing two photons in order to create two excitons, the intensity of the biexciton signature has a quadratic dependence on the excitation power. Moreover, the built-in electric field of

GaN/InGaN weakens the overlap of the electron and hole wave functions and push carriers of the same type towards opposite boundaries of the QD. As a result, repulsive interactions among the carriers commonly dominate over the attractive ones, rendering the biexciton binding energy negative. In the PL spectrum, the biexciton transition therefore appears at the higher energy side of the exciton transition [119]. Due to the large variation in composition and sizes of the InGaN QDs, the bi-exciton binding energies can vary significantly. A biexciton signature is clearly recognized through power-dependent measurement of a nanopillar as shown in Figure 3.15 (c). The exciton transition obeys an expected linear dependence with excitation power while the biexciton transition varies with excitation power to the ~ 1.86^{th} power. It is interesting to note as shown in Figure 3.15 (d) that under high excitation powers, over ~ 100 μW in most cases, the exciton intensity plateaus because higher excitation power only lead to higher generation rate of biexcitons in the QD. For the power dependent measurement on the biexciton transition, the deviation from perfect quadratic dependence may be due to capture of incident photons by defects and imperfections, loss of carriers at higher excitations, and minimal drift of the measurement stage. The general broadening of the exciton and bi-exciton transitions are likely due to spectral diffusion [120].

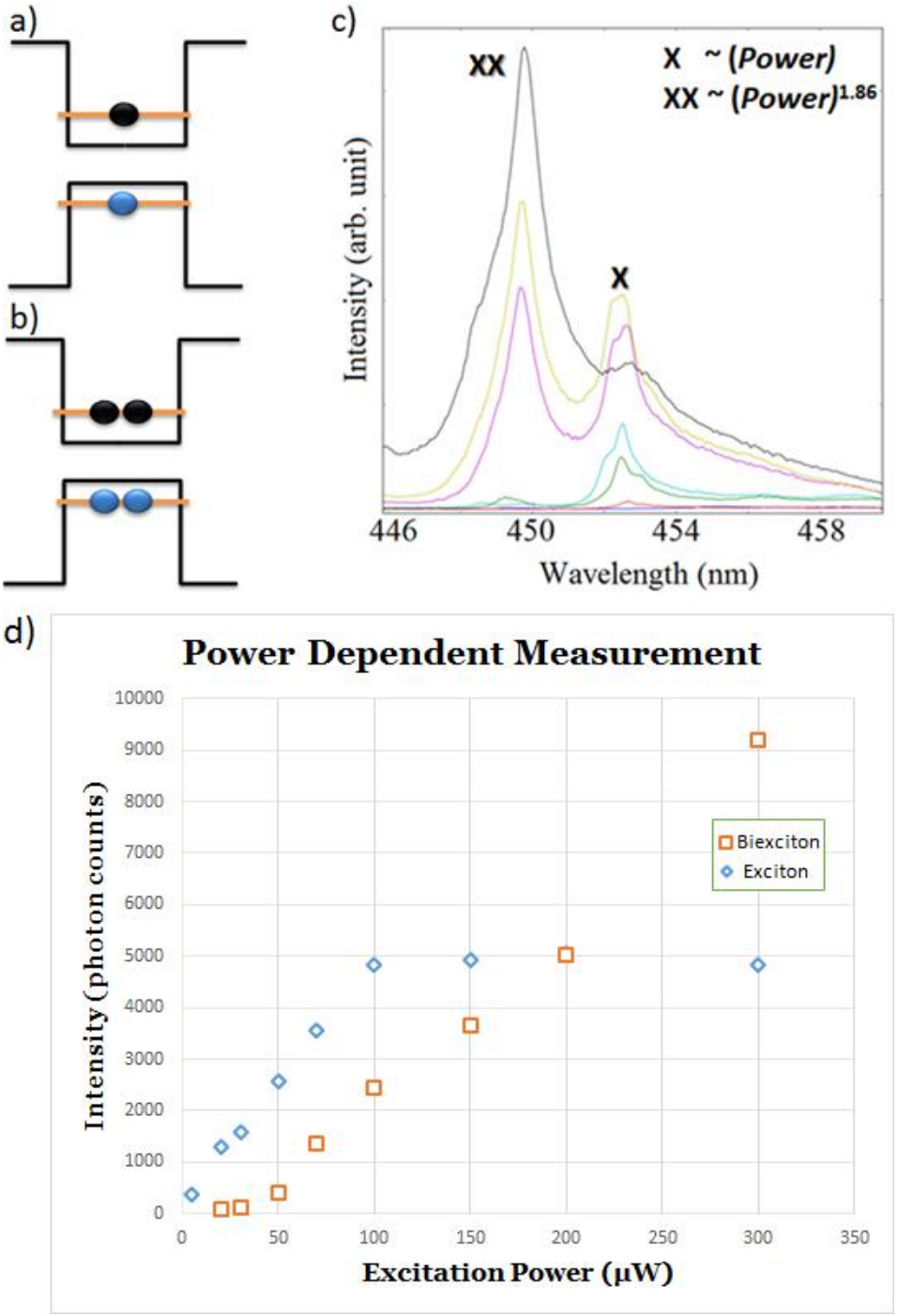

Figure 3.15 (a) An exciton in a QD (b) A pair of biexcitons in a QD. The black and blue dots represent electrons and holes, respectively. (c) Exciton and bi-exciton emission signatures from power-dependent measurement of a nanopillar at ~ 4K. (d) Intensity vs. excitation power plot of the exciton and biexciton emissions.

Figure 3.16 (a) shows the PL spectrum of a nanopillar at ~ 4K. Due to the absence of the broad luminescence, the QD is likely the only active medium present in the structure. Upon laser excitation, an exciton peak at 450 nm is distinctly observed with minimal spectral drift or diffusion. A tunable optical band-pass filter is then used to allow only the isolated exciton transition to pass through. The spectral window of the band-pass filter is depicted as enclosed by the red dotted lines in Figure 3.16 (a). The filtered signal, as shown in Figure 3.16 (b), is then directed to a detection system to perform anti-bunching measurement.

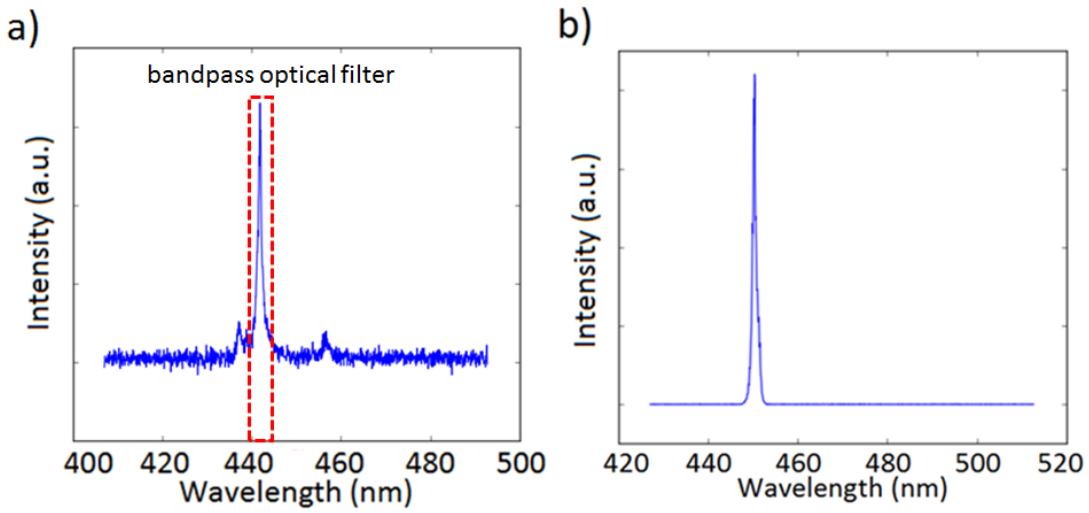

Figure 3.16 (a) PL spectrum of the nanopillar. The area enclosed by the red dotted lines represent the spectral window allowed by the optical band-pass filter. (b) PL spectrum of the nanopillar after band-pass filter is applied.

The simplified anti-bunching measurement set-up is shown in Figure 3.17 (a). This method gives the intensity autocorrelation function by generating the

correlation between detected signals from two independent detectors as shown in Figure 3.17 (a). In this experiment, incident photons from the optically filtered nanopillar impinge onto a 50:50 beamsplitter. An electronic correlator then records the time interval between a detection event at one detector that triggers "start", and a subsequent detection at the other detector that triggers "stop". A histogram of coincidences as a function of the interval between photon detections, τ, is constructed. A delay is placed in the stop channel in order to record negative inter-photon times. Autocorrelation function, $g_2(\tau)$, which represents the statistical character of coincidence intensity, is computed as,

$$g_2(\tau) = \frac{\langle I(t)I(t+\tau)\rangle}{\langle I(t)\rangle^2}$$

I(t) is the intensity of the detected signal. For an intrinsic single-photon emission event, $g_2(0) = 0$, representing that no two photon can arrive at the two independent detectors simultaneously. For a realistically viable semiconductor single photon source, $g_2(0) < 0.5$ is necessary to confirm that such a device is statistically more probable to generate single photon emission over multi-photon emission events. Figure 3.17 (b) shows the measured autocorrelation function of the nanopillar with a computed $g_2(0)$ of ~ 0.231. This unambiguously demonstrates the successful observation of single photon emissions from an InGaN QD embedded in a GaN nanopillar.

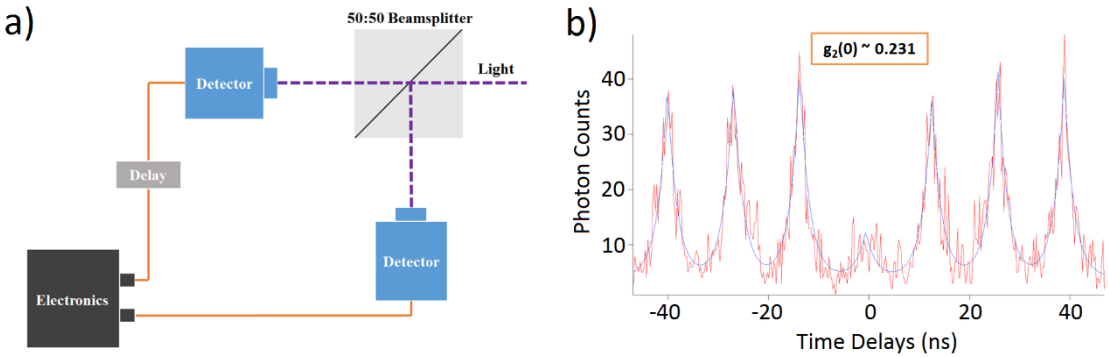

Figure 3.17 (a) Optical set-up for anti-bunching measurement. (b) Measured autocorrelation function of the nanopillar, $g_2(0)$ is ~ 0.231.

3.3.3 Tuning Nanobeam Cavity

The promise of InGaN QD as a single photon emitter is demonstrated in the previous section 3.3.2. As discussed in section 3.3.1, spectrally and spatially coupling the principal cavity mode of a GaN nanobeam to a single exciton transition of an embedded InGaN QD leads to spontaneous lifetime reduction for the emitter through Purcell factor enhancement. A net result of this achievement is a rate and collection enhanced blue single photon source. Moreover, a strongly coupled cavity-QD system is created when a QD exciton transition rate is significantly enhanced past any dissipative event [110, 111]. Such a system can be essential for optical quantum computation and single atom polariton lasing [113, 121]. First and foremost, a method to spectrally and spatially match the cavity mode to a QD exciton is required.

For cavity-QD coupling experiment, a PC nanobeam is a more effective cavity structure compared to a microdisk. Besides the advantage of having a high Q-factor and a wavelength-scale modal volume, most importantly the physical cavity region of a nanobeam is small and closely matched to its mode profile, as clearly shown by the FDTD simulation in Figure 3.1 (c). As a result, it is much more probable for a QD that is distinctly observed in the PL spectrum to be on spatial resonance with the cavity mode. Thus, p-i-n doped GaN/InGaN PC nanobeams with 3 layers of QDs (material structure shown in Figure 1.23) are fabricated according to design 1 outlined in section 3.1.1 for this experiment.

Figure 3.18 (a) shows the room temperature PL spectrum of a nanobeam with a principal mode at 473 nm and a Q-factor of ~ 2300. Since the principal cavity mode is close to the long wavelength tail of the broad QD luminescence, it is therefore necessary to irreversibly blue-shift the mode to a wavelength shorter than the QD luminescence peak in order to apply a gas absorption technique as a next step to further red-shift the mode into resonance with a desirable QD exciton in situ at low temperature. As a first step, the developed water tuning technique used on microdisk system is applied to the nanobeam using the same set-up. Frequency-doubled pulsed titanium-sapphire laser at 380 nm wavelength is used to irradiate the selected nanobeam immersed in DI-water. Figure 3.18 (b) shows the PL spectrum of the same nanobeam after

6 minutes of laser tuning in DI-water with low incident power of ~ 100 nW measured below the objective. The principal mode is successfully blue-shifted ~ 27 nm to a new wavelength of 444 nm. The Q factor of the nanobeam is mildly degraded from ~ 2100 to ~ 1600, likely due to imperfections created on the nanobeam during the surface etching process caused by the tuning technique. Moreover, the nanobeam mode is found to tune faster than a microdisk mode due to the sensitivity of its resonance to change of geometry.

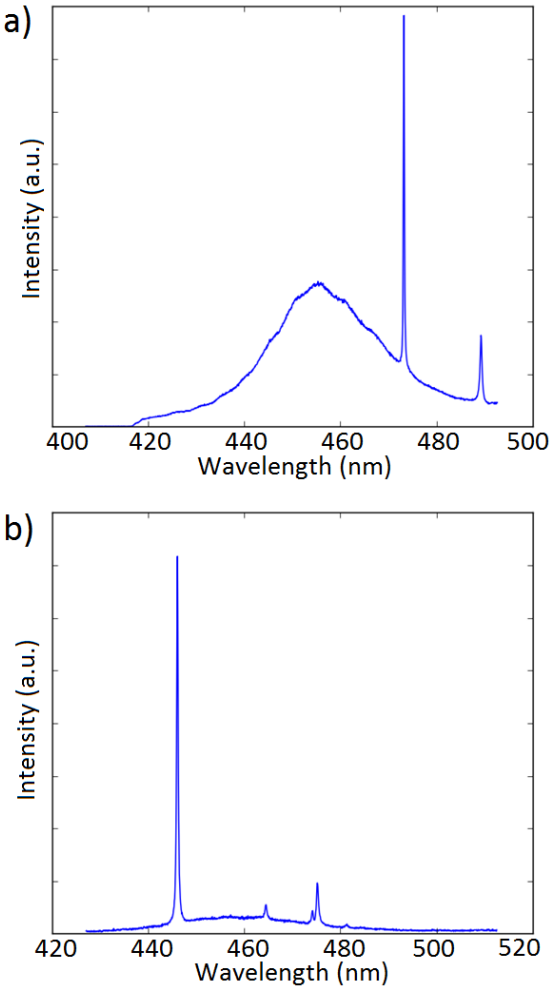

Figure 3.18 (a) Room temperature PL spectrum of the nanobeam. (b) Room temperature PL spectrum of the nanobeam after 6 minutes of laser tuning in DI-water with ~ 100 nW of incident power.

The Purcell factor, assuming perfect spectral, spatial, and polarization match, is calculated to be ~ 91 based on a Q-factor of ~ 1600 and a modal volume of 1.5 $(\lambda/n)^3$. This value also assumes an optimal spatial match between the QD position and the maximum of the mode, one of the most difficult matches to achieve. In order to deterministically tune the system into and out of spectral resonance for lifetime measurements and comparison, a nitrogen gas tuning technique is then employed. Dr. Kasey Russell and Dr. Alex Woolf designed and built the system shown in Figure 3.19. In brief, a digitally controlled amount of nitrogen gas is channeled into a helium-cooled cryostat in which the sample is center-positioned. The gas condenses on the nanobeam that is cooled below the freezing temperature of nitrogen, which effectively enlarges the cavity region leading to an expected red-shift of the cavity resonance.

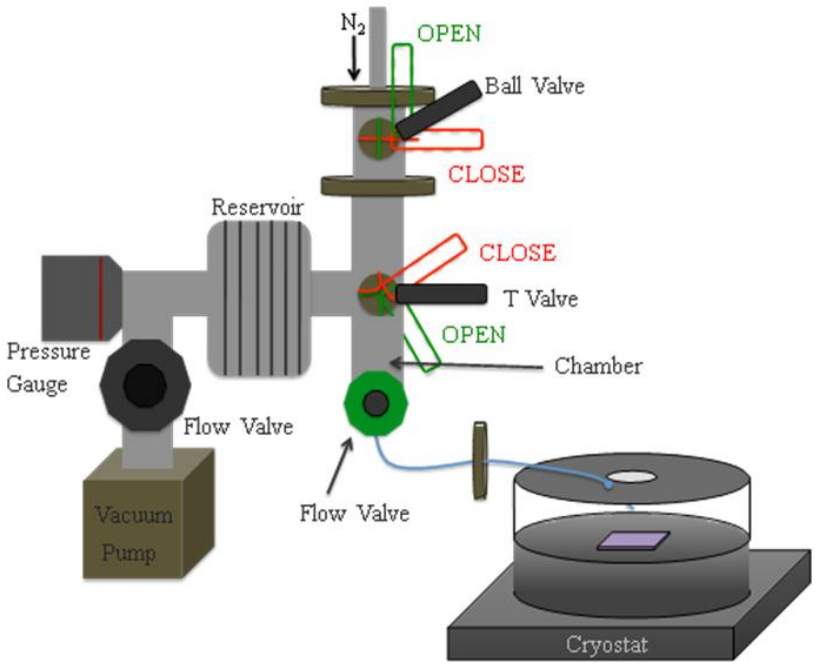

Figure 3.19 Schematic of the gas tuning set-up [49].

In order to proceed with the coupling experiment, a QD exciton transition close to 447 nm is first identified as target. As Figure 3.20 shows, using the gas tuning technique the mode at 444 nm is digitally tuned in multiple steps to reach spectral resonance with targeted exciton transition. The tunable optical band-pass filter is then used to allow the spectrally matched cavity mode-exciton peak into a photon counter for lifetime measurement. The inset of Figure 3.20 shows lifetime traces of the exciton in and out of resonance with the cavity mode, represented by different colors. Unfortunately, no meaningful modification of lifetime is observed, most likely due to the spatial and polarization mismatches between the QD and the high-field region of the nanobeam mode.

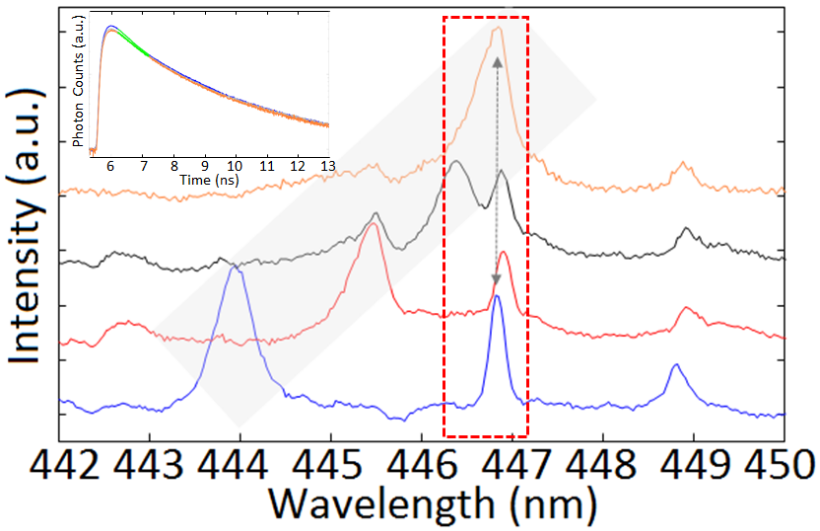

Figure 3.20 PL spectra showing the evolution of the nanobeam cavity mode under digitally controlled gas tuning. The box enclosed by the red dotted line represent the spectral window of the band-pass filter. Inset shows the lifetime plots of the exciton transition measured in and out of resonance with the cavity mode.

The principal modes of the gas-tuned PC nanobeam cavities experience Q-factor degradations after prolonged tunings which are commonly over ~ 6 nm of blue-shifts in wavelengths. This observation may be attributed to the possible uneven condensations of gas molecules onto the cavity surfaces therefore creating physical asymmetries and surface roughness. As a result, the applicability of the gas tuning is limited compared to the water tuning technique. However, for all the measured nanobeam cavities, water tuning is first applied to blue-shift the cavity resonances into the vicinity of target exciton transitions to allow minor subsequent gas tuning to perfectly match the resonances in order to preserve the Q-factors. For a well coupled cavity-QD system, a dramatic increase in intensity of the matched resonances should be observed due to collection enhancement aside from potential spontaneous lifetime reduction. However, among all the measured cavities, no increase in intensity was observed which is likely due to spatial mismatch and polarization mismatch between the emitter and the cavity mode.

3.4 Conclusion and Future Work

In this chapter, basic information on GaN/InGaN photonic crystal nanobeam cavity is introduced and discussed in detail. A new fabrication process is

developed to realize high Q-factor GaN/InGaN nanobeams with QW, fQW, and QDs active media. Surprisingly, fQW is found to have a dramatic influence on the lasing threshold and demonstrates a record low threshold of 9.1 μJ/cm^2, significantly superior to microdisk lasers fabricated from the same material system and comparable to the best devices in other III-V material systems. Due to such ultra-low threshold lasing, it is interesting as a future direction to attempt electrically driven operation on p-i-n GaN nanobeams with InGaN fQWs. Figure 3.21 shows a tentative schematic of an electrically injected GaN photonic crystal nanobeam laser.

Moreover, a single photon signature from an InGaN QD embedded in a GaN nanopillar is demonstrated through an autocorrelation measurement in this chapter. Successful spectral matching of a QD exciton transition to a nanobeam cavity mode is achieved by water and gas tuning techniques. However, no spontaneous lifetime enhancement is observed, likely due to the spatial mismatch between the cavity mode and the QD position. The reliance on the spatial overlap between the QD and cavity mode is probabilistic. Therefore, as another future direction, more GaN/InGaN nanobeams with QDs should be measured and tuned using the development techniques to observe weak coupling.

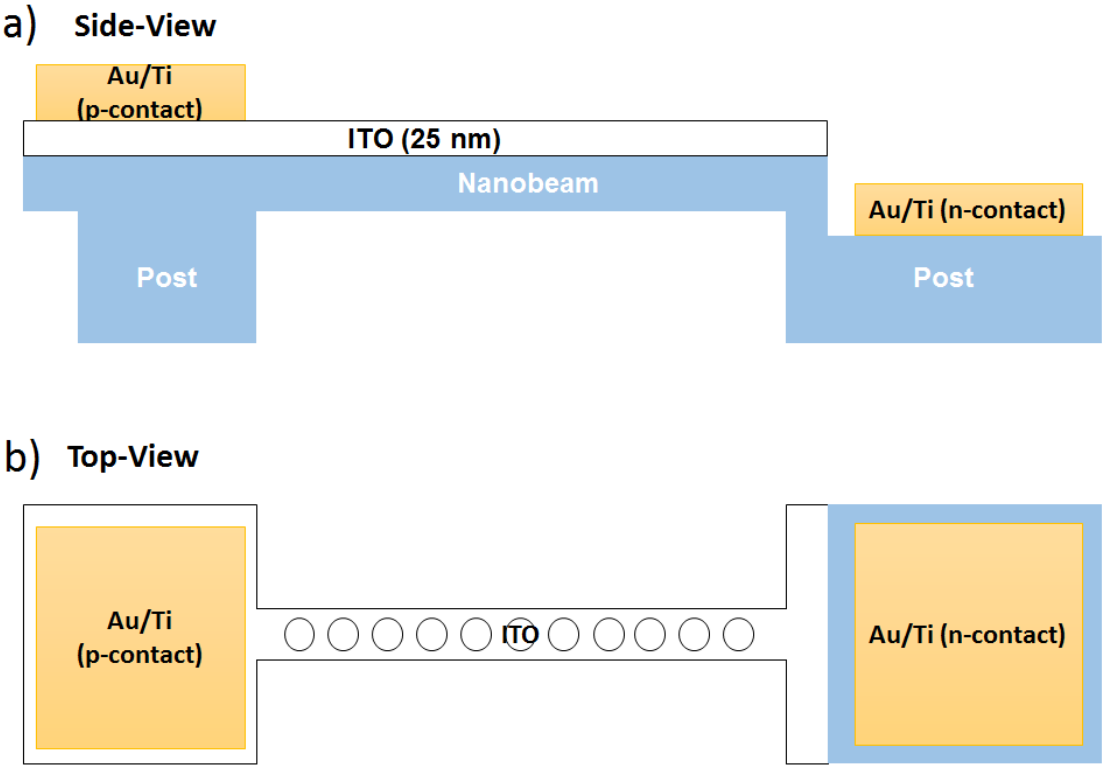

Figure 3.21 (a) Side-view schematic of an electrically injected GaN/InGaN photonic crystal nanobeam laser. (b) Top-view schematic of an electrically injected GaN/InGaN photonic crystal nanobeam laser.

CHAPTER 4: **Conclusion**

In conclusion, GaN/InGaN is an excellent semiconductor material system for fabricating micro- and nano-cavities for experimental studies of optical cavities, lasing dynamics, and cavity QED. Its usefulness and uniqueness are due to its wide direct bandgap, low surface re-combination velocities, and large exciton binding energies, offering the possibility of room temperature realization of light-matter interaction and its applications in the blue spectrum.

In general, it is challenging to fabricate high quality GaN cavities due to its chemical inertness combined with low material quality due to inevitable defects and threading dislocations introduced during growth. However, as outlined in this dissertation, with the novel fabrication processes and the PEC etching developed, high Q-factor GaN microdisk and photonic crystal nanobeam cavities with different classes of InGaN active media, such as QDs fQWs and QW, are successfully fabricated exhibiting distinct modes. The background information on material, growth, and PEC technique is provided

in detail in Chapter 1.

As outlined in Chapter 2, through the use of optimized dry etching and PEC, high Q-factor microdisk are fabricated and characterized. Q-factor as high as ~ 9100 is observed. Demonstration of low threshold lasing is achieved on microdisks with diameters smaller than 2 μm. The implication of the studies reach beyond low threshold lasing and shines light to the optimally matched gain medium for GaN microdisks, namely the InGaN QW.

In pursuit of a method to control cavity resonance, irreversible tuning of the WGMs of p-i-n doped GaN/InGaN microdisks was developed. The method involves photo-excitation of the cavity in DI-water environment, and tuning was achieved over one free spectral range without degrading Q-factors. It is found that fine tuning can be achieved and controlled by applying low incident laser powers. Using this technique, it is possible to deterministically achieve spectral resonances of WGMs with emitters and realize strongly coupled microdisks.

Moreover, high Q-factor GaN photonic crystal nanobeams with InGaN QDs fQWs and QWs are fabricated and introduced in Chapter 3. The fragmented nature of the fQW layer has a surprisingly dramatic influence on the lasing threshold and demonstrate a record low threshold of 9.1 $\mu J/cm^2$, comparable

to the best devices in other III-V material systems. A clear transition from spontaneous emission to lasing is observed with clear linewidth narrowing. The ultra-small modal volume of the cavity and the reduction in the number of competing modes are useful in reducing the threshold. An order of magnitude reduction in lasing threshold is observed on nanobeams fabricated from fQWs, which exhibit nanoscale non-uniformity, compared to those with uniform QWs because of an increased carrier confinement which is expected to reduce the impact of surface states. These observations underscore the advantages of this photonic crystal nanobeam design, matched to the 3-layer fQW gain material. This package is proven to be critically important for fabricating GaN/InGaN nanolasers with excellent performance. Because of their compact size and low thresholds, these devices are excellent candidates for efficient, on-chip optical sources in the blue spectrum.

Last but not least, single photon signature from a GaN/InGaN nanopillar is observed through anti-bunching measurement, demonstrating the quantum nature of the QD emission. Water and gas tuning are attempted on GaN nanobeams with InGaN QDs to achieve spectral resonance between the mode and the emitter. No Purcell effect and no enhancement in spontaneous emission rate was observed, likely due to the spatial mismatch between the cavity modes and the QD positions.

Future research directions for each cavity structure are outlined in their respective chapters. For microdisks, it will be interesting to observe permanent mode-mode coupling of two closely-spaced microdisks through application of the water tuning technique. Moreover, electrical injection for microdisk and nanobeam cavities is an important next step for demonstrating the application potentials of these cavities. Lastly, it is critically important to understand the choice of optimally matched active medium for each cavity structure under electrical injection scheme. The results from these experiments will lead to the ideal material-cavity system for creating blue emitting micro- and nano-lasers in the GaN/InGaN system.

APPENDIX A: **Photoluminescence (PL) Measurement**

The schematic of the PL measurement system is shown in Figure A. For the majority of measurements, unless otherwise indicated, frequency-doubled pulsed Ti:Sapphire laser of 380nm wavelength is used as the excitation source. The excitation laser is sent through a long working distance objective (×40, NA=0.5) to be focused onto the sample. The radius of the laser beam spot is ~ 290 nm. For all materials and fabricated devices presented in this dissertation, the sample absorbs a portion of the excitation laser and subsequently emits photons with principal wavelengths intrinsic to the active material. A portion of the emitted photons is passed through the objective and the optical fiber into the detection systems. The PL spectrum is generated by guiding the photons into a grating-coupled monochrometer with a silicon charge-coupled device (CCD) camera. To carry out time-resolved measurement, the arriving photons are sent into a fast photon counter (MPD Micro Photon Devices). For life-time measurement, the difference between the arrival of the laser pulse and the incident photons generates the life-time

plot of the excited emitter.

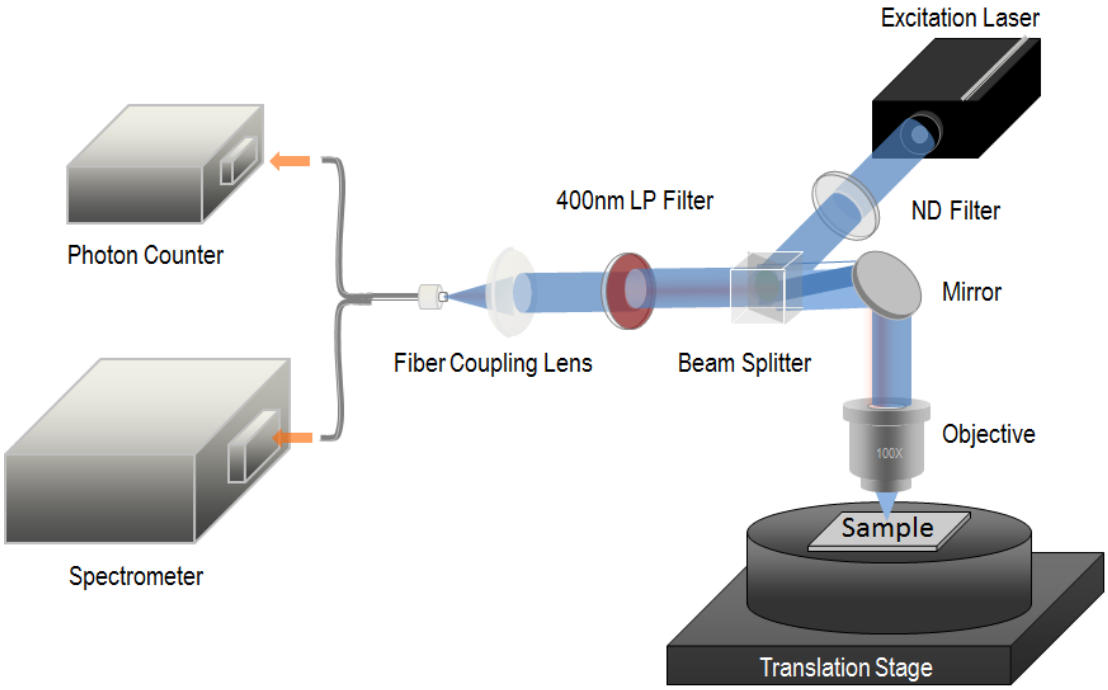

Figure A Schematic of the photoluminescence measurement system.

REFERENCE

1. I. Vurgaftman and J. R. Meyer. *J. Appl. Phys.*, 94:3675, 2003.
2. H. Morkoc. *Handbook of Nitride Semiconductors and Devices*. Wiley-VCH, 2009.
3. D. Holec. *Multi-scale modelling of III-nitrides: from dislocations to the electronic structure*. PhD thesis, University of Cambridge, 2008.
4. T. Zhu. *Nanoscale electrical characterization of gallium nitride*. Ph.D Thesis, University of Cambridge, 2010.
5. W. Götz, N. M. Johnson, J. Walker and D. P. Bour. *Activation of Acceptors in Mg-Doped, p-Type GaN*. MRS Spring Meeting, 1996.
6. M. Suzuki, T. Uenoyama, and A. Yanase. *Physical Review B*, 52(11): 8132–8139, 1995.
7. H. A. R. El-Ella. *III-NITRIDE OPTICAL RESONATORS & INGAN QUANTUM DOTS: MICROSTRUCTURAL & OPTICAL CORRELATIONS*. Ph.D Thesis, University of Cambridge, 2012.
8. M. E. Levinshtein, S. L. Rumyantsev and M. S. Shur. *Properties of Advanced Semiconductor Materials: GaN, AIN, InN, BN, SiC, SiGe*. John Wiley & Sons, 2001.

9. F. Bernardini, V. Fiorentini, and D. Vanderbilt. *Phys. Rev. B*, 56:R10024, 1997.

10. D. Cherns, J. Barnard, and F. A. Ponce. *Solid State Commun*. 111:281, 1999.

11. V. Fiorentini, F.Bernardini, F. D. Sala, A. D. Carlo, and P. Lugli. *Phys. Rev. B*. 60, 8849, 1999.

12. S. F. Chichibu, A. Uedono, T. Onuma, B. A. Haskell, A. Chakraborty, T. Koyama,P. T. Fini, S. Keller, S. P. DenBaars, J. S. Speck, U. K. Mishra, S. Nakamura,S. Yamaguchi, S. Kamiyama, H. Amano, I. Akasaki, J. Han, and T. Sota. *Nat. Mater*. 5:810, 2006.

13. S. Nakamura and S. Chichibu. *Introduction to nitride semiconductor blue lasers and light emitting diodes*. Taylor and Francis, London, 2000.

14. E. J. Thrush. *Presentation: Monitoring MOVPE growth of GaN*. University of Cambridge, 2008.

15. V. I. Klimov, A. A. Mikhailovsky, S. Xu, et al. *Science*. 290(5490): 314-317, 2000.

16. W. K. Leutwyler, S. L. Bürgi, H. Burgl. *Science*, 271(5251): 933-937, 1996.

17. H. Haug, S. W. Koch. *Quantum theory of the optical and electronic properties of semiconductors*. Singapore: World scientific, 2004.

18. U. Merkt, J. Huser, and M. Wagner. *Phys. Rev. B*. 43, 7320, 1991.

19. C. Teichert. *Physics Reports*. 365(5-6):335–432, 2002.

20. K. Yamaguchi, K. Yujobo, and T. Kaizu. *Japanese Journal of Applied Physics*. 39(Part 2, No. 12A):L1245–L1248, 2000.

21. C.M. Reaves, V. Bressler-Hill, S. Varma, W.H. Weinberg, and S.P. DenBaars. *Surface Science*. 326(3):209–217, March 1995.

22. H. A. R. El-Ella, F. Rol, and M. J. Kappers. *Appl. Phys. Lett*. 98, 131909, 2011.

23. R. A. Oliver, G. A. D. Briggs, M. J. Kappers, C. J. Humphreys, S. Yasin, J. H. Rice, J. D. Smith, and R. A. Taylor. *Applied Physics Letters*. 83(4):755, 2003.

24. R. A. Oliver, C. Nörenberg, M. G. Martin, A. Crossley, M. R. Castell, and G. A. D. Briggs. *Appl. Surf. Sci.*, 214:1, 2003.

25. S. Das Bakshi, J. Sumner, M. J. Kappers, and R. A. Oliver. *J. Cryst. Growth*, 311:232, 2009.

26. J. H. Rice, J. W. Robinson, A. Jarjour, R. A. Taylor, R. A. Oliver, G. A. D. Briggs, M. J. Kappers and C. J. Humphreys. *Appl. Phys. Lett*. 84, 4110, 2004.

27. A. F. Jarjour, R. A. Oliver, A. Tahraoui, M. J. Kappers, C. J. Humphreys, and R. A. Taylor. *Phys. Rev. Lett*. 99, 197403, 2007.

28. R. A. Oliver, M. J. Kappers, J. Sumner, R. Datta, C. J. Humphreys. *J. Cryst. Growth*. 289, 506–514, 2006.

29. R. Datta, M. J. Kappers, M. E. Vickers, J. S. Barnard, C. J. Humphreys. *Superlattice Microst*. 36, 393–401, 2004.

30. N. K. van der Laak, R. A. Oliver, M. J. Kappers, C. J. Humphreys. *J. Appl. Phys.* 102, 013513, 2007.

31. K. Bakke, F. Moraes. *Phys. Lett. A.* 376, 2838, 2012.

32. J. H. You, J. Q. Lu, and H. T. Johnson. *J. Appl. Phys.* 99, 033706, 2006.

33. N. G. Weimann, L. F. Eastman, D. Doppalapudi, H. M. Ng, and T. D. Moustakas. *J. Appl. Phys.* 83, 3656, 1998.

34. C. Skierbiszewski, K. Dybko, W. Knap, M. Siekacz, W. Krupczynski, G. Nowak, M. Bockowski, J. Lusakowski, Z. R. Wasilewski, D. Maude, et al. *Appl. Phys. Lett.* 86, 102106, 2005.

35. K. H. Lee, S. J. Chang, P. C. Chang, Y. C. Wang, and C. H. Kuo. *J. Electrochem. Soc.* 155, H716, 2008.

36. N. G. Weimann, L. F. Eastman, D. Doppalapudi, H. M. Ng, and T. D. Moustakas. *Journal of Applied Physics.* 83(7):3656, 1998.

37. T. J. Puchtler, A. Woolf, T. Zhu, D. Gachet, E. L. Hu, and R. A. Oliver. ACS Photonics. 2, 137, 2015.

38. T. Hino, S. Tomiya, T. Miyajima, K. Yanashima, S. Hashimoto, and M. Ikeda. *Applied Physics Letters.* 76(23):3421, 2000.

39. X. J. Ning, F. R. Chien, P. Pirouz, J. W. Yang, and M. Asif Khan. *Journal of Materials Research.* 11(03):580–592, 2011.

40. X. Q. Shen, H. Matsuhata and H. Okumura. *Appl. Phys. Lett.* 86, 021912, 2005.

41. S. Nakamura. *Science*, 281:956, 1998.

42. R. A. Oliver, S. E. Bennett, T. Zhu, D. J. Beesley, M. J. Kappers, D. W. Saxey, A. Cerezo, and C. J. Humphreys. *J. Phys. D: Appl. Phys.* 43:354003, 2010.

43. S. F. Chichibu, H. Marchand, M. S. Minsky, S. Keller, P. T. Fini, J. P. Ibbetson, S. B. Fleischer, J. S. Speck, J. E. Bowers, E. Hu, U. K. Mishra, S. P. DenBaars, T. Deguchi, T. Sota, and S. Nakamura. *Appl. Phys. Lett.* 74:123581, 1999.

44. T. Sugahara, H. Sato, M. Hao, Y. Naoi, S. Kurai, S. Tottori, K. Yamashita, K. Nishino, L. Romano, and S. Sakai. *Jpn. J. Appl. Phys.* 37:L398, 1998.

45. A. Tamboli. *Photoelectrochemical Etching of GaN for High Quality Optical Devices*. Ph.D. Dissertation, University of California at Santa Barbara, 2009.

46. D. Zhuang and J. H. Edgar. *Materials Science and Engineering R-Reports*. 48(1):1–46, 2005.

47. M. S. Minsky, M. White, and E. L. Hu. *Applied Physics Letters*, 68(11):1531–1533, 1996.

48. A. R. Stonas, T. Margalith, S. P. DenBaars, L. A. Coldren and E. L. Hu. *Appl. Phys. Lett.* 78, 1945, 2001.

49. A. J. Woolf. *Low-threshold indium gallium nitride quantum dot microcavity lasers*. Ph.D. Dissertation, Harvard University, 2014.

50. B. Streetman and S. Banerjee. *Solid State Electronic Devices (6th*

Edition). Prentice Hall, 2005.

51. E. D. Haberer, R. Sharma, A. R. Stonas, S. Nakamura, S. P. DenBaars, and E. L. Hu. *Applied Physics Letters*. 85(5):762–764, 2004.
52. E. D. Haberer. *Development and Fabrication of Gallium Nitride-Based Microdisk Lasers Using Photoelectrochemical Etching*. PhD thesis, University of California, Santa Barbara, California, 2005.
53. R. A. Oliver, et al. *Appl. Phys. Lett*. 103(14):141114, 2013.
54. N.K. van der Laak, R.A. Oliver, M.J. Kappers, C.J. Humphreys. *Appl. Phys. Lett*. 90(12):121911, 2007.
55. A. Woolf, T. Puchtler, I. Aharonovich, T. Zhu, N. Niu, D. Wang, R.A. Oliver, and E.L. Hu. *Proceedings of the National Academy of Sciences*. 111, 14042, 2014.
56. R. A. Oliver, A. F. Jarjour, A. Tahraoui, M. J. Kappers, R. A. Taylor, and C. J. Humphreys. *J. Phys.: Conf. Ser*. 61, 889, 2007.
57. K. Srinivasan and O. Painter. *Phys. Rev. A*. 75, 023814, 2007.
58. Y. Xu, R. K. Lee, and A. Yariv. *Phys. Rev. A*. 61, 033808, 2000.
59. M. Pöllinger, D. O'Shea, F. Warken, and A. Rauschenbeutel. *Phys. Rev. Lett*. 103, 053901, 2009
60. K. Vahala. *Optical Microcavities*. World Scientific, 2004.
61. A. Yariv and P. Yeh. *Photonics: Optical Electronics in Modern Communications*. Oxford University Press, 2007.
62. I. Aharonovich, A. Woolf, K.J. Russell, T. Zhu, N. Niu, M.J. Kappers,

R.A. Oliver and E.L. Hu. *Appl. Phys. Lett*. 103, 021112, 2013.

63. A.E. Siegman. *Lasers*. University Science Books, Mill Valley, CA, 1986.
64. P. Salières, A. L'Huillier, P. Antoine, M. Lewenstein. *arXiv* preprint quant-ph/9710060, 1997.
65. P. Salières, A. L'Huillier, and M. Lewenstein. *Phys. Rev. Lett*. 74, 3776, 1995.
66. D. J. Griffiths. *Introduction to Quantum Mechanics*. Pearson Prentice Hall, 2004.
67. M. Asada, Y. Miyamoto, Y. Suematsu. *IEEE J. Quantum Electron*. 22(9):1915–1921, 1986.
68. S. Mosor, J. Hendrickson, B. C. Richards, J. Sweet, G. Khitrova, H. M. Gibbs, T. Yoshie, A. Scherer, O. B. Shchekin, and D. G. Deppe. *Appl. Phys. Lett*. 87, 141105, 2005.
69. A. Faraon, D. Englund, D. Bulla, B. Luther-Davies, B. J. Eggleton, N. Stoltz, P. Petroff, and J. Vuckovic. *Appl. Phys. Lett*. 92, 043123, 2008.
70. D. Sridharan, E. Waks, G. Solomon, and J. T. Fourkas. *Appl. Phys. Lett*. 96, 153303, 2010.
71. K. Hennessy, A. Badolato, A. Tamboli, P. M. Petroff, E. Hu, M. Atature, J. Dreiser, and A. Imamoglu. *Appl. Phys. Lett*. 87, 021108, 2005.
72. J. P. Reithmaier, G. Sek, A. Loffler, C. Hofmann, S. Kuhn, S. Reitzenstein, L. V. Keldysh, V. D. Kulakovskii, T. L. Reinecke, and A. Forchel. *Nature*. 432, 197, 2004.

73. A. Faraon and J. Vuckovic. *Appl. Phys. Lett*. 95, 043102, 2009.

74. I. Aharonovich, N. Niu, F. Rol, K.J. Russell, A. Woolf, H. A. R. El-Ella, M. J. Kappers, R. A. Oliver and E.L. Hu. *Appl. Phys. Lett*. 99, 111111, 2011.

75. N. Niu, T. L. Liu, I. Aharonovich, K. J. Russell, A. Woolf, T. C. Sadler, H. A. R. El-Ella, M. J. Kappers, R. A. Oliver and E. L. Hu. *Appl. Phys. Lett*. 101, 161105, 2012.

76. A. C. Tamboli, A. Hirai, S. Nakamura, S. P. DenBaars, and E. L. Hu. *Appl. Phys. Lett*. 94, 151113, 2009.

77. L. Zhang and E. Hu. *Applied Physics Letters*. 82, 319, 2003.

78. A. Nakagawa, S. Ishii, and T. Baba. *Applied Physics Letters*. 86, 041112, 2005.

79. M. Bayer, T. Gutbrod, J. P. Reithmaier, and A. Forchel. *Phys. Rev. Lett*. 81, 2582, 1998.

80. T. Mukaiyama, K. Takeda, H. Miyazaki, Y. Jimba, and M. K. Gonokami. *Phys. Rev. Lett*. 82, 4623, 1999.

81. S. Deng, W. Cai, and V. N. Astratov. *Opt. Express*. 12, 6468, 2004.

82. S. Ishii and T. Baba. *Appl. Phys. Lett*. 87, 181102, 2005.

83. E. Yablonovitch. *Phys. Rev. Lett*. 58, 2059, 1987.

84. S. John. *Phys. Rev. Lett*. 58, 2486, 1987.

85. J. S. Foresi, P. R. Villeneuve, J. Ferrera, E. R Thoen, G. Steinmeyer, S. Fan, J. D. Joannopoulos, L. C. Kimerling, H. I. Smith and E. P. Ippen. *Nature*. 390, 143, 1997.

86. O. Painter, R. K. Lee, A. Scherer, A. Yariv, J. D. O'Brien, P. D. Dapkus, and I. Kim. *Science*. 284, 1819, 1999.

87. J. Ctyroky. *J. Opt. Soc. Am. A*. 18, 435, 2001.

88. K. J. Vahala. *Nature*. 424, 839, 2003.

89. Y. Gong, B. Ellis, G. Shambat, T. Sarmiento, J. S. Harris, J. Vučković. *Opt. Express*. 18, 8781, 2010.

90. Y. Zhang, M. Khan, Y. Huang, J. H. Ryou, P. B. Deotare, R. Dupuis, M. Lončar. *Appl. Phys. Lett*. 97, 051104, 2010.

91. J. L. O'Brien, A. Furusawa, and J. Vuckovic. *Nat. Photonics*. 3, 687, 2009.

92. J. Leuthold, C. Koos, and W. Freude. *Nat. Photonics*. 4, 535, 2010.

93. M. Eichenfield, J. Chan, R. Camacho, K. J. Vahala, and O. Painter. *Nature*. 462, 78, 2009.

94. D. G. Grier. *Nature*. 424, 21, 2003.

95. D. Psaltis, S. R. Quake, and C. Yang. *Nature*. 442, 381, 2006.

96. Q. Quan and M. Loncar. *Optics Express*. 19, 18529, 2011.

97. Q. Quan, P. B. Deotare, and M. Loncar. *Appl. Phys. Lett*. 96, 203102, 2010.

98. J. Danhof, U.T. Schwarz, A. Kaneta, Y. Kawakami. *Phys. Rev. B*. 84, 035324, 2011.

99. J. Danhof, H. M. Solowan, U. T. Schwarz, A. Kaneta, Y. Kawakami, D. Schiavon, T. Meyer, M. Peter. *Phys. Status Solidi B*. 249, 480–484, 2012.

100. T. Baba. *IEEE J. Sel. Top. Quant.* 3, 808-830, 1997.

101. M. Boroditsky, R. Vrijen, T. F. Krauss, R. Coccioli, R. Bhat, and E. Yablonovitch. *Journal of Lightwave Technology*. 17, 2096, 1999.

102. E. M. Purcell. *Phys. Rev. Lett.* 69, 681, 1946.

103. A.W. Snyder and J.D. Love. *Optical Waveguide Theory*. Chapman and Hall, New York, 1983.

104. W.C. Chew and W.H. Weedon. *Microwave Opt. Technol. Lett.* 7, 599-604, 1994.

105. J. P. Hugonin and P. Lalanne. *J. Opt. Soc. Am. A.* 22, 1844-1849, 2005.

106. E. Silberstein, P. Lalanne, J.-P. Hugonin and Q. Cao. *J. Opt. Soc. Am. A.* 18, 2865-2875, 2001.

107. A. Armaroli, A. Morand, P. Benech, G. Bellanca and S. Trillo. *J. Opt. Soc. Am. A.* 25, 667-675, 2008.

108. J. T. Choy, B. J. M. Hausmann, T. M. Babinec, I. Bulu, M. Khan, P. Maletinsky, A. Yacoby and M. Loncar. *Nature Photonics*. 5, 738-743, 2011.

109. E.D. Palik. *Handbook of optical constants of solids*. Academic Press, New York, 1985.

110. K. Hennessy, A. Badolato, M. Winger, D. Gerace, M. Atatüre, S. Gulde, S. Fält, E. L. Hu & A. Imamoğlu. *Nature*. 445, 896-899, 2007.

111. J. P. Reithmaier, G. Sęk, A. Löffler, C. Hofmann, S. Kuhn, S. Reitzenstein, L. V. Keldysh, V. D. Kulakovskii, T. L. Reinecke & A.

Forchel. *Nature*. 432, 197-200, 2004.

112. H. J. Kimble. *Physica Scripta*. T76, 127–137, 1998.

113. K. J. Vahala. *Nature*. 424, 839-846, 2003

114. O. Demichel, M. Heiss, J. Bleuse, H. Mariette, and A. F. i Morral. *Appl. Phys. Lett*. 97, 201907, 2010.

115. Y. Dan, K. Seo, K. Takei, J. H. Meza, A. Javey, and K. B. Crozier. *Nano Letters*. 11, 2527, 2011.

116. H. Morkoç. *Handbook of Nitride Semiconductors and Devices, Electronic and Optical Processes in Nitrides*. John Wiley & Sons, 2009.

117. J. W. Robinson, J. H. Rice, A. Jarjour, J. D. Smith, R. A. Taylor, R. A. Oliver, G. A. D. Briggs, M. J. Kappers, C. J. Humphreys and Y. Arakawa. *Appl. Phys. Lett*. 83, 2674, 2003.

118. R. A. Taylor, J. W. Robinson, J. H. Rice, A. Jarjour, J. D. Smith, R. A. Oliver, G. A. D. Briggs, M. J. Kappers, C. J. Humphreys, Y. Arakawa. *Physica E: Low-dimensional Systems and Nanostructures*. 21(2), 285-289, 2004.

119. J. H. Rice, J. W. Robinson, J. H. Na, K. H. Lee, R. A. Taylor, D. P. Williams, E. P. O'Reilly, A. D. Andreev, Y. Arakawa and S. Yasin. *Nanotechnology*. 16(9), 1477, 2005.

120. M. Abbarchi, F. Troiani, C. Mastrandrea, G. Goldoni, T. Kuroda, T. Mano, K. Sakoda, N. Koguchi, S. Sanguinetti, A. Vinattieri, and M. Gurioli. *Applied Physics Letters*. 93, 162101, 2008.

121. T. Yoshie, A. Scherer, J. Hendrickson, G. Khitrova, H. M. Gibbs, G. Rupper, C. Ell, O. B. Shchekin & D. G. Deppe. *Nature*. 432, 200-203, 2004.